UNIVERSITY OF OKLAHOMA

GRADUATE COLLEGE

METHODS OF VELOCITY DETERMINATION AND NOISE REDUCTION IN THE PROCESSING OF NEAR-SURFACE SEISMIC REFLECTION DATA

A Dissertation

SUBMITTED TO THE GRADUATE FACULTY

in partial fulfillment of the requirements for the

degree of

Doctor of Philosophy

By

ZHI-MING LIU
Norman, Oklahoma
1999

UMI Number: 9957002

UMI

UMI Microform 9957002

Bell & Howell Information and Learning Company
300 North Zeeb Road
P.O. Box 1346
Ann Arbor, MI 48106-1346

METHODS OF VELOCITY DETERMINATION AND NOISE REDUCTION IN THE PROCESSING OF NEAR-SURFACE SEISMIC REFLECTION DATA

A Dissertation APPROVED FOR THE SCHOOL OF GEOLOGY AND GEOPHYSICS

BY

ACKNOWLEDGMENTS

I would like to thank my advisor, Dr. Roger Young, for his advice and supervision for the dissertation. Without his guidance and help in all aspects, this dissertation would be impossible to be complete.

I would like to thank Dr. William Doll of Oak Ridge National Laboratory for his guidance in the processing of the near-surface vibroseis reflection data set of the K-25 Site, TN.

I would like to thank Dr. Stephen Danbom of Conoco, Inc., for his major contribution in the field data acquisition and his guidance in the data processing of the near-surface seismic reflection data set of the Gypsy Outcrop Site, OK. His suggestions have made this dissertation improved.

I would like to thank Mr. Pat Lindsey of GX Technology for providing his ideas and illustrations for the continuous spectral balancing algorithm. Mr. Lindsey has also given me fresh ideas in other noise suppressing algorithms. Mr. Lindsey's comments have made this dissertation better.

I would like to thank Dr. Peter Lemiszki of Tennessee Division of Geology for his assistance in the geological interpretation of K-25 stacked sections.

I would like to thank the professors in my Ph.D. committee, Dr. James Forgotson, Dr. Judson Ahern, Dr. John Pigott and Dr. Samuel Osissanya for their time, care, and suggestions for my Ph.D. degree progress and for the writing of this dissertation.

I would like to thank Dr. Paul Valasek of Phillips Petroleum Company for mentoring my prestack depth migration and presentation skills.

Thanks to Dr. Brad Car of Oak Ridge National Laboratory for clearing issues in the preliminary processing of K-25 data set. Thanks to Kansas Geology Survey, especially Rick Miller, for the assistance to the Oak Ridge National Laboratory in the acquisition of the K-25 data set. Thanks to Dr. John Costain of Virginia Polytech Institute, Dr. Kevin Smart of University of Oklahoma, Phil Hall of Star Geophysics and Julian Ivanov of Kansas Geological Survey, for their help and correspondence in various aspects.

Thanks to Zhenghan Deng (previously University of Oklahoma), Richard Weindell (previously University of Tulsa) and Dr. Christopher Liner of University of Tulsa, for their participation in the seismic data acquisition at the Gypsy Outcrop Site.

I would like to thank the School of Geology and Geophysics, Dr. Charles Gilbert and other faculty members, for providing a wonderful environment for learning and experimenting. Thanks to Donna Mullins for reminding me about Ph.D. degree requirements. Thanks to my wife, Xian Tan, for her assistance in completing this dissertation. Thanks to the Unix Administrators of the Shell Crustal Imaging Facility

(SCIF.) of the University of Oklahoma, Geoff Quelch, Stephen Sandifer, and Kathy Rosborough, for their Unix Systems Support.

The financial support of dissertation has been provided by the Oak Ridge National Laboratory (ORNL) and the Oklahoma Center for the Advancement of Science and Technology (OCAST). These government entities will have a non-exclusive permission to use or allow others to use the published form of this dissertation for government purposes.

The seismic data processing is performed using ProMAX of Landmark Graphics Corp., and FOCUS of CogniSeis Corp. The seismic ray-tracing modeling is performed using GXII of GX Technology.

TABLE OF CONTENTS

ABSTRACT

The present work extends methods of noise reduction and velocity analysis used in conventional seismic reflection exploration (target depths of greater than 1000 ft) to near-surface seismic cases (target depths less than, or much less than, 1000 ft). Two study sites are treated, and the particular difficulties encountered require the use of unconventional approaches.

In addition to the investigations of noise reduction and velocity analysis using data processing techniques existing, I have programmed the "Continuous Spectral Balancing" algorithm, based on the ideas of Pat Lindsey. I have designed and developed a new algorithm – "Local Slant-Sum Adaptive Noise Removal". Examples on synthetic and real data shot gathers show that both algorithms are effective.

At the K-25 Site, Oak Ridge, TN, the zone of interest is from the very near-surface to 1800 ft depth. 2-D Vibroseis seismic reflection surveys were used in non-invasive radioactive waste remediation. Deeper targets due to larger layer impedance contrasts produce stronger reflections following hyperbolic traveltimes. The signal/noise ratio is much higher, and it is not a problem to obtain stacking velocities and hence interpretable stacked reflections. Special data processing techniques such as Vibroseis whitening, refraction statics, continuous spectral balancing have improved the stacked sections. Geological interpretations are made based on stacked sections and surface geological observations. Iterative prestack depth-migration velocity analysis and prestack depth

migration have resulted in more accurate depths to horizons and faults, which may influence waste migration in the K-25 vicinity and off-site. 3-D seismic exploration is recommended for future seismic reflection studies.

At the Gypsy Outcrop Site, OK, the depth of interest is less than 100 ft. 2-D seismic surveys used a shotgun as source. The signal/noise ratio is very poor. CMP stacking fails to produce interpretable reflections. Because of the implausible velocities from the outcrop velocity measurements, it is decided that the seismic modeling results are not reliable. A composite walk-away display convincingly illustrates that only one possible reflection event exists in the expanding spread profile survey. This event is estimated to be at the bottom of the shallow Gypsy sandstone unit. Survey parameters are recommended to improve the success of seismic reflection surveys faced with similar difficult circumstances.

INTRODUCTION

This dissertation is an investigation of methods of velocity determination and noise reduction in the processing of the near-surface seismic reflection data from two seismic reflection study sites. Although the basic data acquisition and processing procedures using seismic reflections have, over time, been formulated into the common-midpoint (CMP) method by petroleum exploration companies, the use of this method in shallow exploration has been exploited greatly in the past decade (Burger, 1992; Steeples et al., 1995, 1997; Doll and Coruh, 1995; Doll et al., 1994; Doll et al., 1996; Doll et al., 1998; Miller and Xia, 1997). The present work seeks to extend the near-surface seismic data processing to two seismic study sites, to adopt unconventional approaches required by the particular difficulties encountered, and to offer recommendations for improving the success of the reflection method for shallow targets. In addition, two special noise filtering algorithms that I have developed will be presented in Appendix A (Continuous Spectral Balancing) and Appendix B (Local Slant-Sum Adaptive Noise Removal). These special filtering algorithms are important to filtering out ground-roll and other linear-coherent noise, especially for near-surface ground-roll and coherent noise problems.

The two seismic reflection study sites are the K-25 Site, Oak Ridge, Tennessee, and the Gypsy Outcrop Site, Oklahoma. The method of determining velocities necessary for seismic imaging varies greatly for these two sites. For the K-25 Site, obtaining stacking velocities is not a problem because of relatively high S/N ratio in the far offsets of the shot gathers. In addition, relatively deep targets from layer impedance contrasts produce strong reflections following hyperbolic traveltimes. However, in order to know the depth and thus to obtain better geological interpretation, iterative prestack migration velocity analysis is utilized. For the Gypsy Outcrop Site, the S/N ratio is so low that there is no way of obtaining stacking velocities for a CMP stack. Alternative velocities are needed in order to know where to find the possible reflections.

At the K-25 Site, noise is not very serious, but it is necessary to use special filtering to improve the S/N of the data, making it suitable for CMP stacking and for depth migration. At the Gypsy Outcrop Site, noise is very serious. Conventional filtering to attenuate noise and seismic ray-trace modeling to predict events are attempted and great difficulties are encountered. Noise is a serious problem inside the air-wave and ground-roll cone for both sites. This is also true for most near-surface data sets. I have attempted to attack this problem.

Chapter 1 discusses the seismic data processing and analysis, including velocity determination and noise reduction method for the near-surface seismic reflection data from the K-25 Site, Oak Ridge, Tennessee. This site consists, for the most part, of lower Paleozoic dolomites, sandstones and shales and has been subjected to periods of thrusting associated with the history of the Applachian Mountains (Peter Lemiszki, 1994). The seismic survey and data processing are part of the waste monitoring and remediation effort on the Oak Ridge Reservation (Doll et al., 1998).

The seismic reflection data were acquired by Oak Ridge National Laboratory in 1995–1996, with the assistance of the Kansas Geology Survey, using a 96 channel GeoMetrics seismograph and an IVI Minivib as the seismic source. The purpose of the survey was to define the locations of faults and horizons that would affect the choice of monitoring wells to be drilled for waste remediation. This acquisition effort was much closer in practice to conventional petroleum exploration surveys in that targets were deeper, maximum offsets were longer, the number of recording channels was greater, and the seismic source was more energetic, than in the Gypsy survey. The correlated Vibroseis reflection data shows higher S/N ratio and more continuous reflection events than at the Gypsy Outcrop Site. There are recognizable reflections in the far offsets. In both cases, however, ground-roll obscures reflections at near offsets.

A special noise filtering step, the Continuous Spectral Balancing, increased the S/N ratio, particularly on the larger-offset traces. Stacking velocities are successfully obtained from the data. Stacked sections show reflection events that correspond to fault boundaries, which separate rocks with large impedance differences. This seismic observation is consistent with laboratory velocity measurements. Conventional processing succeeds very well at the K-25 Site. The geologic column shows thin shales interbedded with dolomites. This character is observed from the seismic reflection data. Geological interpretations are completed based on the seismic stacked sections and surface geology of the K-25 Site. However, there is a need to know the depth of the geological layer boundaries. The stacking velocities obtained from semblance velocity analysis are not accurate for conversion to interval velocity and thickness because dipping structures, folding and faulting deviate the seismic raypaths from vertical. Furthermore, the spatial locations of steeply dipping geological boundaries must be repositioned by migration. In order to obtain more accurate structural images, prestack depth migration was performed. The result of having a depth section is that a better geological interpretation can be made. Various sources of velocity information for the construction of the interval velocity–depth model necessary for depth migration were considered, such as stacking velocities, velocities from rock samples, and iterative migration velocity analysis using Kirchhoff prestack depth migration. Stacking velocities were not accurate because dipping structures, folding and faulting deviate seismic raypaths from vertical, and thus stacking velocities were not used for depth migration. The velocities from relevant rock samples in Virginia were useful geological constraints, roughly limiting the interval velocities within reasonable range for the rock types in the seismic survey areas at K-25 Site. The iterative migration velocity analysis from Kirchhoff prestack depth migration gave the best structural image and this was made possible by the higher S/N ratio of reflections and thicker layering at the Oak Ridge K-25 Site. A depth section was obtained using the velocity–depth model from the iterative migration velocity analysis. The depth section led to modification of the geological interpretation based on the geologic mapping and the stacked seismic sections.

Chapter 2 discusses the seismic data processing and analysis, including velocity determination and noise reduction methods for the near-surface seismic reflection data from the Gypsy Outcrop Site, Oklahoma. This site is the location for extensive geological and geophysical studies characterizing the lithology, continuity, and sedimentary features of stacked channel sands in a fluvial-deltaic environment of Pennsylvanian (Doyle et al., 1992) age. This project was supported by the Oklahoma Center for the Advancement of Science and Technology (OCAST). The present study is one part of that project and is a feasibility study of reflection imaging in the interborehole volume.

The geological target at the Gypsy Outcrop Site is very shallow, 0–100 ft in depth. A refraction survey was carried out earlier at the Gypsy Outcrop Site to map the structure (velocity and depth) of the very shallow subsurface. The result of that survey showed that the bottom of the uppermost channel sand was a refractor at a variable depth of 5–15 ft and that the refractor velocity varied laterally. A CMP reflection survey was shot to image deeper channel boundaries between mudstones and sandstones. Due to the difficulties of recognizing reflection events and the difficulties in noise filtering of the CMP Line, an "Expanding Spread Profile" (ESP survey) was collected using high fold and wide offset range in hope of improving the S/N ratio in the vicinity of borehole control.

Chapter 2 will present the difficulties in using band-pass and F-K filtering to reduce noise. Chapter 2 will next present the difficulties in obtaining a reliable velocity–depth model in an attempt to use seismic raytrace modeling to predict possible reflections in the ESP Line. A composite walk-away display illustrates that only one reliable reflection event exists in the ESP survey. This reflection is approximately at the boundary between the Gypsy sandstone and the Tallant marine sandstone, indicating that the Gypsy sandstone sequence is seismically indistinct. Finally, this chapter will offer recommendations for modifying the survey approach to help overcome the S/N problem at similar sites.

Appendix A discusses a new noise filtering algorithm, "Continuous Spectral Balancing". I have programmed this algorithm locally on a Unix workstation in the Shell Crustal Imaging Facility of the university of Oklahoma, based on the ideas of Pat Lindsey of GX Technology. This algorithm uses the spectral differences to separate noise from signal. This algorithm is important and useful in that it removes narrow-banded noise such as ground-roll and reverberative noise. Synthetic seismic traces are used to verify the algorithm. Real data examples for data sets from both the K-25 Site and the Gypsy Outcrop Site are included to show the effectiveness of the algorithm.

Appendix B presents another new noise filtering algorithm. It is called Local Slant-Sum Adaptive Noise Removal. This is a workstation-based, interactive, and multi-channel process. By evaluating noise wavelets within small, local and slant-time windows in the time-space domain, this method is designed to filter noise from signal even with small spectral differences, to avoid spatial aliasing, and to filter dispersive ground-roll. Both synthetic and real-data examples for the K-25 shot gathers show that the algorithm will be useful and robust to remove ground-roll noise which exist locally in some of the shot gathers. The algorithm will improve the seismic imaging of the very near-surface of seismic reflection study sites such as the K-25 Site by removing the ground-roll noise locally in the shot gathers.

CHAPTER 1 DATA PROCESSING OF NEAR-SURFACE SEISMIC REFLECTION DATA FROM THE OAK RIDGE K-25 SITE, TENNESSEE

1.1 INTRODUCTION

The K-25 Plant, Oak Ridge, Tennessee, formerly known as the Oak Ridge Gaseous Diffusion Plant, was constructed in the 1940s and was used for enrichment of uranium hexafluoride until 1985. The enrichment procedures and related activities generated non-hazardous, hazardous, radioactive, and mixed wastes that have been stored, treated, or disposed in the vicinity of the K-25 Plant (referred to as the Oak Ridge K-25 Site). Effective monitoring and remediation requires an accurate geologic and hence hydrologic model. Seismic investigation is needed to define the locations of faults and horizons that would affect the determination of the locations of the monitoring wells to be drilled for waste remediation.

Seismic reflection data were acquired by the Kansas Geological Survey to provide three-dimensional control of faults and formation contacts previously mapped at the surface (Lemiszki, 1994) for incorporation into a drilling and ground water monitoring strategy intended to detect any contaminant migration off-site. Between August and December, 1995, approximately 5,000 shot points of seismic reflection data of 13 seismic lines were acquired in the vicinity of the K-25 Plant (Doll et al., 1996). Preliminary data processing was started and brute stacks were obtained for all of the seismic lines in 1996 by Doll and Kaufman (Doll, 1996, personal communication). Initial geological interpretation was made based on the brute stacks. However, a structural interpretation from the brute stack is not reliable because the structural images would not be correct, due to problems such as low signal-to-noise ratio, the statics shifts of structures, poor event alignment caused by statics and incorrect NMO velocities, etc. Depth values of geological structures are important because we are interested in waste remediation up to 900 ft in depth. A time section does not show depth to targets.

Workstation processing started in June 1996, as my summer internship assignment with Doll at Oak Ridge National Laboratory. The major objective of the processing was to obtain improved stacked sections for the interpretation of faults and horizon contacts, which are controls of possible waste migration paths. Five seismic lines were processed using common-midpoint stack, with the addition of Vibroseis whitening and refraction statics. Much of my processing effort at the University of Oklahoma was on the reprocessing of one of the five lines, with large amount of work on different processing procedures to produce a good image for the line. The objective of the complete seismic data processing was to obtain more reliable and detailed interpretation of the fault locations and major stratigraphic units. The result of the complete processing of Line I through prestack depth migration is a new interpretation of the faults and the horizons on the K-25 line. The prestack depth migration provides more reliable depths of geological structures.

1.2 GEOLOGICAL SETTING

The K-25 Site, Oak Ridge, Tennessee, is located in the Valley and Ridge Province of the Southern Appalachians, in an area of folded and faulted Cambrian through Ordovician sedimentary rocks in the footwall of the White Oak Mountain Fault. Figure 1 shows the regional structural setting of the Oak Ridge Reservation within the Valley and Ridge Province. Figure 2 shows the geologic map of the Oak Ridge Reservation. The K-25 Plant buildings are located to the right of BB'. Dips measured at the surface in the vicinity of the plant range from near-horizontal to near-vertical. The area is characterized by multiple stages of thrust faulting, affecting the lower Paleozoic rocks. The primary faults include the K-25 Fault and the White Oak Mountain Fault. There are also secondary faults (KF-1, KF-2, KF3). The fault boundaries are obtained through surface geological mapping. Figure 3 shows the stratigraphic units and their thicknesses within the Oak Ridge Reservation. The Rome Formation is of Cambrian age and consists mainly of sandstones/shales, having a thickness of at least 400 m (1312 ft). The Knox Group is partly of Cambrian age and partly of Ordovician age. The Knox Group consists mainly of dolomites, having a total thickness of 837 m (2746 ft). The Chickamauga Supergroup is of Ordovician age. It consists mainly of limestones, having a total thickness of 647 m (2122 ft). Because the Rome Formation, the Knox Group, and the Chickamauga Supergroup include shales as interbedded layers, large acoustic impedance contrasts exist. Consequently, one expects large amplitude reflections from layer boundaries between shales and dolomites, and shales and limestones. The thrust faulting brings different lithologic units in contact, providing acoustic impedance contrasts across faults also.

Large reflection amplitudes from boundaries between the major groups themselves (e.g., Rome Formation/Chickamauga Supergroup) are also expected. Figure 4 shows two cross-sections BB' and CC'. However, these cross-sections were based on surface geological mapping and there were not a lot of outcrop locations to provide surface geological data. The interpretation of the geological boundaries at depth is highly hypothetical, having been extrapolated from the surface downward without any depth control. The reflection images from seismic data will verify and enable better understanding for the faults and horizon contacts in depth so that a more reliable understanding of the K-25 geology will be obtained to assist in the waste monitoring and remediation.

1.3 SEISMIC DATA ACQUISITION

A total of thirteen CDP seismic reflection lines were acquired by the Kansas Geological Survey in and around areas with geologic features potentially significant to the transport and fate of surface and subsurface contaminants.

The seismic reflection data were obtained with an IVI Minivib vibrator source, with a 10 second linear up-sweep from 30 to 300 Hz tapered on both ends for 0.25 seconds, (Doll et al., 1996). The data were recorded on two 48-channel, 24-bit Geometrics StrataView seismographs interfaced for simultaneous 96-channel recording.

Three Mark Products L28E 40 Hz geophones were wired in series and deployed in a 1 m (3.48 ft) array at each station. The receiver and shot station spacing was 3.048 m (10 ft).

The geophone conditions ranged from gravel roadbed to manicured grass lawn. The use of 14 cm spikes and removal of the loose surface material was critical to the amplitude and frequency response of the geophones.

Three shots were separately recorded, along with the source sweep (pilot trace), in uncorrelated form for each shot station. This special recording, rather than the conventional recording of the correlated traces directly in the field, has the advantage that customized correlation procedures, such as Vibroseis whitening plus correlation, can be carried out later during processing stage in order to produce optimally correlated seismic traces (Doll et al., 1996).

Figure 5 shows the locations of the five seismic lines (Line I, E1, E2, F1, F2) that were processed in the summer of 1996 at the Oak Ridge National Laboratory. The seismic lines were designed to be near the faults and to be roughly along dip directions of the faults in order to provide information about dips of the faults. The reprocessing at the University of Oklahoma was emphasized on Line I, with complete reinvestigation of processing procedures and parameters. Because Line I is near the cross-section CC' (Figure 4), it is interesting to see how much additional information the seismic data will reveal.

The shooting of Line I started from the north end (smaller station numbers) and moved steadily toward the south end. The shots started from push-end at shot no. 1001 (north end of the line) until shot no. 1179. Then they changed to walk-through until shot no. 1219. Then they changed to drag-on until shot no. 1371 (the south end of the line).

Because there was more noise interference from near offsets than from far offsets, there was higher S/N ratio for large-offset shot gathers when the shot-receiver was in a push-end or pull-off pattern, whereas lower S/N ratio for small-offset shot gathers when the shot point walked through the receiver spread. . However, that was the trade-off of the seismic survey due to the restricted access and topographic limitation.

1.4 PROCESSING FLOW

Figure 6 is the processing flow chart for Line I. The first box, labeled preprocessing, includes processing steps performed at the Oak Ridge National Laboratory using FOCUS (Seismic processing software of CogniSeis). The second box, labeled "Filtering, Trace Killing, Muting", and the third box, labeled "Time Correction and Stacking", featured the processing steps performed at the University of Oklahoma using ProMAX (Seismic processing software of Landmark). In the second box, there is also a special algorithm, "continuous spectral balancing" (Appendix A), which was locally written by myself. It was applied to filter ground-roll and other narrow-band noise. F-K filtering was tested on the shot gathers of Line I, however, there was too much smearing and smoothing. So the F-K filtering will not be included in the processing flow. Residual statics was also tested by picking horizons on stacked sections of Line I and then estimating and applying residual statics corrections (maximum 4 ms) on shot gathers. The residual statics did not show much improvement on the stacked sections of Line I. Therefore residual statics will not be included in the processing flow either.

1. PREPROCESSING

Uncorrelated shot-gather field files were down-loaded into IBM PC computers. The files were then transferred into a SUN workstation at the Oak Ridge National Laboratory for correlation and subsequent processing.

Vibroseis Whitening (VSW)

VSW is an unconventional correlation procedure for Vibroseis data (Doll and Coruh, 1995; Coruh and Costain, 1983). VSW is a robust means of whitening the spectra of high-resolution shallow seismic data. It applies an automatic gain control (AGC) to the swept source data in the local time domain before they are correlated with the source sweep. In the wave propagation process through the earth, higher frequency components (later time during the linear up-sweep) of data have higher tendency to be attenuated, due to the nature of the impulse response of the earth. An AGC compensates the weaker signals in later time (higher frequency components in a linear up-sweep) in an uncorrelated trace. This makes the trace data correlate better with the source sweep, because the source sweep does not have any decay of amplitude versus frequency (time). The field recording of uncorrelated swept trace data makes VSW possible, along with the advantage of allowing choice of correlating sweep length and the type of pilot trace (Doll and Coruh, 1995), resulting in the best correlated traces and hence improved stacked sections. A longer AGC length will preserve relative amplitudes in the uncorrelated trace data, while a shorter AGC length will boost high frequency components which were attenuated during the propagation through the earth. An AGC length of 250 ms produced optimally correlated shot gathers for the K-25 data sets, taking into account both the relative amplitudes and the compensation of the high frequency components for reflections.

Correlation

This step consists of the cross-correlation of the pilot trace with the uncorrelated trace data. The pilot trace is the 10 s linear up-sweep from 30 Hz to 300 Hz transmitted by the MiniVib truck, recorded in channel 1 of 96 channels in each shot. The uncorrelated trace data is the 12 second record received by geophones, in channels 2-96. The cross-correlation of the source sweep with the recorded uncorrelated trace data produces a correlated shot gather of 95 traces, 2 seconds in length.

Vertical Stacking

Since there were three shots at each shot location, with exactly the same source and receiver locations, they were cross-correlated with the corresponding pilot traces and then the correlated traces were vertically stacked, i.e., by simple trace-by-trace summation, to produce one shot gather as output. Random noise was reduced by vertical stacking.

Refraction Statics

Refraction statics corrects the time shift caused by irregular distribution of weathering layer velocity and thickness. The refraction statics was computed tomographically (Taner et al., 1994) using FOCUS (CogniSeis software). Four steps were used: (1) pick first arrival times from shot gathers; (2) assign refractors; (3) solve for refraction statics; (4) apply refraction statics correction to data, correcting traveltimes to a datum of 800 ft. Even though doing refraction statics is time consuming due to the amount of work in steps (1) and (2), it is rewarding in defining correct structural images, as compared with doing no statics or only elevation statics.

Figure 7 shows the refraction statics curves for the five seismic lines (I, E1, E2, F1, F2). The top of each panel shows the surface elevation and the refractor elevation. The middle of each panel shows the refractor velocity. The refractor velocities are in the range of 10,000--20,000 ft/s, which are indications of the near-surface lithological/structural changes. The bottom of each panel shows the long wavelength and short wavelength refraction statics. The refraction statics values vary in the range of approximately 20ms. The short wavelength statics will affect how well the traces are aligned for stacking, thus it will affect the amplitude of the stacked traces. The long wavelength statics will cause undulation of reflection images. Therefore, the refraction statics correction is necessary for the K-25 seismic lines to ensure correct structural images.

2. FILTERING, TRACE KILLING, MUTING

Notch Filtering and Band-pass Filtering

A notch filter removes cultural noise (60 Hz), such as from power lines and motors; whereas a band-pass filter removes both low and high frequency noise. Because the notch filtering is an additional feature in the band-pass filtering module in ProMAX, the notch filtering and the band-pass filtering are applied together to the shot gathers of Line I.

Figure 8 shows the effect of both the notch and the band-pass filtering. The best notch filter has a central frequency of 60±4 Hz, and the notch is automatically searched and located at the peak frequency within the range. The notch filter has a width of 6 Hz. As shown in Figure 8, both the 60 Hz noise and the 62 Hz have been removed. A trapezoidal band-pass filter (20, 40, 100, 150) Hz was also applied. The band-pass filter removed high frequency noise and improved the general appearance of the shot gathers. However, there was not much improvement of reflections inside the air-wave and ground-roll cone. In addition, tests showed that increasing frequency values at the high-end of the band-pass filter allowed high-frequency noise to pass; and that increasing frequency values at the low-end damaged the low frequencies in the reflections, without much reduction in the noise modes such as air-wave and ground-roll. Without the band-pass filtering, the 60 Hz noise traces would have appeared as 180 Hz residual noise traces.

Continuous Spectral Balancing

The continuous spectral balancing (Appendix A) was used as a special filtering option to filter out reverberative, i.e., mono-frequency noise. A continuous spectral balancing filter having the following parameters was applied to the shot gathers of Line I.

Number of Subchannels	=	10
Low Cut Frequency	=	20 Hz
High Cut Frequency	=	150 Hz

Figure 9A shows a shot gather with reverberative noise. After continuous spectral balancing, the noise was substantially reduced and the possible reflections stand out much better (Figure 9B). It must be pointed out that not all of the shot gathers of Line I have reverberative noise.

Predictive Deconvolution Test

A prediction operator seeks a time-advanced form of the input time series. The coefficients of the operator are solved from a matrix equation involving the auto-correlation of the seismogram to be filtered. A prediction error filter is constructed by one minus the prediction operator. Convolving the prediction error filter with the seismogram removes the predictable part of the seismogram (the wavelet) from the unpredictable part of the seismogram (the impulse response) of the earth (Yilmaz, 1991). This procedure is called predictive deconvolution.

Figure 10A shows an event that parallels with the first arrivals (event G inside the yellow box). It is interpreted to be reverberated refraction, the raypath of which is shown at the bottom of Figure 10A. The additional traveltime required for the reverberation in the layer above the refractor is estimated to be approximately 50 ms for a layer thickness of 100 ft and a velocity of 4500 ft/s (Line I, Figure 7). This agrees with the traveltime of event G being approximately 50 ms greater than the first-arrival.

A predictive deconvolution filter with a prediction lag of 12 ms and an operator length of 80 ms was tested as a means of reducing the reverberated refractions (event G inside yellow box in Figure 10A). It was expected that after removing the reverberated refractions, shallow reflections would become more visible. Even though it was understood that the predictive deconvolution filtering should only be good to filter out the reverberated refraction noise, it was applied to the entire shot gather in order to see what would happen to the entire shot record.

After applying the predictive deconvolution to the shot gather in Figure 10A, the reverberated refractions (event G inside the yellow box of Figure 10A) have been substantially reduced (Figure 10B). However, the predictive deconvolution has damaged the reflections also. Event R is likely a reflection, rather than a reverberated refraction. However, it has been greatly attenuated inside the first yellow box. There is a 25-50 ms time delay in the far offsets for event A (Figure 10A), which becomes event A' (Figure 10B). But event A is a strong reflection, not a reverberated refraction noise. In addition, event A (Figure 10A) becomes very discontinuous (A' in Figure 10B). The strong reflection event B (Figure 10A) becomes very discontinuous (B' in Figure 10B), almost not recognizable as a reflection event.

From the damages to the reflections, it can be seen that the predictive deconvolution should not be applied to the final processing flow.

Summary of Filtering in Shot Gathers

Figure 11 shows a comparison of shot gathers before and after the above filtering. Figure 11A includes six VSW correlated shot gathers. Figure 11B includes the corresponding shot gathers after notch and band-pass filtering, and continuous spectral balancing. The reverberative noise in S1351 and S1081 (Figure 11A) has been reduced, shown in Figure 11B. The 60 Hz noise in S1271 (Figure 11A) has been substantially reduced, shown in Figure 11B. The other three shots also show different levels of noise reductions and signal enhancements. Possible reflections are marked on Figure 11B. These reflections provide a verification of the reflection events in the stacked sections. For example, the events marked with the green lines correspond to the two strong reflection events (passing 140 ms and 190 ms at CDP 810) in Figure 16D.

Trace Killing

Trace killing was deferred until this stage because some noisy traces, such as those with 60 Hz noise or reverberative noise, might have been improved substantially through the various filtering above.

First, trace 1 of each shot was killed because it was the auto-correlation of the pilot trace, not representing any reflection events. Second, very noisy traces were killed interactively. Third, the very near offset (0-30 ft) traces were killed because these traces showed in strong interference due to direct arrival, air-wave, and ground-roll.

Mute of First Arrival, Air Wave and Ground Roll

Figure 12 shows an example of typical mutes in shot gathers, including moderate top mute, severe top mute, surgical mute of air-wave, and bottom mute of air-wave and ground-roll. Those different mute options will be tested later in the processing tests.

The moderate top mute removes only the events from zero time through the first wavelet packet of the first arrival, preserving any possible reflections that are close to the first arrival. The severe top mute removes first arrivals and subparallel events with less than 160 ms in the far offset to 80 ms at 100 ft offset delay following the first arrivals.

A bottom mute of air-wave and ground-roll was applied to remove all the events later than the air-wave, considering that air-wave and ground-roll are so strong in the noise cone that no obvious reflections could be seen. The preceding filtering techniques, including the continuous spectral balancing, did not make significant improvements to the reflections in the noise cone. Thus, bottom muting seemed to be a natural choice in the noise cone. Some shot gathers have ground-roll earlier than air-wave (Figure 13). Muting of such ground-roll should be avoided so as not to damage reflections nearby.

Surgical mute of air-wave was attempted as a comparison with bottom mute, because it was believed that stacking would reduce ground-roll noise significantly, even inside the noise cone. Picking the surgical mute gates for the air-wave took much more than double the time for picking the top or bottom mute, because the ProMAX picking tool would not spatially extrapolate and/or interpolate the surgical mute gates across shot gathers. It will be seen later in the processing tests that surgical mute of air-wave yields poorer quality on stacked section than does the bottom mute. Therefore bottom mute was used instead of surgical mute, unless specified.

3. TIME CORRECTION AND STACKING

Velocity Analysis, NMO and Stacking

Shot gathers were sorted into CMP gathers for velocity analysis, NMO, and stacking. Eleven neighboring CMP gathers were combined and common-offsets were stacked to form a super-gather at each velocity analysis location.

Figure 14 shows an example of stacking velocity analysis for Line I. Because of the low signal-to-noise ratio, the velocity spectra do not have good bulls' eyes. The picking of the velocity points has to rely on the combination of the velocity spectra (left, Figure 14), the fitting of hyperbolas on the super-gather (middle, Figure 14), and the picking of velocity on the constant velocity stacked traces (right, Figure 14). It is difficult to pick accurate stacking velocity functions for Line I; and a velocity difference of 1000-3000 ft/s for an event makes very little difference in the stack.

Figure 15 shows the stacking velocity field for Line I. The stacking velocities were obtained at every 20th CMP location. 11 CMP gathers were combined and same offsets were stacked to form a super-gather at each CMP location for velocity analysis. The stacking velocities for any CMP points not at the velocity analysis locations were linearly interpolated before being applied to the NMO. For this particular stacking velocity field, prior to the velocity analysis, the trace data have been processed using the following steps: VSW, refraction statics, continuous spectral balancing, moderate top mute, bottom mute of air-wave and ground-roll, CMP sort, semblance velocity analysis in super-gathers. It will be shown later in the "processing tests" section that those options are the best combination. Because the velocity field was obtained and interpolated through velocity analysis at sparse CMP intervals (every 20th), it is not smooth and/or evenly distributed. However, no attempt was made to smooth it because a velocity difference of 1000-3000 ft/s makes little difference in the stacked section. In fact, a quite different velocity field provided by Julian Ivanov (1998, personal communication, Kansas Geological Survey) was tried, but very similar stacked section of Line I was obtained.

A stretch mute of 30% was used for the NMO. All offsets were stacked without any weighting factors. Offset limited stacks, i.e., excluding larger offsets from stacking, were tested, but this resulted in inferior stacked sections.

1.5 PROCESSING TESTS

The purpose of the processing tests was to show which processing options (discussed in the previous section) contribute favorably toward a better stacked section. The same velocity field (Figure 15) was applied for NMO regardless of the processing options so that the processing options are the only factors considered in the comparisons, even though different velocities might be more desirable for some options.

Figures 16A--F show the CMP stacked sections of Line I with different processing options for comparison purposes. A constant velocity of 12000 ft/s is used to show an equivalent depth axis. The plotting of the sections in approximately H:V~1:1 helps to easily visualize the dips of structures.

Figures 16A and 16B compare the VSW option. Figure 16A is the stacked section with conventional correlation instead of VSW. Figure 16B is the CDP stacked section with VSW. Refraction statics is included in both cases, but continuous spectral balancing is not applied. Figure 16B shows much higher resolution and much better continuity for reflection images inside the yellow boxes. Figure 16B shows significant improvement of reflection images inside the two green boxes. Therefore VSW correlation is better than conventional correlation.

Figure 16C shows the CDP stacked section without refraction statics correction. VSW is included, but continuous spectral balancing is not applied. There is undulation or non-flatness of the reflectors on the south side (yellow dashed line), compared with Figure 16B. The undulation is caused by a long wavelength statics problem (Line I of Figure 7), which causes false structure. However, the stack quality on the south end (box A) is only a little bit poorer than in Figure 16B, due to small values of the short wavelength statics. The stack quality on the north end (box B) is much poorer than in Figure 16B, because the short wavelength statics values on the north end (Line I of Figure 7) are much greater.

Figure 16D shows the stacked section with continuous spectral balancing added to the flow, in addition to VSW and refraction statics. Compared with Figure 16B, it has slightly overall higher resolution; less north-dipping noise in box A; better continuity in boxes B and C. However, there is not substantial difference between Figure 16B and Figure 16D.

From the comparison of Figures 16A–D, it can be seen that including VSW, refraction statics, and continuous spectral balancing in the processing flow will result in an improved structural image (Figure 16D).

Figure 16E uses the surgical mute of air-wave instead of the bottom mute of air-wave and ground-roll cone. VSW, refraction statics and continuous spectral balancing are included.

Compared with Figure 16D, which used bottom mute of air-wave and ground-roll, Figure 16E has lower signal-to-noise ratio on the entire section, especially on the northern part (inside the box).

Figure 16F shows the stacked section with severe top mute instead of moderate top mute, in contrast to Figure 16D. The severe top mute removed most of the events parallel and close to the first arrivals in the shot gathers (i.e., reverberated refractions in Figure 10). This mute removed the noise that would stack into the first 100 ms in the stacked sections. However, in order to see whether there are any possible reflections on the shallow part (first 100 ms) of the stacked sections, it is preferred to use moderate top mute rather than severe top mute. It just has to be kept in mind that the first 100 ms in the stacked sections is most likely noise, hence the first 100 ms has to be interpreted with caution. Therefore Figure 16D (with moderate top mute) will be used as the final and best stacked section for Line I.

Some reflection events in the stacked sections such as Figure 16D are verified using the filtered shot gathers (Figure 11B). The two green reflections in Figure 11B correspond with the two strong reflections events in the stacked section (Figure 16D). For example, the reflection event of the K-25 Fault, i.e., (CDP 530, 180 ms)-(CDP 890,125 ms), corresponds to the first green event in S1351 (Figure 11), having a T_0 of approximately 130 ms in shot 1351; the Chickamauga bedding reflection, i.e., (CDP 530, 240 ms)-(CDP 890, 180 ms), corresponds to the second green event in S1351 (Figure 11B), having a two-way-time of 200 ms. The events in S1081 (Figure 11B) have nearly linear moveout, being unlikely reflections. This might be the cause for the non-reflection image at the north end of Line I (CDP 200–340). Reflections in other shot gathers of Figure 11B are used similarly to verify the reflection events in the stacked section (Figure 16D).

In summary, the best processing of Line I (Figure 16D) is obtained by including these processing options: VSW, refraction statics, continuous spectral balancing, bottom mute of air-wave and ground-roll, moderate top mute.

1.6 GEOLOGICAL INTERPRETATION OF STACKED SECTIONS

Interpretation of Line I

Figure 17 shows a geological interpretation of the seismic section of Line I, based on discussions with Lemiszki, incorporating the best stacked section (Figure 16D). Figure 17 shows much more detail and quite a lot of difference from the geological cross-section CC' (Figure 4). First, there is no reflection image in Figure 17 corresponding to the KF-1 fault as shown in Figure 4. The KF-1 fault would have to be a south dipping event starting at the north side, extending all the way to the south end, and would have a two-way time of approximately 150–200 ms on the south end, assuming a velocity of 8000-12000 ft/s. Second, the reflection events in Figure 17 do not simply dip to the south, indicating that the subsurface geology is more complicated than is implied by the geological cross-section

CC' (Figure 4). In an area of complex geology such as the K-25 vicinity, it is dangerous to assume surface geology extends all the way down into the subsurface without variations.

On the south side of Figure 17, the major reflections (CDP 500, 200 ms to CDP 870, 130 ms) are interpreted to represent the location of the K-25 Fault (thick black line). The hanging wall of the fault contains chaotically deformed Rome Formation shales and sandstones, so it would be expected to show few coherent reflections. The footwall of the fault is interpreted to contain the Chickamauga Supergroup limestones, characterized by the strong and continuous reflections below the K-25 Fault. Three important lines of reasoning can be made supporting this interpretation. First, the strong and continuous reflection (thick black line) must represent large impedance contrast due to two distinct lithologies. Second, the geologic map (Figure 2) indicates that the Rome Formation (orange) is over the Chickamauga Supergroup, with the K-25 Fault separating them. Third, because the south end of Line I is closer to the K-25 Fault vs. Chickamauga Supergroup surface boundary (location of the cross in Figure 2) than the north end, it is shallower at the south end of the seismic section (Figure 17) than at the north end. Suppose that the K-25 Fault has as dip angle of 15–20 degrees, and also suppose that an average velocity of 12000 ft/s is used for time–depth conversion, then the fault is estimated to be 800–1100 ft in depth when it intersects with Line I. This estimation is roughly consistent with the two-way zero-offset traveltimes of the strong and continuous reflections (thick black line) in the stacked section of Line I. The geological cross-section CC' (Figure 2) is in NW--SE direction, while the seismic section of Line I (Figure 2) is nearly in the N–S direction, intersecting the geological cross-section at an oblique angle.

Therefore, the structural components in the left–right direction of the map (Figure 2) should also have significant contributions to the cross-section of Line I. With this in mind, it is not difficult to explain the K-25 Fault dipping toward the north in the seismic section (Figure 17). Fourth, according to the stratigraphy (Figure 3), the shale vs. limestone inter-beddings in the Chicakmauga Supergroup should provide more layerings and stronger impedance contrasts than the shale vs. dolomite inter-beddings in the Knox Group, where the shale layers are thinner and provide less significant impedance contrasts.

Driller's logs in the area also indicate that limestones of the Chickamauga Supergroup most likely underlie the Rome Formation thrust sheet (Lemiszki, 1999, personal communications). New geological mapping indicates that a window of Chickamauga Supergroup limestone exists to the east of Line I (at the star to the left of CC', Figure 2), which again suggests that the Chickamauga Supergroup underlies the Rome Formation (Lemiszki, 1999, personal communications).

There is a syncline in the Chickamauga Supergroup rocks beneath the K-25 Fault. The geological map (Figure 2) shows the surface location of the syncline (to the left of the K-25 Fault). A revised result for the orientation of the syncline fold axis (N68E/13) based on surface geological mapping (Lemiszki, 1999, personal communications) indicated that the syncline plunges approximately 10 degrees towards Line I with the syncline axis intersecting around CDP 500. Because of the K-25 Fault and the plunging of the syncline toward Line I, the syncline does not out-crop nor does it appear in the near surface in the hanging wall of the K-25 Fault. Instead, the syncline is buried at depth. The seismic section shows that the Chickamauga syncline is 900–1800 ft in depth (yellow box of Figure 17). The field geology indication of the syncline being faulted in places (Lemiszki, 1999, personal communications) is also confirmed by the seismic section (Figure 17) with the minor faults cutting the Chickamauga Supergroup.

There is also an anticline in the Chickamauga Supergroup rocks beneath the K-25 Fault; however, Line I is too short to show the complete seismic image for it. The geological map (Figure 2) shows the surface location of the anticline (to the left of the K-25 Fault and to the southwest of the syncline). Similar to the syncline, the anticline is also buried in depth, under the K-25 Fault. The anticline hinge, however, is further away from or almost at the south end of Line I. So only the reflections from its common limb (northwest dipping) with the syncline at the south end of Line I is seen. Line I is not as perpendicular to dip on the south limb of the syncline as its north limb and that is why bedding dips seen on the south end of Line I are less on the stacked section than the north limb.

Field geological data (Lemiszki, 1999, personal communication) suggested that the Rome Formation was folded with the Chickamauga Supergroup after fault emplacement. In other words, the Rome Formation was thrust on the Chickamauga Supergroup first, and then the whole package was folded. The seismic evidence is that the K-25 Fault parallels the Chickmauga reflections (yellow arrows, Figure 17), and the K-25 Fault partially parallels the overlying Rome Formation.

The secondary thrust faults KF-1, KF-2, KF-3–shown in the geological map (Figure 2) and in the geological cross-section CC' (Figure 4)–are not clearly imaged in the stacked section (Figure 17), because the shallow 100 ms is dominated by noise. A possible interpretation is that the KF-1 and KF-2 faults dipped toward the south (shown in Figure 17, green lines) until they were terminated by another unknown fault (yellow line in Figure 17). The KF-1 and KF-2 faults are bedding parallel faults because there are additional reflections that parallel them, dipping to the south. The KF-1 and KF-2 faults are highly speculative to match with the surface geological mapping. However, there was very little geological evidence in outcrop for the KF-1 and KF-2 faults (Lemiszki, 1999, personal communications). The unmapped fault (Figure 17) was not shown on the geological map (Figure 2) and cross-section (Figure 4) of Lemiszki, possibly due to the absence of outcrops in the area. There is no seismic event corresponding to the KF-3 fault. Unless the seismic imaging for the shallow 100 ms is improved substantially through robust noise filtering techniques, the KF-1, KF-2, and KF-3 faults cannot be interpreted with confidence.

A reverse fault, marked KR-1, is interpreted on the northern part of the seismic section (Figure 17). The reverse fault is interpreted to have a steep dip to the north. The footwall contains the folded beds of the Chickamauga Supergroup, while the hanging wall contains the moderately–steeply dipping Knox dolomites, characterized by the lack of reflectivity, partly due to the thin layer thickness of the shales, partly due to the steep dips. The reverse faulting (KR-1) places Knox Group (older) on Chickamauga Supergroup (younger rocks). However, due to the K-25 Fault placing Rome Formation over Chickamauga Supergroup at an earlier stage, it appears as though the KR-1 places the Knox Group (younger) over the Rome Formation (older); i.e., KR-1 looks like a normal fault at the near-surface, but in fact it is a reverse fault. However, the KR-1 fault is not supported by surface geology and the faults KR-1 and KF-1 have opposite dip directions. One explanation is that the KR-1 fault is a deep fault which has not out-cropped to the surface and that the KF-1 fault is only a shallow fault and thus does not properly show up in the seismic section. Another explanation is that the KR-1 reverse fault is real while the KF-1 thrust fault is non-existent. Both explanations are reasonable.

On the south end of the section (Figure 17), there is an event between 200 and 400 ms, (yellow dashed line). This event is cutting through the Chickamauga Supergroup reflections without displacements, so it might not be real geology. It may be either reflections from steep structures or sideswipe. The prestack depth migration will clarify this issue.

The complex deformational history in the area makes it difficult to interpret the subsurface structures solely based on poorly constrained surface geological model (Figure 2 and Figure 4) and seismic data (Figure 17). Because the area is within a complexly deformed hinge of a footwall fault-propagation fold and it has undergone multi-stage deformations, it is unnecessary to strictly adhere to thrust belt style structures and timing relationships. In other words, other structural styles such as reverse and/or normal faulting are also possible, even if they are not supported by the poorly constrained surface geological data.

The seismic section (Figure 17) shows much slower variations of dips for subsurface structures, while the geological mapping shows much faster variations of surface dips of out-cropped rocks (refer to Figure 2 for surface dips near Line I). This substantial difference is understandable because the K-25 is in the complex structural deformation area, so we cannot simply extend surface structures downward (just as in the cross-section CC' of Figure 4) without consideration of structural changes in a 3D perspective.

Extension of Geological Interpretation to Nearby Seismic Lines (E1, E2, F1, F2)

Figure 18 shows the extension of geological interpretation to the nearby seismic lines (E1, E2, F1, F2), the surface locations of which were shown in Figure 5. The seismic sections were processed using a slightly different processing procedure (Liu et al., 1997) from the processing of Line I. The processing features included Vibroseis whitening and refraction statics, but without continuous spectral balancing. Unlike Line I, the seismic images of lines E1, E2, F1, F2 are not so clear.

Line E1 (Figure 18A) is located across the surface location of the Whiteoak Mountain Fault, separating the Rome Formation and the Chickamauga Supergroup at approximately CDP 600 (Figure 2 and Figure 5). Due to the high noise level in the southern part (CDP 200–570) of the stacked section, the subsurface location of the Whiteoak Mountain Fault cannot be established with confidence. The northern part (CDP 570–690) shows some coherent reflections. The yellow dashed lines shows the present interpretation. The southern part is dominated by diffraction noise. This difference in character is also seen on

Line I where it is interpreted to be the contrast between the sharp reflections in the Chickamauga Supergroup and the lack of reflections in the Knox Group. On this basis, a fault is interpreted between the Chickamauga Supergroup and Knox Group on Line E1 (green line, Figure 18A).

Line E2 (Figure 18B) crosses the surface location of the K-25 Fault at approximately CDP 540 (Figure 5). The K-25 Fault separates the Rome Formation (above) and the Chickamauga Supergroup (below). There are two unmapped reverse faults. The north dipping reverse fault (NR, Figure 18B) places the Knox Group (lower) and the Chickamauga Supergroup (upper) in contact. On the north side of the fault, the Chickamauga Supergroup is characterized by reflections. On the south side of the fault, the Knox Group is characterized by the lack of reflections. The south dipping reverse fault (SR, Figure 18B) separates the Knox Group (upper) from the Chickamauga Supergroup (lower). The entire Chickamauga–Knox package is up-thrown on the south side of the fault, with a vertical displacement of approximately 100 ms (two green dots as reference, Figure 18B). According to cross-cutting relationship, at first the north dipping reverse fault was formed. Then the south dipping reverse was formed. Then the K-25 Fault was formed, cutting through the south dipping fault. Even though the Chickamauga anticline did not appear on Line I, because it was further to the south end of Line I, it shows up clearly on Line E2 with an apex at approximately CDP 480 (Figure 18B). The location of the anticline on Line E2 is consistent with the surface location shown on the geological map (Figure 2 and Figure 5). Line E2 has remarkable similarity to Line I in that they both have roughly consistent depth for the K-25 Fault, the same stratigraphic units (Rome

Formation, Chickamauga Supergroup), even the same time-thickness for the Chickamauga Supergroup.

Line F1 (Figure 18C) is located across the surface location of the K-25 Fault, separating the Rome Formation and Chickamauga Supergroup at approximately CDP 230. The K-25 Fault separates the Rome Formation (above) and the Chickamauga Supergroup (below). Because the 100 ms is dominated by reverberated refractions in the shot gathers, the interpretation of the K-25 Fault is highly speculative. There are two interpreted faults. Line F1 is too short to be really useful.

Line F2 (Figure 18D) crosses the K-25 Fault at approximately CDP 600 on surface. The K-25 Fault separates the Rome Formation (above) and the Chickamauga Supergroup (below). The Rome Formation is shallow in the section and is interpreted to be chaotically deformed, so there is not any good reflection. The Chickamauga Supergroup is interpreted to be faulted in many places (green lines in Figure 18D) with time displacements, while the Knox Group is characterized by the lack of reflections.

In summary, the additional seismic sections (E2, F1, F2) support the identification of the K-25 Fault in the interpretation of Line I. The consistency of the time-thickness of the Chickamauga Supergroup in Line I and in Line E2 is the assurance for the identification of the Chickamauga Supergroup. The interpreted faults in the seismic lines suggest that additional faults exist in depth, even though they have not been mapped on surface geology.

1.7 PRESTACK DEPTH MIGRATION

The final stacked section (Figure 17) has a vertical axis in time rather than depth. The result of processing in time is that artifacts may occur, having no geological counterpart. Common examples of this are "bowties" and diffractions (Sheriff, 1991).

Because the structures of Line I are complex, including stratigraphic dips greater than 35 deg., a syncline, and several stages of faulting, the assumptions (small dips, gentle curvature, gradual velocity variation, and hyperbolic moveout) for CMP stacking do not hold well. This will result in poor stacking, mainly for the northern half of Line I such as inside the yellow box of Figure 17. Migration is required because events from steeply dipping structures will be significantly mispositioned on a stacked section. Post-stack migration is inappropriate because the stack is not a clear image and is not equivalent to a zero-offset section. Prestack time migration is inappropriate because lateral velocity variation is rapid, not gradual. Prestack depth migration is appropriate because it allows for ray bending at velocity contrasts and therefore accommodates rapid velocity variation. Therefore it is decided to apply prestack depth migration to improve the imaging of Line I.

One of the ultimate goals is to know the depth of horizons and faults under the K-25 seismic lines. A further benefit of prestack depth migration is that it will obtain horizons and faults in terms of depth rather than two-way reflection time so that the reflection images are more like geology. The depths that could be obtained from vertical ray depth conversion of times would be far from accurate. First, the seismic ray paths are not vertical for complex structures such as with steep dips and curvatures. Second, the interval velocities derived from the stacking velocities by the Dix equation would be in error, because the stacking velocities are highly dip-dependent. The prestack depth migration, through migration focusing analysis, provides more accurate interval velocities, which are relatively independent of structural dip. The improved and more accurate velocity–depth model in turn results in more accurate prestack depth migration, placing reflections more closely at their correct spatial locations.

Prestack depth migration will collapse the conflicting dips of the bowtie at the axis of the syncline in the Chickamauga Supergroup (inside the yellow box of Figure 17). It will also help to clarify the identity of the crossed events on the southern end of Line I (Figure 17, question mark below 300 ms).

Prestack Depth Migration Processing Procedure for Line I

Kirchhoff prestack depth migration (McMechan et al., 1998, Pasasa et al., 1998) in ProMAX v 6.0 was applied to Line I, using the following processing procedure:

(1) Vibroseis whitening

(2) Correlation

(3) Vertical stacking

(4) Refraction statics

(5) Notch and band-pass filtering

(6) Continuous spectral balancing

(7) Trace killing

(8) Severe top muting

(9) Bottom muting of air-wave and ground-roll cone

(10) Sorting of traces into common-offsets (absolute offsets)

(11) Offset binning

(12) Interpretational prestack depth migration velocity analysis

(13) Kirchhoff prestack depth migration of (11), using velocity from (12)

(14) Stacking migrated common-offset gathers of (13)

(15) Displaying stacked depth-migrated section of (14)

(16) Sorting migrated common-offsets of (13) into common image gathers (CIG)

(17) Displaying CIG gathers in Variable Area and Wiggle (VAW) mode

(18) Updating the migration velocity model from (12) and using (17) as assistance

(19) Repeating (12)–(18) until satisfactory depth migration result is obtained

Descriptions of Prestack Depth Migration Processing Procedure

Steps (1)–(11): Trace Processing and Sorting into Common-Offset (DMO offset bins). Steps (1)–(9) are the best trace processing procedure explained earlier in the preprocessing, filtering and muting sections. Steps (10)–(11) sort trace data into common-offset bins.

Step (12): Interpretational Prestack Depth Migration Velocity Analysis. The velocity–

depth model is updated using previous prestack depth migration results as inputs. Either the CIG gathers or the stacked migrated section are displayed in overlays on top of the interval velocity–depth model. This is helpful to show how well the migrated section matches with the velocity–depth model. The adjustment of interval velocities brings changes of events (flatness) in the CIG gathers (Stork and Clayton, 1989, 1991), thus enabling the modification of velocities locally without having to re-do a full prestack depth migration. However, velocity variations shorter than an array length of the CIG gather cannot be properly handled due to the 1-D ray path assumption of the velocity adjustment algorithm (Stork and Clayton, 1989, 1991).

Step (13): Kirchhoff Prestack Depth Migration. Common-offset gathers and velocity–depth model are input into the Kirchhoff prestack depth migration. In a complex velocity–depth model, the ray paths are often complicated, resulting in multi-values for the arrivals from an imaging point in depth to a surface point. The maximum energy arrival condition uses the arrival time with the maximum amplitude (energy) among all the arrivals as an imaging condition in the Kirchhoff prestack depth migration. The maximum energy arrival imaging condition yields better prestack depth migration than the first arrival imaging condition, because the former represents the most energetic arrival time. In the Kirchhoff depth migration, the input velocity–depth model is smoothed (with aperture 50 ft) to alleviate ray-tracing problems, such as shadow zones and ray-crossings, in the calculation of imaging conditions. The result of the Kirchhoff prestack depth migration is the depth-migrated common-offset gathers.

Step (14): Stacking Migrated Common-Offset Gathers. The migrated common-offset gathers in (13) are stacked to make the stacked depth-migrated section.

Step (15): Displaying Stacked Depth-Migrated Section. This is the "Screen Display" of the depth-migrated section as a final result of the prestack depth migration.

Steps (16)–(17): Examining Common Image Gathers (CIG). Migrated common-offset gathers are sorted into CIG gathers, then displayed in VAW mode. This alternative VAW display mode allows examining CIG gathers in much finer detail (higher resolution) than the Variable Density display mode that is part of the "Interpretational Prestack Depth Migration Velocity Analysis". The extra display effort in VAW is rewarding for better identification of reflections from noise in a CIG gather.

Steps (18)–(19): Iterating for updating the velocity model and prestack depth migration-process. The velocity analysis, velocity update and prestack depth migration are iterated until the depth migration result is satisfactory, being reasonably geologically interpretable and/or closely matching a structural model.

Velocity Model Building for Kirchhoff Prestack Depth Migration

A velocity–depth model is the prerequisite to perform prestack depth migrations and the quality of the prestack depth migration is dependent on the accuracy of the velocity–depth model compared with the velocity–depth model of the earth. In building an initial velocity–

depth earth model, all available information on rock-material velocities is considered.

Rock-Material Velocities

The first source of velocity information is from the tomographic solution of refraction statics (Figure 7). The refractor velocities of Line I show a low velocity of approximately 10000 ft/s in the middle of the line, and a high velocity of approximately 15000 ft/s at each end of the line. However, the refractor has a depth of less than 200 ft. This is very shallow compared with the reflections, which are at a depth of 800 ft or deeper (equivalent depth in Figure 17 using a velocity of 12000 ft/s).

The second source of velocity information is from first-arrival apparent velocities from shot gathers. The velocities are in the range of 8000-13000 ft/s. Similar to the tomographic solution in the previous paragraph, these velocities are for surface rocks and/or the shallow refractors (less than 200 ft in depth).

The third source of velocity information is from the VSP velocity measurements in the Oak Ridge Reservation (Doll et al., 1998). The measurement site is approximately 5 miles away from the K-25 Line I. The velocities range from 4921 ft/s at surface to 10826 ft/s at depth of 525 m. Even though the two sites have similar lithologies of similar age, they have different stratigraphy (formations). Therefore it is expected that the two sites will have somewhat different vertical and lateral velocity distributions.

The fourth source of velocity information is from the ultrasonic velocity measurements of

Kolich (1974) for the Price Mountain rocks in Montgomery County, Virginia. The cores measured came from similar stratigraphic and lithologic units to those that occur at the K-25 site. One factor that may limit the usefulness of these velocities at the K-25 site is the fact that the Price Mountain is hundreds of miles away from the K-25, Oak Ridge, TN. Figure 19 summarizes the relevant velocity measurements of Kolich (1974). Only the velocity values in the first column of the velocities, i.e., at 200 atm (depth of 1968 ft), will be relevant for the depth of interest for the K-25, because 1968 ft is already too great for near-surface targets. Lithology is the most important factor controlling the range of the velocities. To quote a few representative rock samples, velocity in shale (Rome shale)= 11155 ft/s; velocity in sandstone (Copper Ridge sandstone) is (17946 + 18602)/2 = 18274 ft/s; velocity in limestone (Chepultepec limestone)=21161 ft/s; velocity in dolomite (Kingsport dolomite) is 20177 ft/s. The Chickamauga Supergroup was not included in Kolich (1974), but it would be similar to any of the limestone units such as the Chepultepec limestone in the Knox Group.

The first three kinds of velocity information are restricted to only the shallowest reflectors in the seismic data. The 4th kind of velocity information may not be representative of the stratigraphic and lithological units at the K-25 site and there are no borehole logs at the K-25 site to check this. Nevertheless, they can be used as general geological constraints, limiting the interval velocities for specific lithologic/stratigraphic units within reasonable range. For example, if we assume the layers above the K-25 Fault (Figure 17) to be of Rome Formation, we can limit the Rome sandstone velocity from 18274 ft/s (Copper Ridge sandstone) and the velocity of Rome shale from 11155 ft/s (Rome shale in Figure

19). Because interval velocities are required in the velocity–depth model for our prestack depth migration, the velocities we obtain must correspond to the velocities of the stratigraphic and lithologic units known to exist at the K-25 site. If the velocities were not typical of shales, sandstones, dolomites and limestones (these are known to exist in the K-25 area) and/or their combinations, but of mafic igneous rocks, for example, which could not possibly exist according to the geological mapping, there would be a major problem.

Updating a Velocity–depth Model Using Residual Moveout

The most reliable and meaningful velocity information for a velocity–depth model for the prestack depth migration is obtained through observation of residual moveout in common image gathers (Ratcliff and Brzostowski, 1997; Zhu et al., 1998). This is practical because the interval velocity information is derived from the seismic data itself, i.e., from the residual moveout in CIG gathers.

Figure 20 is a schematic diagram showing the alignment pattern (residual moveout) for a reflection event in a CIG gather, in response to the accuracy of migration velocity. A proper velocity makes the reflection event aligned flat for all offsets (properly-migrated). A low velocity makes the reflection event tailed-up toward increasing offsets (under-migrated). A high velocity makes the reflection event tailed-down toward increasing offsets (over-migrated).

The velocity analysis and the velocity model building follow a layer-stripping approach.

That is, if an event is not flattened by the prestack depth-migration process, then the velocities for the layers above that event must be adjusted, until the primary reflection events above that event are all flattened. This process requires working from the top downward. Due to the noise problems and the lack of reflections in the shallow part of the seismic section of K-25 Line I, average interval velocities to the first strong reflector were sought. Average interval velocities for deeper layers were also used, because it would be impossible to consider very thin layers. This kind of averaging is acceptable as long as the major reflection events are properly migrated.

The ProMAX "Interpretational Depth Migration Velocity Analysis" uses a 1-D algorithm (Stork and Clayton, 1989; Stork, 1994) to adjust velocities and to make residual time shifts in CIG gathers. This is useful except in cases of strong noise interference and/or very complex structures. Additional methods, including trial and error of migration velocity with full prestack depth migration, and examination of CIG gathers in VAW display, were relied upon heavily to derive a velocity–depth model for the prestack depth migration of the noisy data set of Line I.

Kirchhoff Prestack Depth Migration Using First Velocity–Depth Model

Figures 21A, B, C are the first set of figures (velocity–depth model, prestack depth-migrated section and CIG gathers) for the prestack depth migration of Line I. Prominent reflection events are marked with green ellipses and letters in Figures 21A, B, C to show their correspondence in migrated section and in CIG gathers.

Figure 21A is the interval velocity–depth model for the prestack depth migration, with the migrated CIG gathers displayed as overlay.

In the construction of the interval velocity–depth model, the stacked section (Figure 17) was used to define the initial structural boundaries. A few trial and error migrations using velocities guided by the considerations of the previous section and adjustments of the initial structural boundaries were tested with full prestack depth migration. The location of the fault or the velocity discontinuity below CDP 400–500 (black ellipse) was defined arbitrarily. The layers and velocities deeper than 1500 ft were also defined somewhat arbitrarily.

The overall match of the velocity–depth model with the depth migration indicates that the velocity–depth model is reliable.

The "V proper", "V low", "Dipping noise such as residual air-wave and ground-roll" and "Events migrated with too low velocities" areas will be explained better after the introduction of Figure 21C because these migration features require the examination of the CIG gathers.

Figure 21B is the prestack depth-migrated section. Events A, B, and C have been well migrated, as indicated by the overall flatness of events in the overlay display (events A, B, C in Figure 21A), and by the continuity and strong amplitudes of reflections in the depth-migrated section (events A, B, C in Figure 21B). Event D becomes weaker toward the north. Events E and F are fairly well migrated, as indicated by the overall flatness of events in the overlay display (Figure 21A) and by the strong amplitude and continuity of events in Figure 21B. The very weak and curving-up events (for example, CDP 730-930 and Depth 0–500 ft) should be considered to be migration noise. The two regions that need substantial velocity adjustments are marked to indicate the poor migration quality due to incorrect velocities.

Figure 21C is the VAW display for detailed examination of a few CIG gathers. Compared with the overlay display (Figure 21A), the VAW display mode provides much higher resolution to examine reflections against noise; to evaluate the flatness of events in CIG gathers; and to determine the direction of velocity adjustment.

The "V proper" (Figure 21A), areas show that the reflection events were properly migrated, giving an overall flat appearance. The "V low" areas show reflection events that were over-migrated. The south-dipping noise (CDP 650–780, Depth 1000–2000 ft) was caused by residual air-wave and ground-roll noise earlier than air-wave. This can be seen clearly in the VAW display of the CIG 750 (red lines, Figure 21C).

The events labeled "Events migrated with too low velocities" (red lines, north-dipping) correspond to events D and J. They appear as north-dipping noise because the overlay display is so compressed horizontally. However, in the VAW display (Figure 21C), the depth difference between the near-offset and the far-offset is not so substantial (less than 100 ft). Thus the events will stack well to result in fairly strong amplitudes in the migrated section (Figure 21B). Events D and J are interpreted to be reflections.

In CIG 350 (Figure 21 C), no events have been properly migrated. Judging from the migrated section (Figure 21B), modifying the velocities below event F might improve the migration of events G, H, I in CIG 350.

For CIG 450 (Figure 21 C), the event at 600 ft is well migrated. This corresponds with the migrated event E in Figure 21B. No other events are properly migrated.

For CIG 550 (Figure 21 C), the event at 1250 ft is well migrated, while the event at 1700 ft is migrated with low velocity. The events under CDP 550 in Figure 21A have the strong south-dipping appearance, indicating very low migration velocity. However, the CIG 550 in Figure 21C shows that the depth differences between the near and the far offsets are within tolerable limit, yielding an acceptable depth image.

For CIG 620 (Figure 21 C), events at 1000 ft and 1300 ft are well migrated. The event at 1700 ft is over-migrated with a low velocity. The events shallower than 900 ft are considered noise.

For CIG 750, the south dipping events (corresponding to red lines under CDP 750 in Figure 21A) can be easily identified as noise having large slopes (CIG 750 in Figure 21C). Those events are most likely residual air-wave and ground-roll noise earlier than air-wave. The reflection events at 1100 ft and 1500 ft of CIG 750 are fairly migrated, only with slightly higher velocity, in contrast to the "too high velocity" impression at CDP 750 of Figure 21A.

For CIG 820, several events (at 1000, 1400, 1600 ft) have been properly migrated.

Kirchhoff Prestack Depth Migration Using Second Velocity–Depth Model

Figures 22A, B, C are another set of figures (velocity–depth model, prestack depth-migrated section and CIG gathers) for the prestack depth migration of Line I using the second velocity–depth model.

In Figure 22A, the velocity value for the bottom layer is changed from 28,000 ft/s (in Figure 21A) to 24,000 ft/s. The fault boundary (black ellipse in Figure 21A) is removed in the current model. Instead, just smooth layer boundaries are used so as to eliminate migration artifacts (differences in depth across the abrupt velocity discontinuity) in the depth image.

Compared with Figure 21B, the structural images in Figure 22B (CDP 370–500, black ellipse) are more continuous, due to the smoother velocity model in Figure 22A.

In Figure 22C, not all reflection events could be flattened, even though attempts to adjust the interval velocities (with reasonable rock velocities) above them were made. In contrast, event J (below 2500 ft at CIG 550) could not be flattened no matter how the velocities above it were adjusted.

The prestack depth migration using the second velocity–depth model is considered to be more reliable because the fault in the first velocity–depth model (Figure 21A) was not defined with much geological reasoning, as evidenced by the stacked section (Figure 17).

1.8 GEOLOGICAL INTERPRETATION OF DEPTH-MIGRATED SECTIONS

The geological interpretation will be based on the second depth migration (Figure 22). The depth migration (Figure 22B) uses different labeling from the stacked section (Figure 17), because different features need to be discussed. However, the depth-migrated section (Figure 22B) shows structural features similar to the stacked section (Figure 17).

Similar to the interpretation of the stacked section (Figure 17), the K-25 Fault is interpreted to be represented by the strongest events A and B (green lines, Figure 22B), in the depth range of 900–1300 ft. The K-25 Fault places the Rome Formation on top of the Chickamauga Supergroup. The Chickamauga Supergroup has continuous bedding reflection events C and D, (green lines, Figure 22B). The bottom of the Chickamauga Supergroup is interpreted to be represented by event J. Therefore, the total thickness of the Chickamauga Supergroup is approximately 1400 ft, being less than the total thickness (2122 ft) shown in stratigraphic column (Figure 3). The low velocity for approximate depth used in Figure 17 gives smaller apparent depths and thicknesses. Therefore, the depths and thicknesses from the prestack depth migration (Figure 22B) are much more reliable.

There is a new structural feature on the depth-migrated section (black dashed lines at the south end in Figure 22B) which was not present in the stacked section (Figure 17). It looks like a fault or fault zone (flower structure characteristic of compressive tectonics). One explanation is that the prestack depth migration has reduced the smearing effects present in CMP stacking, thus the prestack depth migration has higher spatial resolution. Therefore the structural images become clearer, revealing additional features not imaged through CMP stacking.

The reflection events E, F, G are more uniformly dipping toward the south and have much higher signal-to-noise ratio than the south-dipping events in the stacked section (Figure 17) at similar locations. The lower signal-to-noise ratio in the latter was mainly due to the poor stacking of the dipping layers. It is possible that event E corresponds to the KF-1 fault and event G corresponds to the KF-2 fault, assuming that the KF-1 and KF-2 faults are bedding-parallel faults. Events E, F, G extend downwards to the south and terminate against the same north-dipping event (inside the polygon labeled "sole faulting"). Because the KF-1, KF-2, KF-3 faults intersect on the surface (Figure 2), they have to intersect/merge somewhere in depth (Kevin Smart, 1999, personal communication). One scenario is that the KF-3 fault occurred first, then the KF-2 fault, then the KF-1 fault. All of the 3 faults originally began from a common surface–the sole. Then came the K-25 Fault, placing the already deformed Rome Formation on top of the Chickamauga Supergroup. This scenario is consistent with the cross-cutting relationship characterization the geological mapping (Figure 2).

The Chickamauga syncline is not as well imaged in the depth-migrated section (Figure 22B) as in the stacked section (Figure 17). The axis of the Chickamauga is estimated to be at CDP 570 at a depth of 1300 ft. This places the axis of the Chickamauga syncline further to the north on the prestack depth-migrated section than on the stacked section.

The south dipping crossed event (yellow dashed line, Figure 17) at the south end of the stacked section becomes much weaker in the depth-migrated section (Figure 22B). Therefore it is probably not a primary reflection event.

1.9 CONCLUSIONS

The best CMP stacked section of Line I is obtained from the following processing: VSW, refraction statics, notch and band-pass filtering, continuous spectral balancing, bottom mute of air-wave and ground-roll and moderate top mute, and velocity analysis. The complete processing improved the signal-to-noise ratio, the continuity of reflections, and the resolution of Line I.

From the stacked section of Line I and associated lines nearby, it is possible to obtain a consistent interpretation of major stratigraphic and structural features. These features include the following: stratigraphic units (Chickamauga Supergroup, Knox Group, Rome Formation), faults (K-25 Fault, Whiteoak Mountain Fault, KF-1, KF-2, KF-3 mapped-faults), and the Chickamauga syncline.

The consistent time-thickness of the Chickamauga Supergroup in the stacked sections of Line I and Line E2 is evidence that correct geological boundaries of the Chickamauga Supergroup have been picked.

The seismic sections are consistent with the geological mapping regarding the approximate lateral locations of the mapped-faults and the axis of the Chickamauga syncline.

The interpretation of the KF-1, KF-2, KF-3 mapped-faults in seismic cross-section is different from the geological cross-section CC'. These faults truncate against the K-25 Fault rather than simply extending downward without change and termination.

Several unmapped-faults were interpreted on the seismic images of Line I and nearby seismic lines. This suggests that there are more faults than are mapped. Some faults might not outcrop, while others might have not reached the surface or are truncated in depth.

The geological dips mapped on the surface are much more variable and larger than dips seen on the seismic data at depth. In areas with thrust faults, it is common for faults to be less steep at depth.

Ideally, we hope the depths and thicknesses obtained from seismic imaging (stacked sections and prestack depth-migrated section) can be verified by borehole rock sampling or by well logs. Unfortunately, such data are not available because drilling would expose underground wastes to the surface. Nevertheless, prestack depth migration is useful to obtain depth images more accurately than the depth conversion from stacked sections. Prestack depth migration shows the depth to the K-25 Fault to be 1000-1500 ft, and depth to the Chickamauga Supergroup to be 1000-2500 ft, and the thickness of the Chickamauga Supergroup to be 1400 ft.

The depth and thickness values from the prestack depth migration might not be accurate to some extent, mainly due to the low signal-to-noise ratio in the data set of Line I. The inaccurate velocity–depth model, in turn, results in inaccurate depth migration. For instance, event D (in Figure 22B) could not be flattened for its northern part. Event D and event J are under-migrated no matter what realistic rock velocities were used. The depth values for event D and event J should be smaller than appeared in the prestack depth-migrated section (Figure 22B). The depth values, and even the depth values for the K-25 Fault and the Chickamauga Supergroup, should not be regarded as absolutely accurate values. Instead, they should be regarded as much more accurate estimation than obtained from CMP stacking, which uses two-way-time as the vertical axis.

The prestack depth migration reveals one structural discontinuity (fault zone, i.e., flower structure) that was not apparent on the stacked section of Line I. The prestack depth migration has reduced spatial smearing significantly, thereby increasing the structural resolution. This additional discovery is a reliable interpretation of structure and depth. It would be significant for making decisions for waste monitoring and/or remediation.

Due to the low S/N ratio in the reflection seismic data of Line I, especially inside the air-wave and ground-roll cone, the seismic data processing presented in this chapter needs to be further improved. Future work should include more robust filtering techniques, such as local tau-p filtering (available in some processing software packages) and Local Slant-Sum Adaptive Noise Removal (Appendix B). These techniques are based on the apparent velocities and/or slopes of noise, and therefore might be useful to remove linear coherent noise such as ground-roll, air-wave and reverberated refractions, considering that these noise modes are characterized by distinct slope patterns.

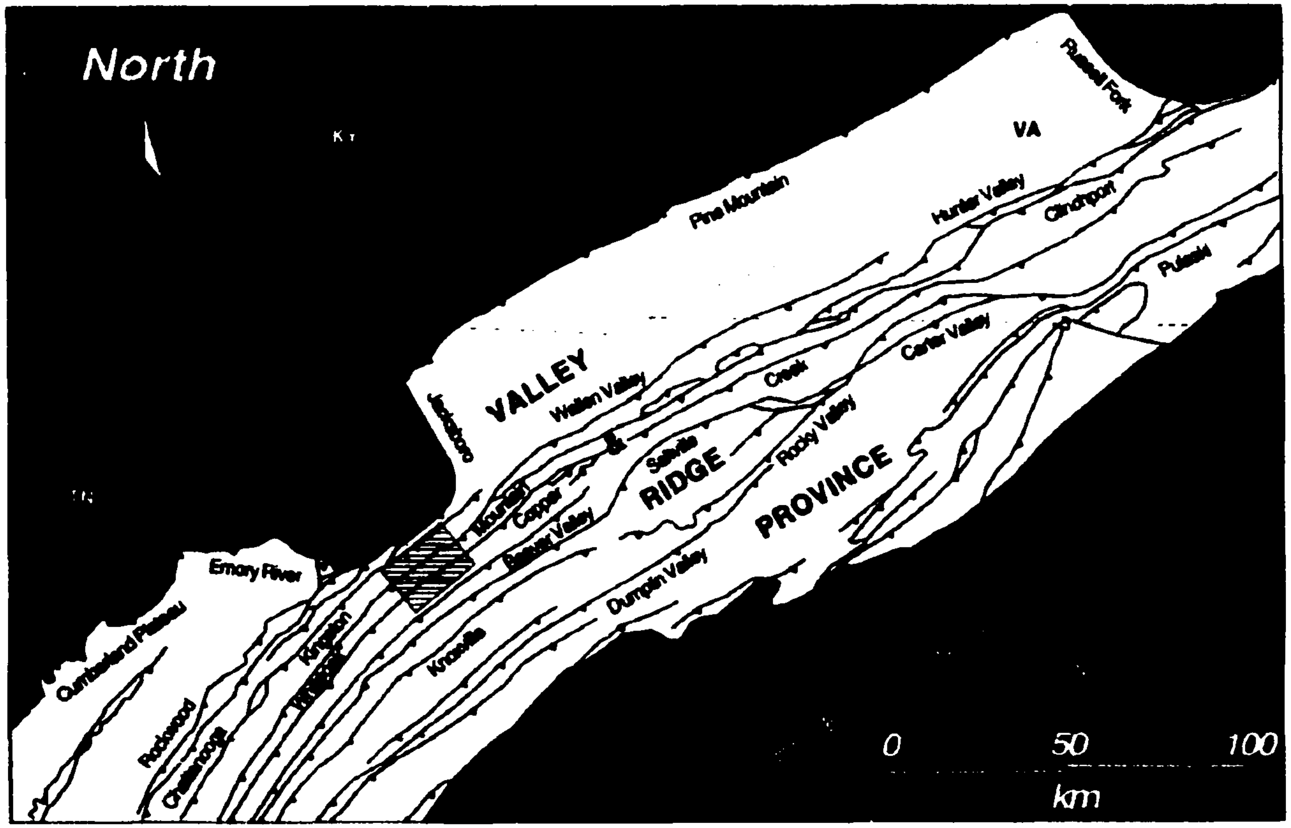

Figure 1 Regional structural setting of the study area (hatched area), the Oak Ridge Reservation, near Oak Ridge, Tennessee (Lemiszki, 1994).

Figure 2 Geological map of the Oak Ridge Reservation. The K-25 Plant is located to the right of BB' (modified from Lemiszki, 1994). The area is characterized by multiple stages of thrust faulting, affecting the lower Paleozoic rocks. Based on the cross-cutting relationship, it is inferred that the chronological order of the faulting is KF-1 Fault, K-25 Fault, then Whiteoak Mountain Fault. The color codings represent the surface stratigraphic units corresponding to those illustrated in Figure 3. The fold axes of the syncline and the anticline are also shown. The star next to CC' indicates a window of the Chickamauga Supergroup. The cross on the K-25 Fault indicates a reference point from where dip angle for the K-25 Fault is calculated.

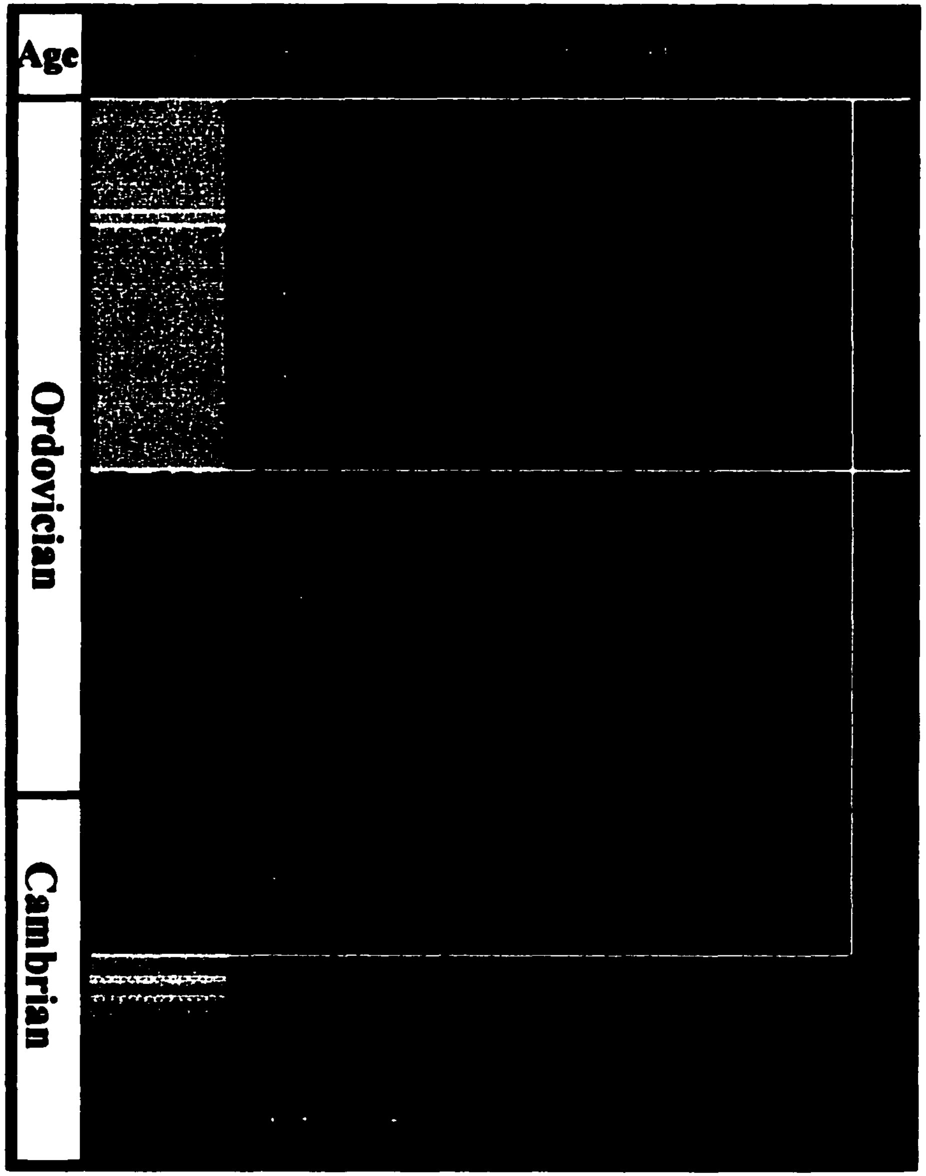

Figure 3 Stratigraphic units of the Oak Ridge Reservation (modified from Lemiszki, 1994). Lower Paleozoic rocks have thick sequences of limestones, dolomites, and clastics. Shale layers occur in most formations as interbedding.

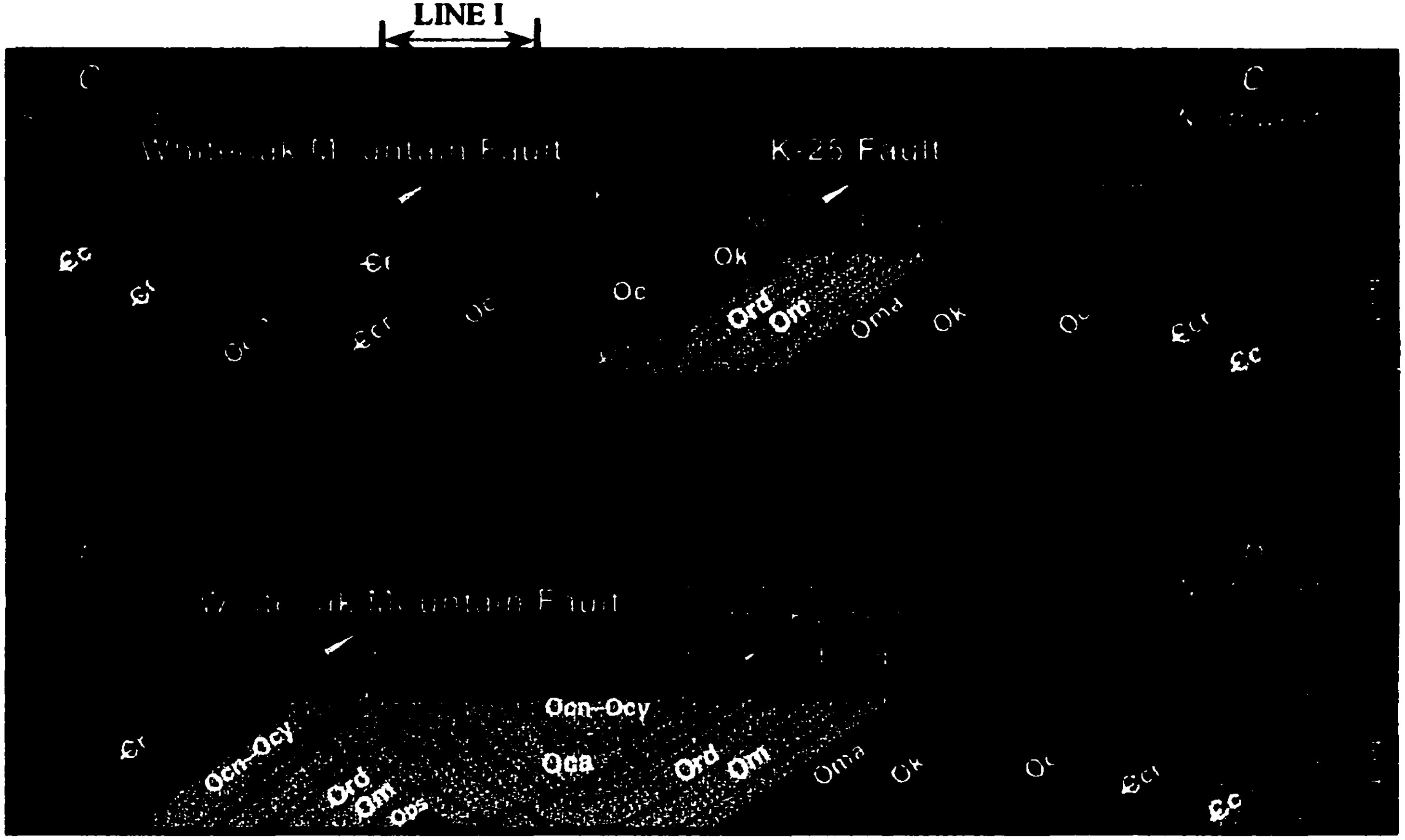

Figure 4 Geological cross-sections BB' and CC' in the K-25 area (Figure 2), based on surface geological mapping. Due to the lack of data in depth, the interpretations of geological boundaries were hypothetical, needing to be validated by seismic reflection data. The cross-section CC' will be of major significance because it is taken near Line I (shown projected into the cross-section CC') (modified from Lemiszki, 1994).

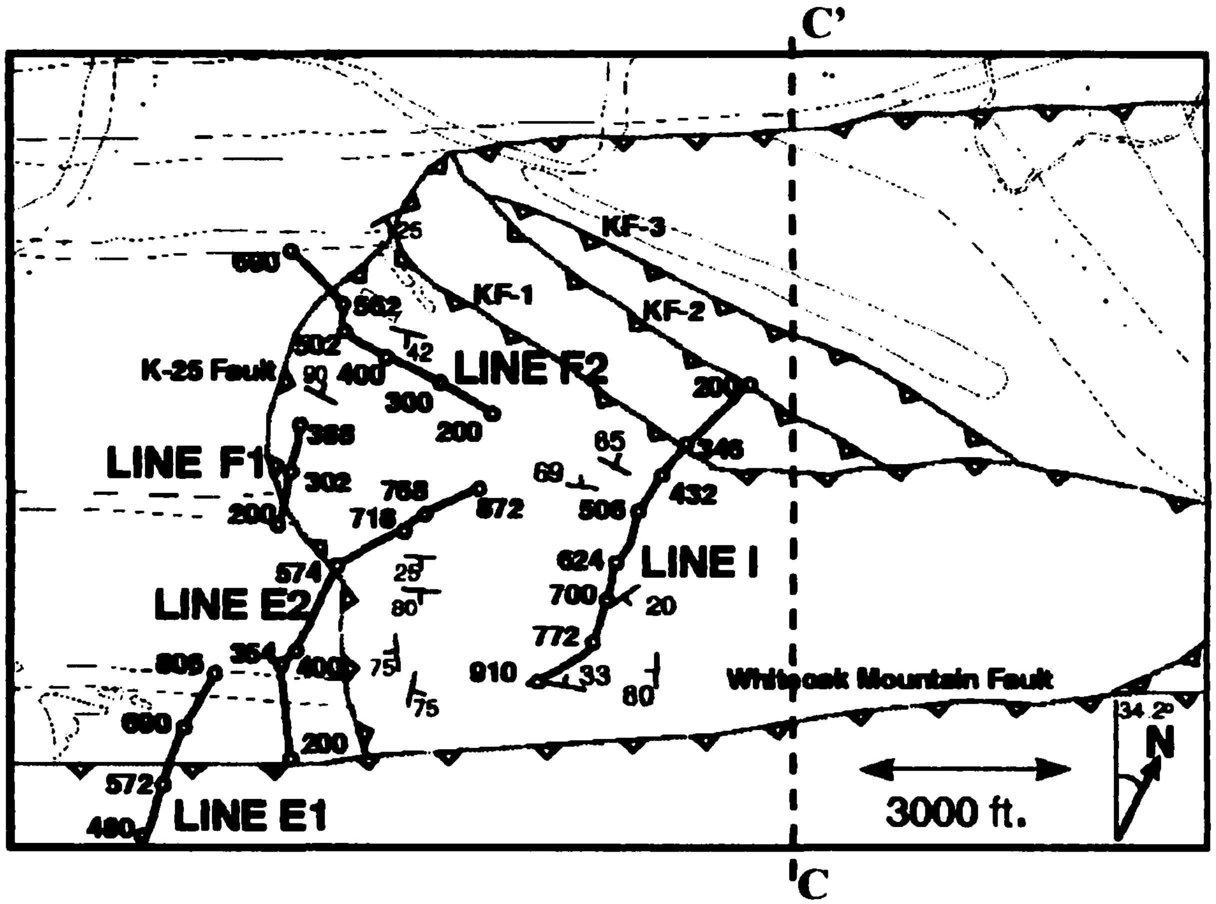

Figure 5 Locations of the 5 seismic lines that were processed (modified from Doll et al., 1996; Liu and Doll, 1997). The seismic lines were designed to be near the faults and to be approximately perpendicular to the thrust faults, so that the seismic sections are approximately in the fault dip direction. The numbers along the seismic lines are CDP numbers. The dip symbols indicate the strikes and dips of rock units measured from surface mapping. Notice the relative location of Line I with respect to the geological cross-section CC' (Figure 4).

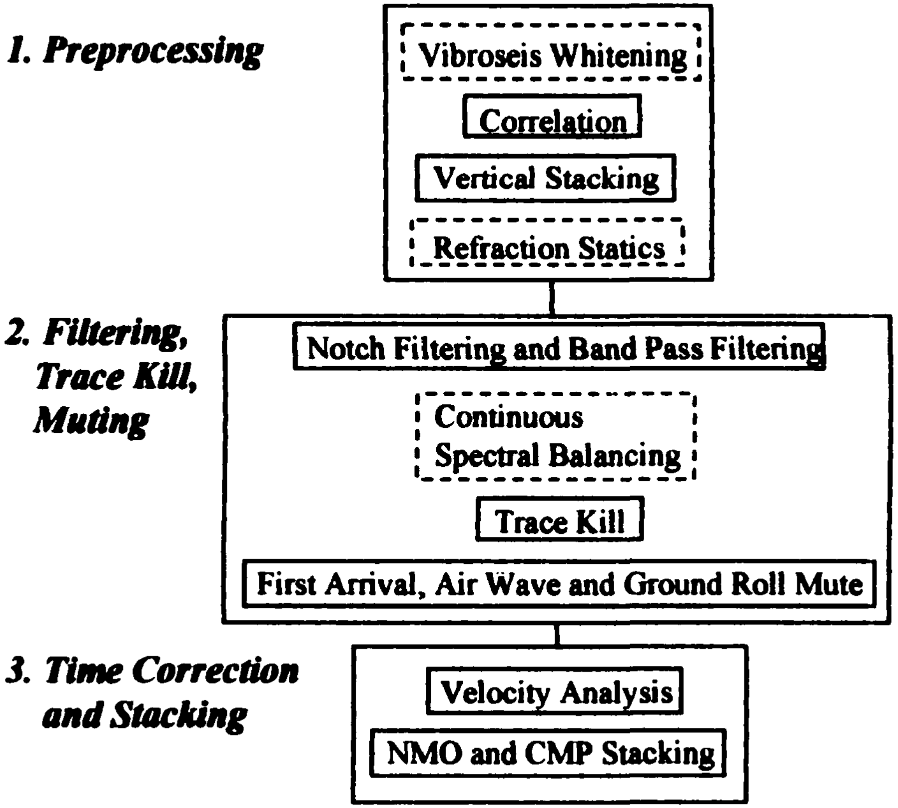

Figure 6 Processing flow chart for Oak Ridge K-25 Line I. The boxes with the dashed frames are options for comparison purpose. Refer to the text in the section "PROCESSING TESTS" to see how the options are included for comparison.

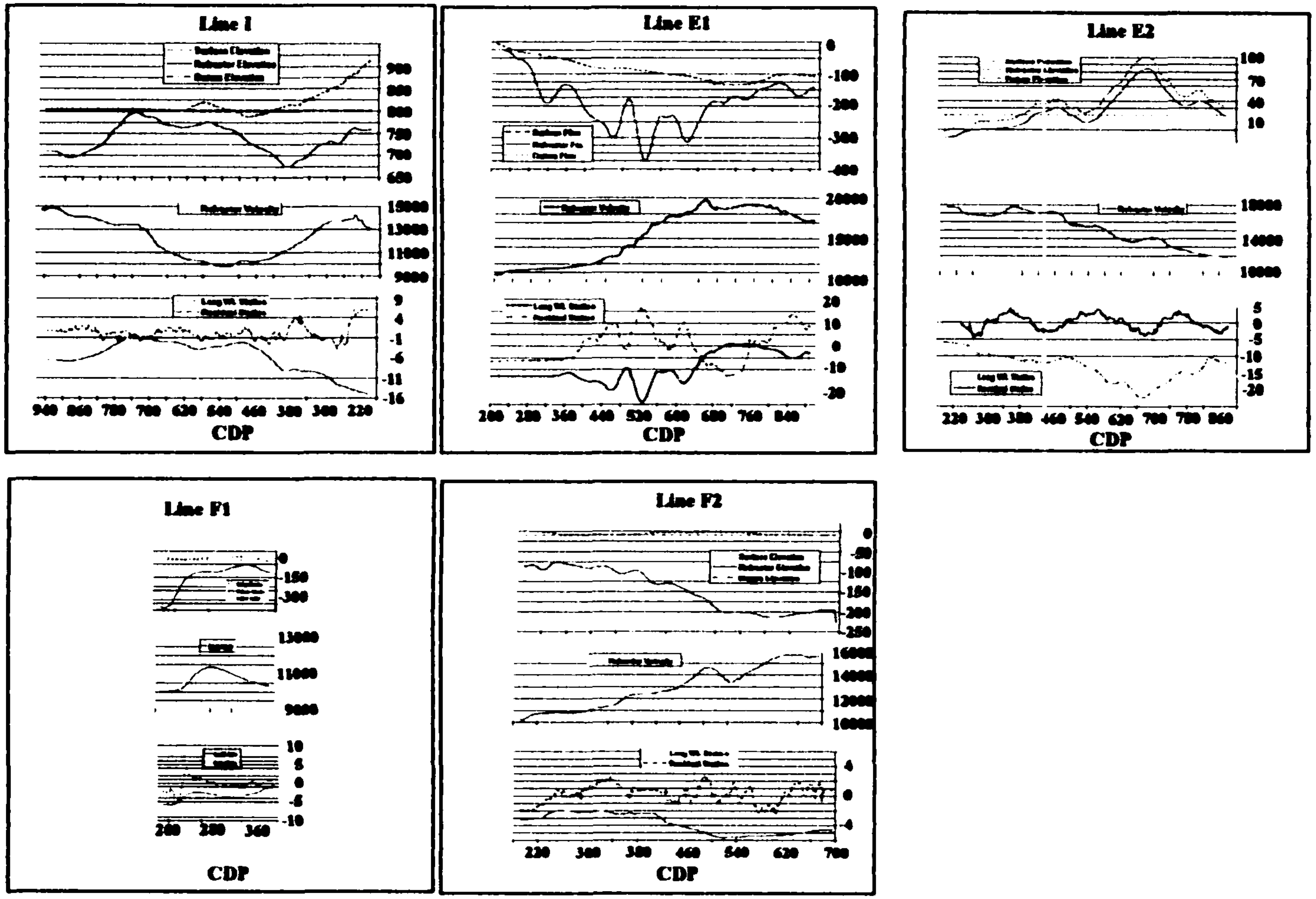

Figure 7 Refraction statics curves for Lines I, E1, E2, F1, F2. The surface elevation, the refractor elevation, and the datum elevation are shown in the top of each panel. The refractor velocities are shown in the middle of each panel. The long wavelength statics (red, slowly changing) and the short wavelength statics (blue, fast changing) are shown in the bottom of each panel. The north ends of all lines are to the right.

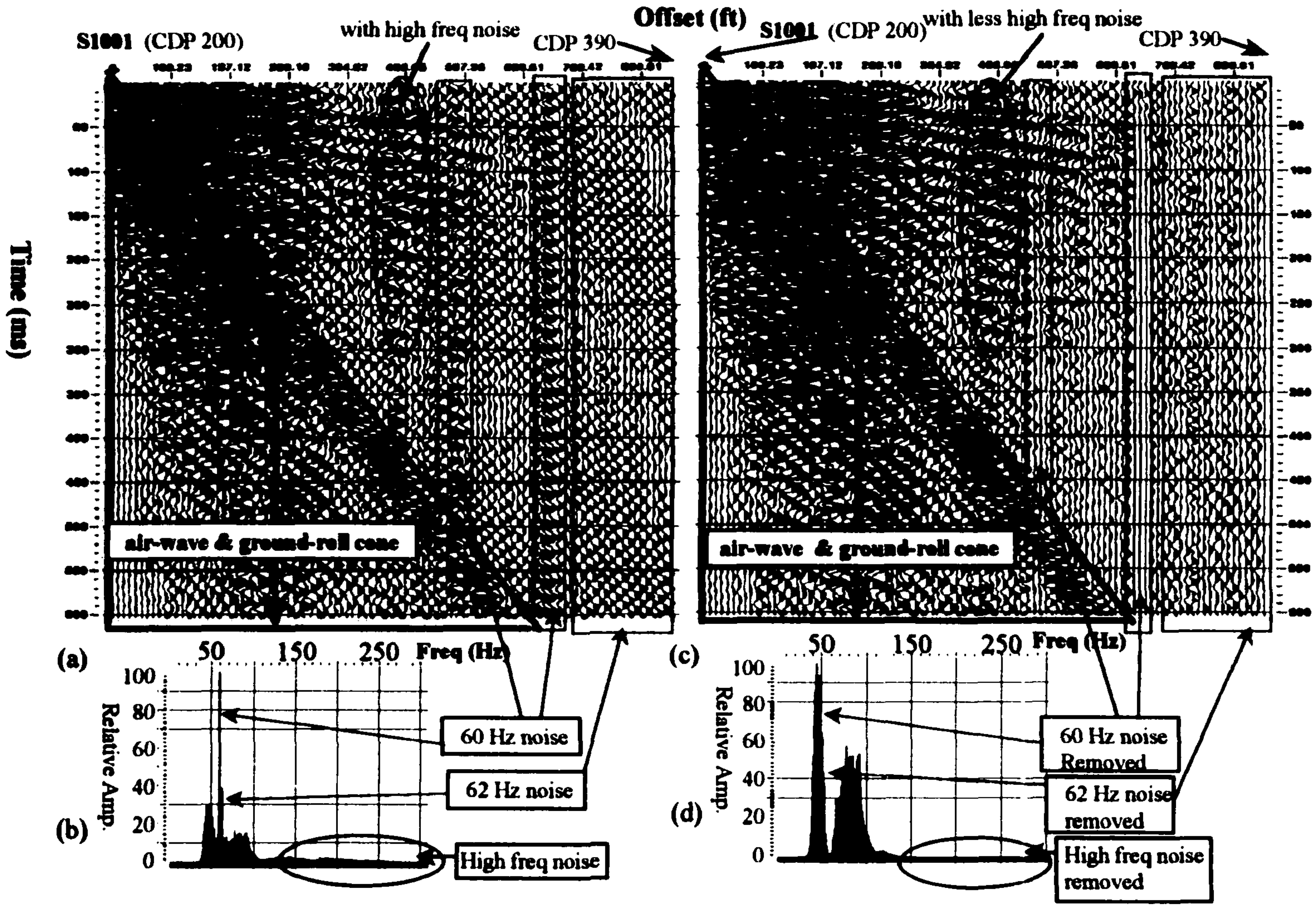

Figure 8 Shot 1001 (at CDP 200) before and after notch filtering and band pass filtering: (a) VSW correlated shot gather 1001; (b) Average power spectrum of (a); (c) Shot gather after filtering; (d) Average power spectrum of (c). 60 and 62 Hz noise has been greatly reduced. The high frequency noise has also been reduced.

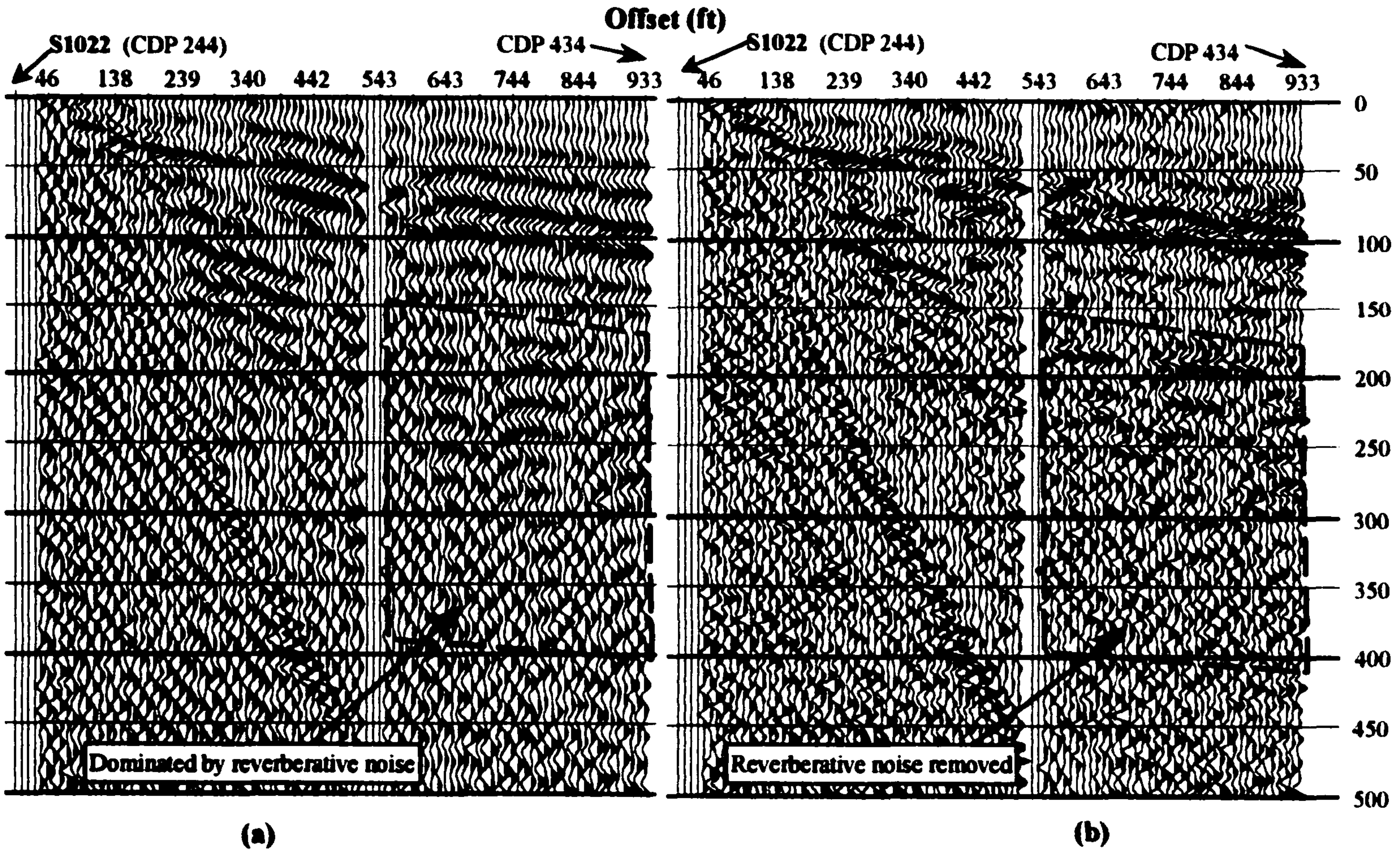

Figure 9 Shot gather 1022 (at CDP 244) before and after continuous spectral balancing: (a) VSW correlated shot gather after the notch and band-pass filtering. (b) Continuous spectral balancing of (a). The shot gather in (a) was dominated by reverberative noise. The continuous spectral balancing has greatly reduced the reverberative noise, and reflections stand out much clearer.

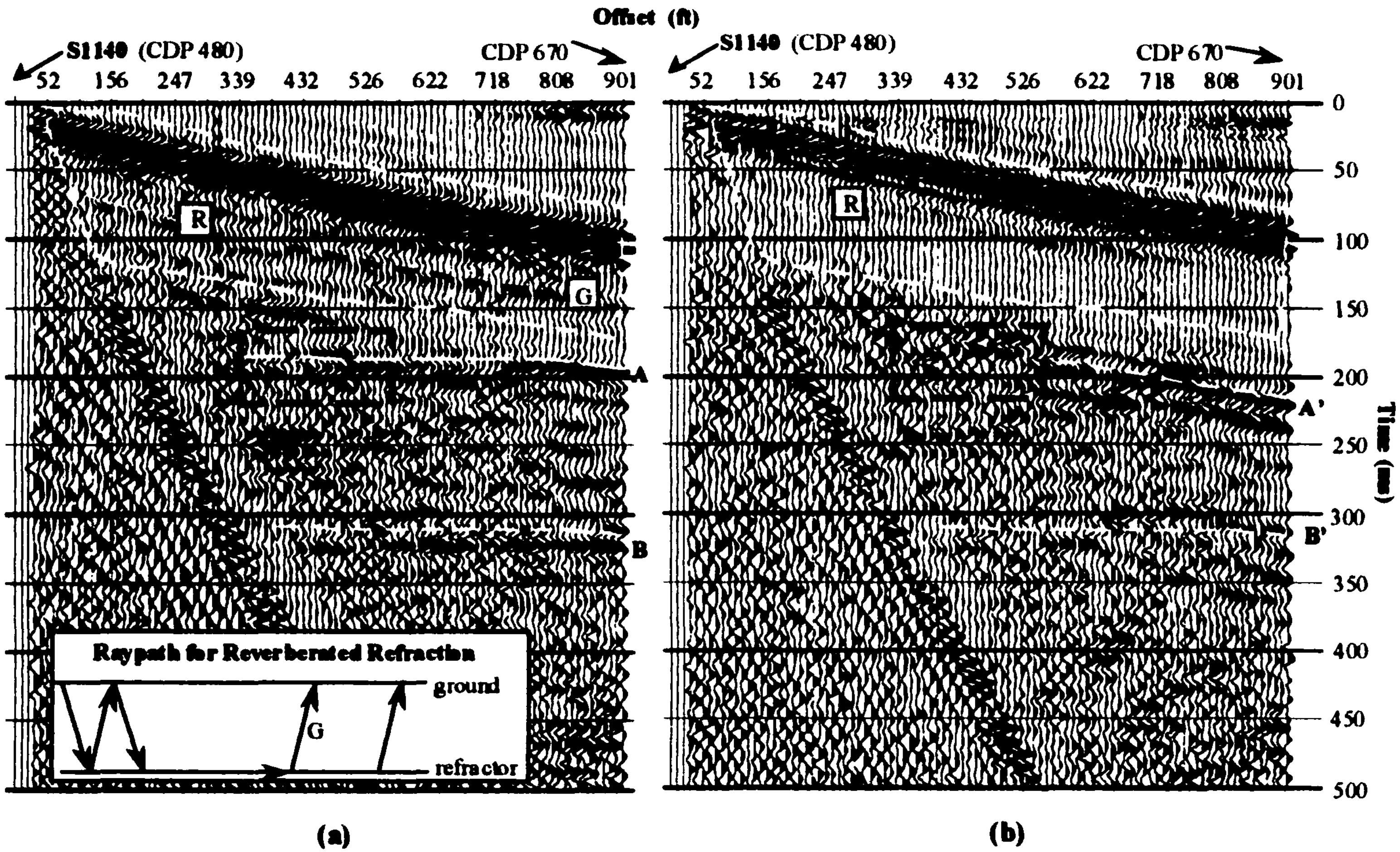

Figure 10 Shot gather 1140 (at CDP 480) before and after predictive deconvolution, using prediction lag of 12 ms, prediction operator length of 80 ms, and autocorrelation window starting from the first arrivals. (a) VSW correlated shot gather after the notch and band-pass filtering in Figure 8. Event G (inside yellow box) is parallel to the first arrivals. It is interpreted as reverberated refraction, with the ray path shown at the bottom. (b) Predictive deconvolution of (a). The reverberated refraction event (G inside the yellow box) has been removed. However, the possible reflection event (R) has also be greatly reduced. The strong reflection event A has 25 ms time delay in the far offsets (A') and becomes especially discontinuous inside the blue rectangular box. Strong reflection event B becomes almost unrecognizable (B').

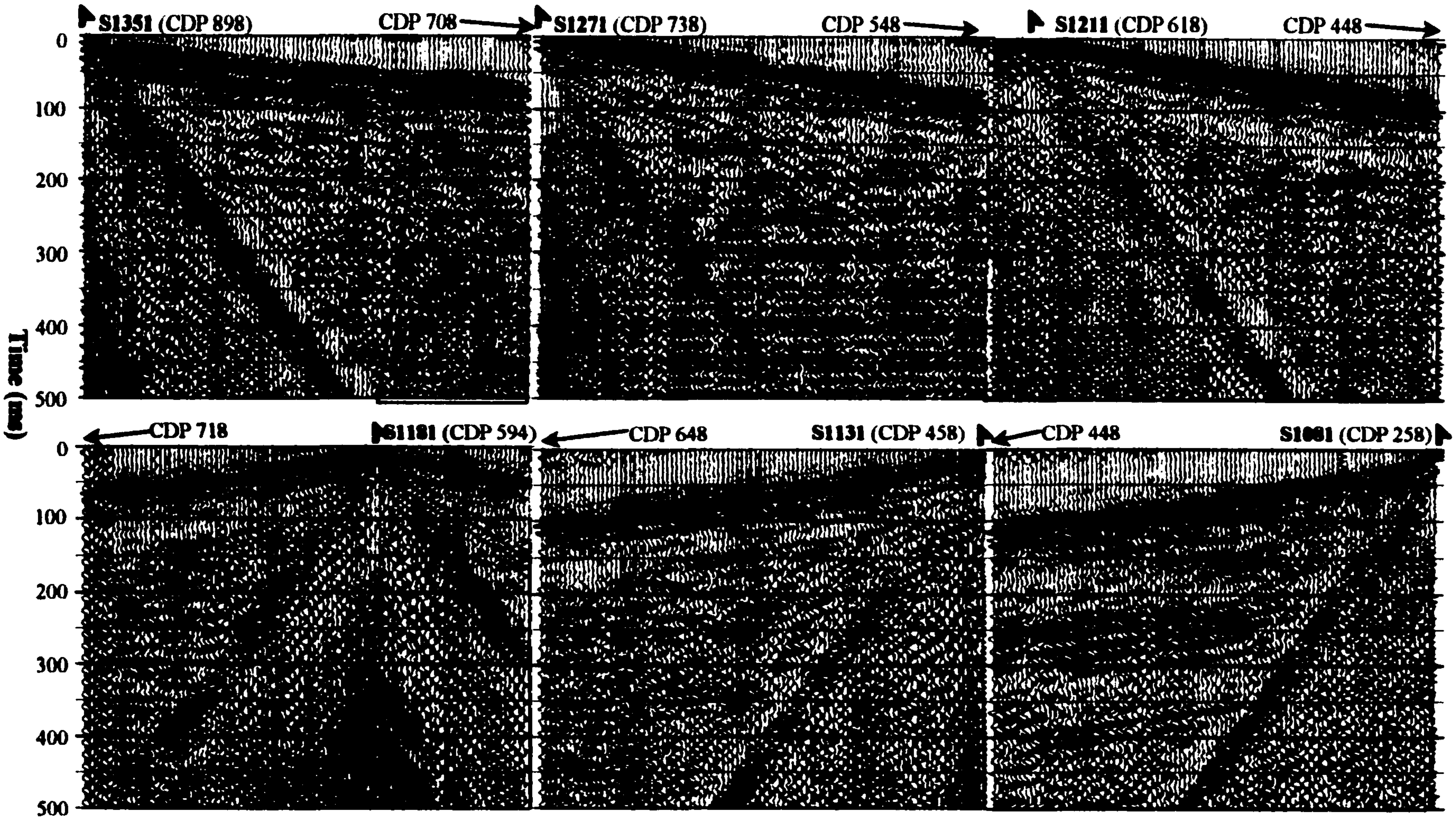

(A)

Figure 11A Shot gathers before notch and band-pass filtering, and continuous spectral balancing. The shot gathers were VSW correlated. Shot 1351 has some reverberative noise (inside the box in S1351). Shot 1271 is dominated by 60 Hz noise.

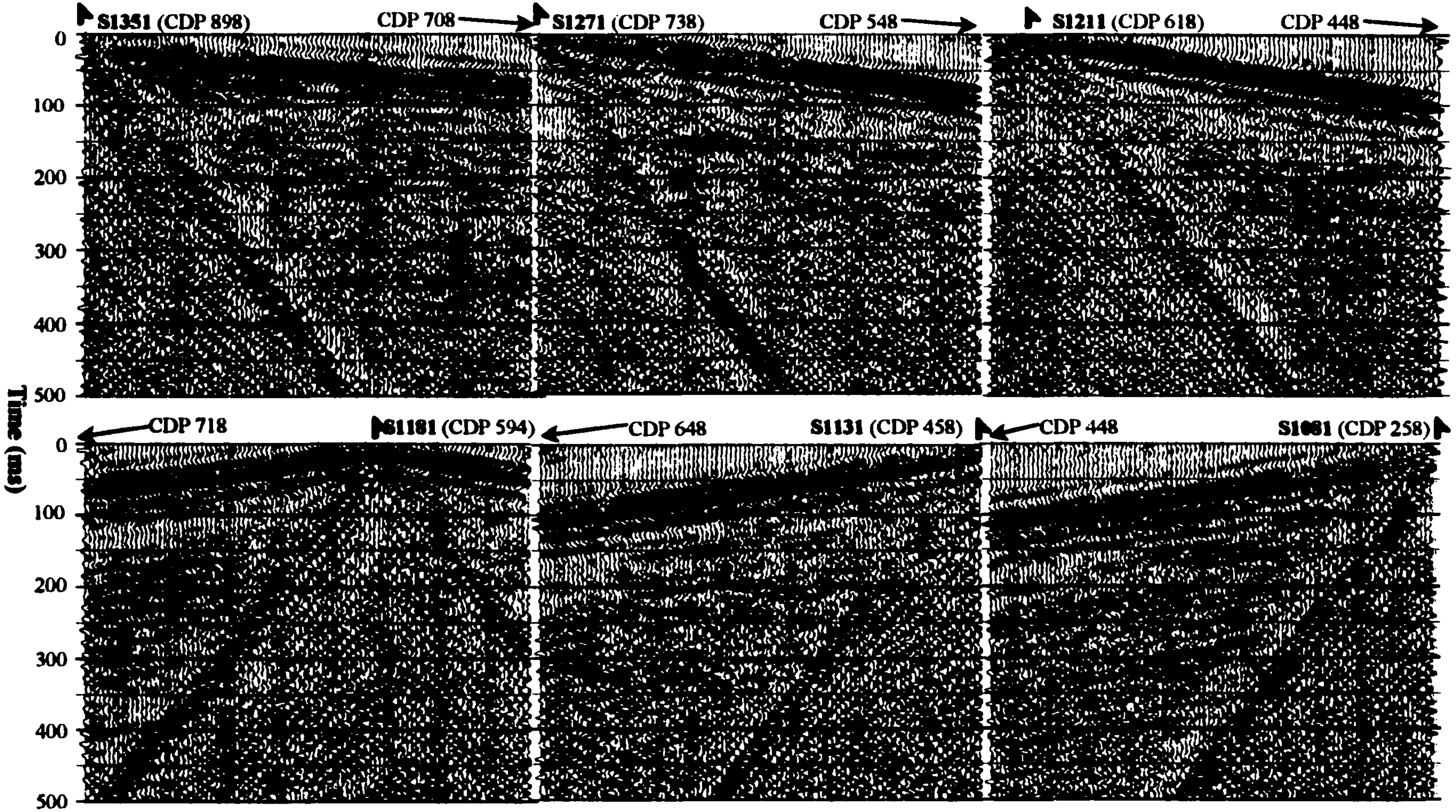

(B)

Figure 11B Shot gathers after notch and band-pass filtering, and continuous spectral balancing. The shot gathers were VSW correlated. Possible reflection events are marked (green and blue lines through peaks). The reflections are harder to recognize in Figure 11A. The green lines correspond to the two strong reflections (passing 140 ms and 190 ms at CDP 810) in the stacked sections (Figure 16D).

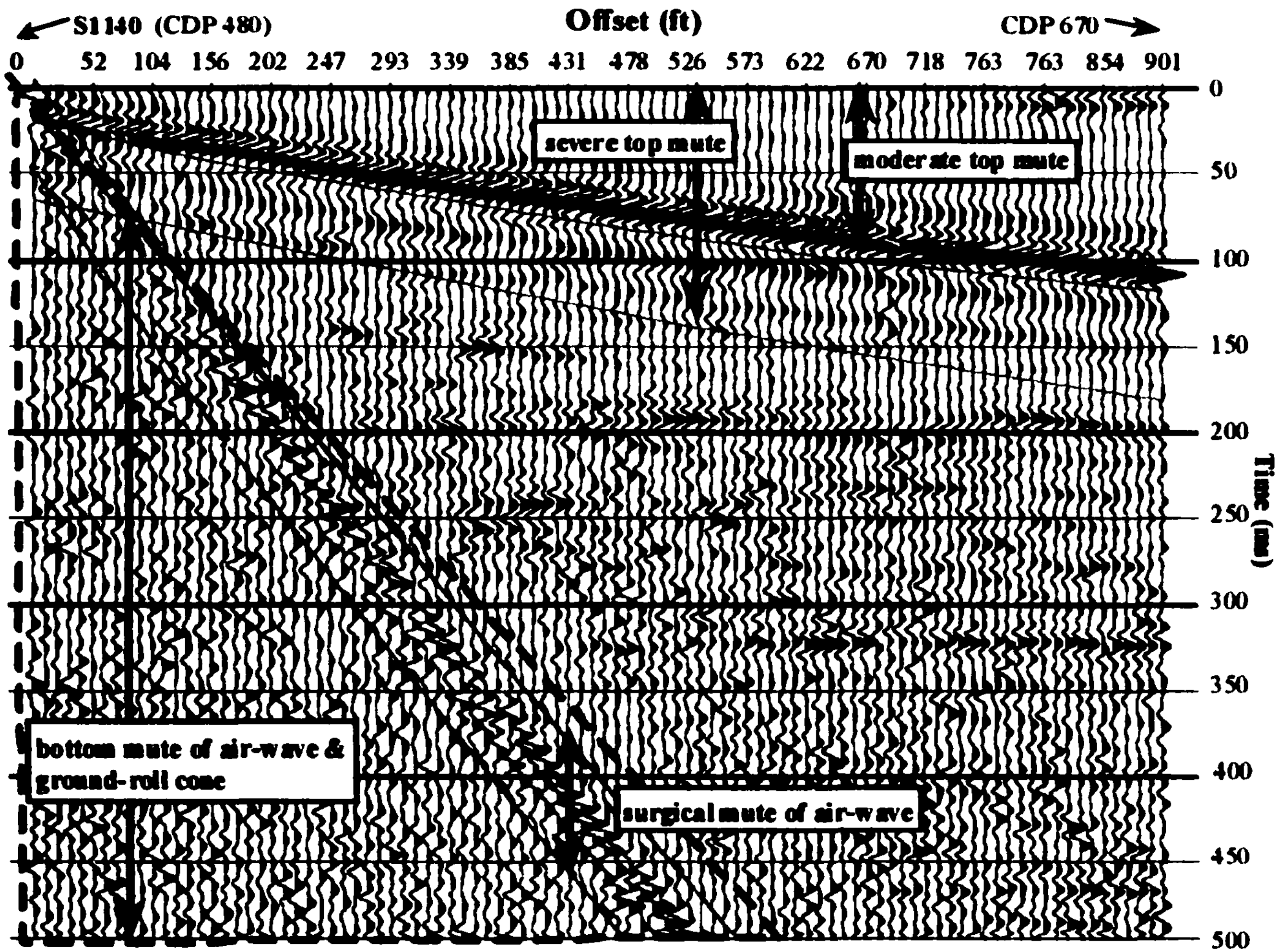

Figure 12 Definition of mute gates applied to shot gathers. Shown is shot no. 1140 (at CDP 480) after VSW, refraction statics, and continuous spectral balancing. The continuous spectral balancing has not improved much on the reflections inside the air-wave and ground-roll cone (Compare with Figure 10A). The events between green lines have nearly the same moveout as the first-arrivals and are interpreted to be reverberated-refractions.

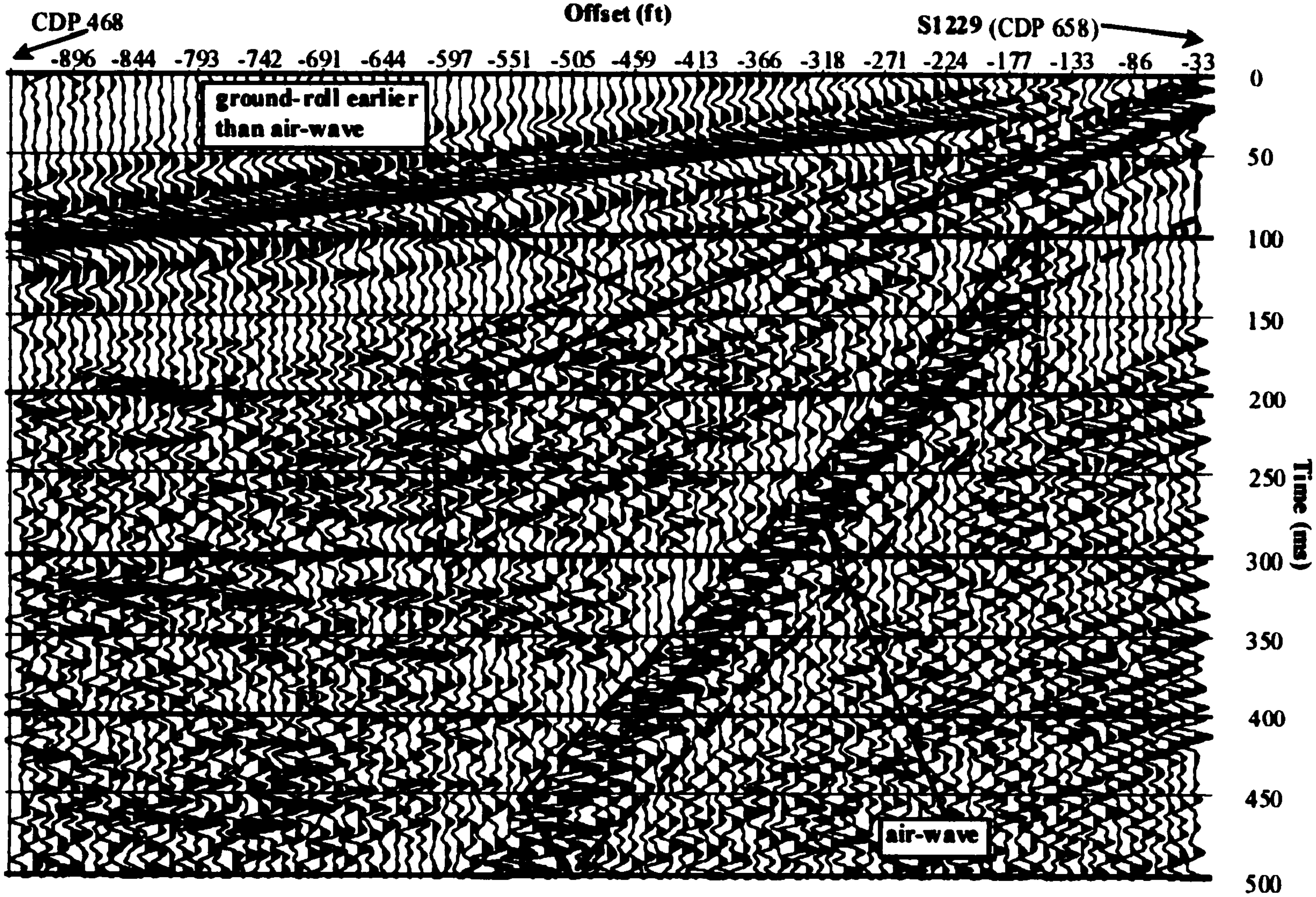

Figure 13 Example shot gather (1229) having ground-roll noise earlier than air-wave. Such ground-roll should not be muted because reflections are nearby, and they could be damaged due to the muting.

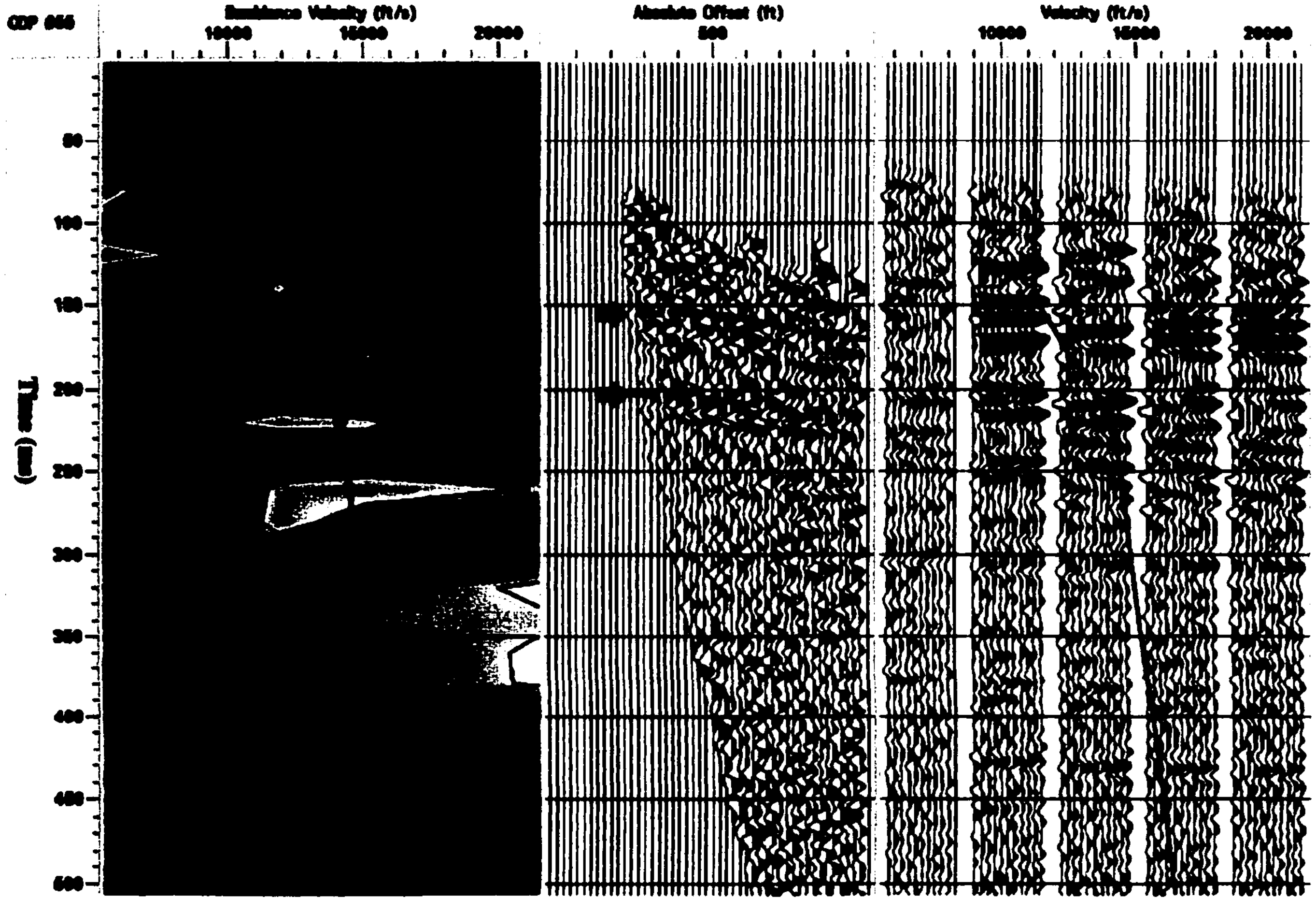

Figure 14 Example of stacking velocity analysis for Line I at CMP 655. There are not many bulls' eyes in the velocity spectra (left) due to the low signal-to-noise ratio in the super-gather (middle). It is necessary to depend on the constant-velocity-stacked traces (right) and the fitting of hyperbolas, which show up on top of the super-gather (middle) when the mouse cursor is placed on the velocity spectra. The arrows on the super-gather point to the reflection events that correspond to the two dots picked on the velocity spectra and on the constant-velocity-stacked traces. The two events are stacked into strong reflections at 160 ms and 220 ms respectively at CMP 655 of the stacked section (Figure 16D). The gaps on the right panel are for display purpose only.

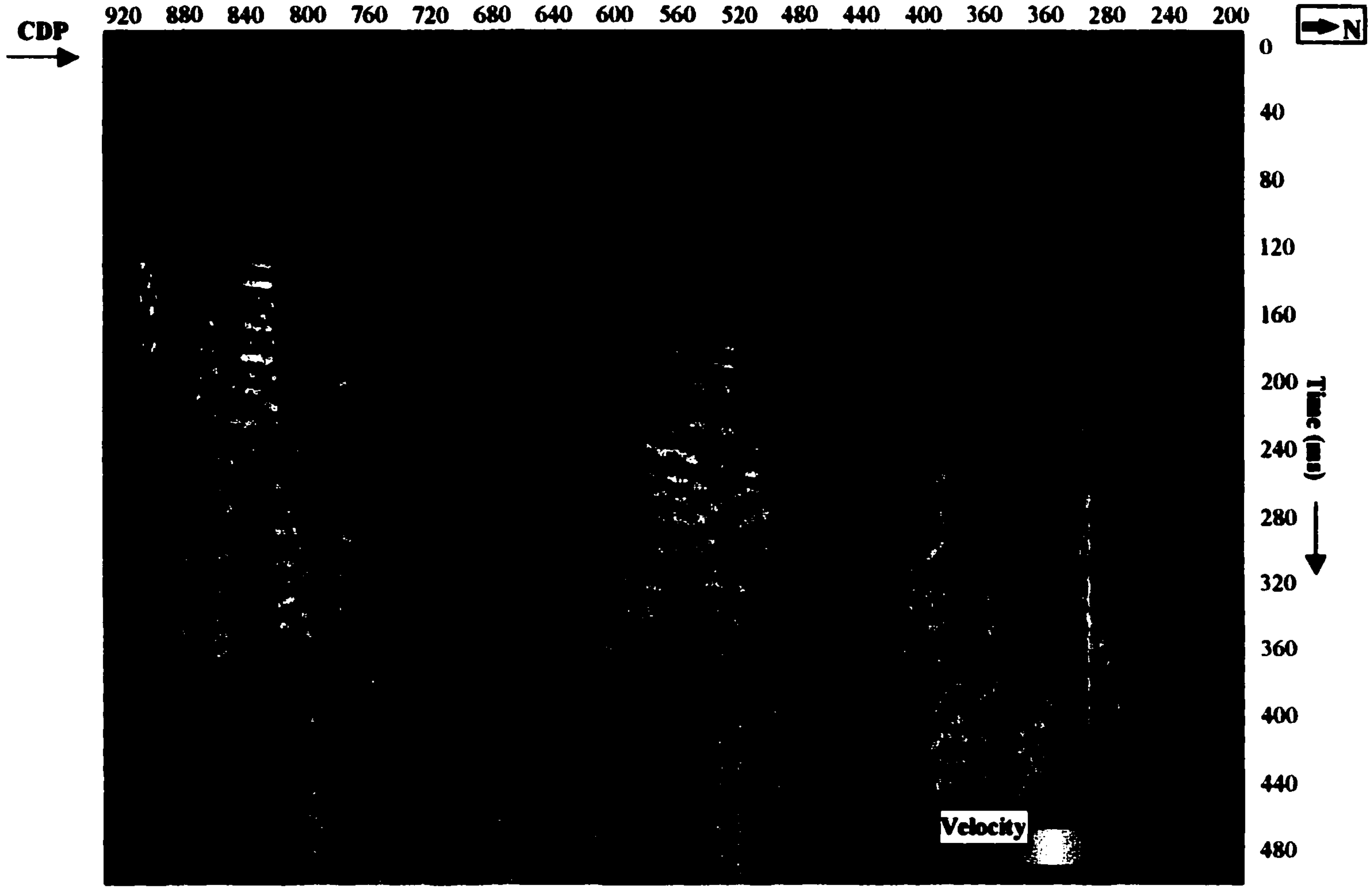

Figure 15 Stacking velocity field, analyzed at every 20th CMP and then interpolated. Stacked section is displayed as overlay in the background. Because the structures are complex and stacking velocities are dip dependent, there is no easy and accurate way of relating the stacked velocities to structures and/or lithologies. Because a velocity difference of 1000-3000 ft/s makes little difference in the stacked section, no attempt is made to smooth the velocity field for NMO correction. The general increase in velocity with depth is due to the increase in compaction and the decrease in weathering.

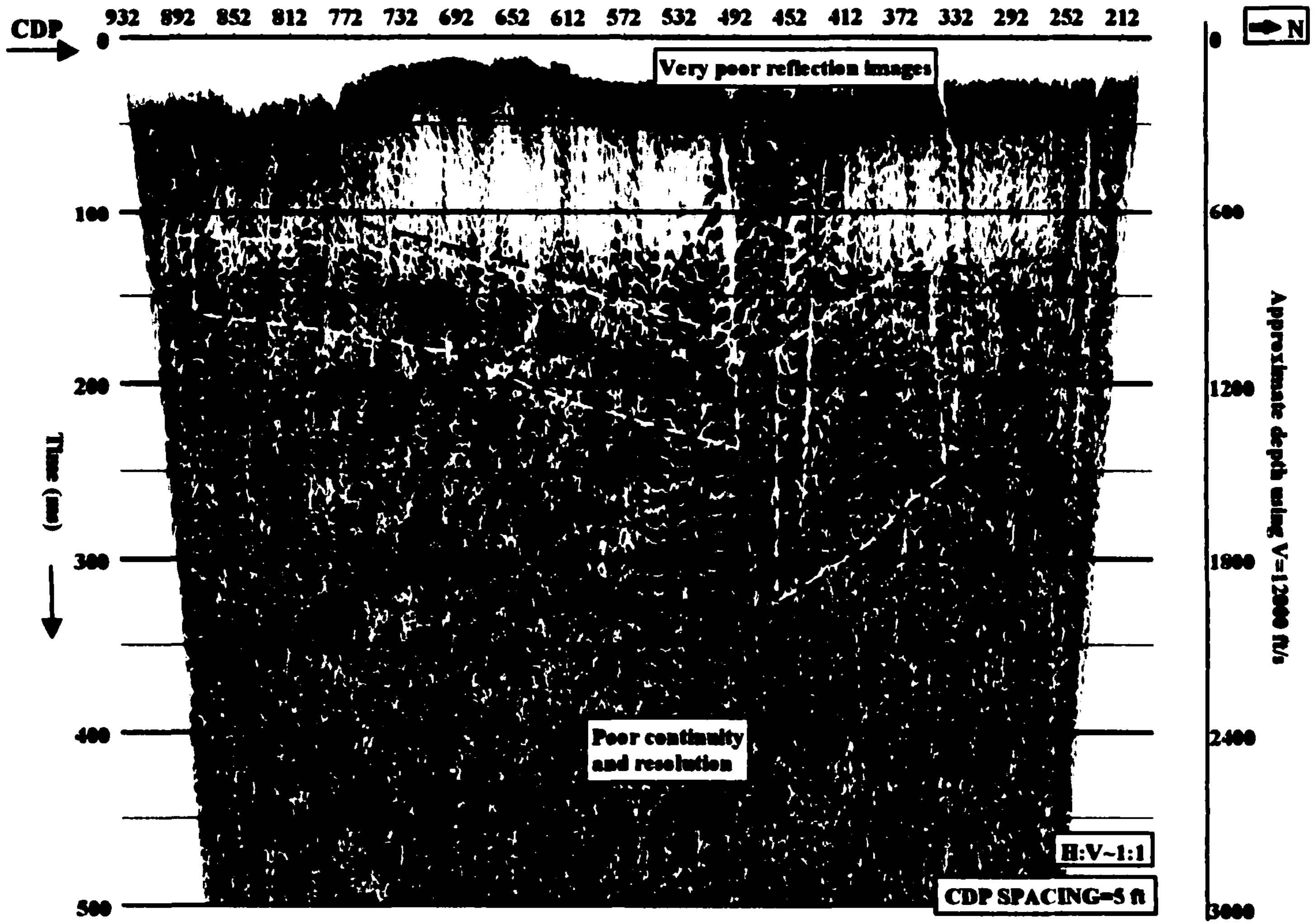

Figure 16A Stacked section with conventional correlation instead of Vibroseis whitening. Refraction statics is included, but not continuous spectral balancing. The continuity and resolution are poor inside the two yellow boxes, as compared with Figure 16B. There are almost no reflections inside the two green boxes. Because the conventional correlation does not compensate the frequency components attenuated in the wave propagation process, we cannot expect it to produce reflection events in comparable quality of amplitude and continuity as the Vibroseis whitening.

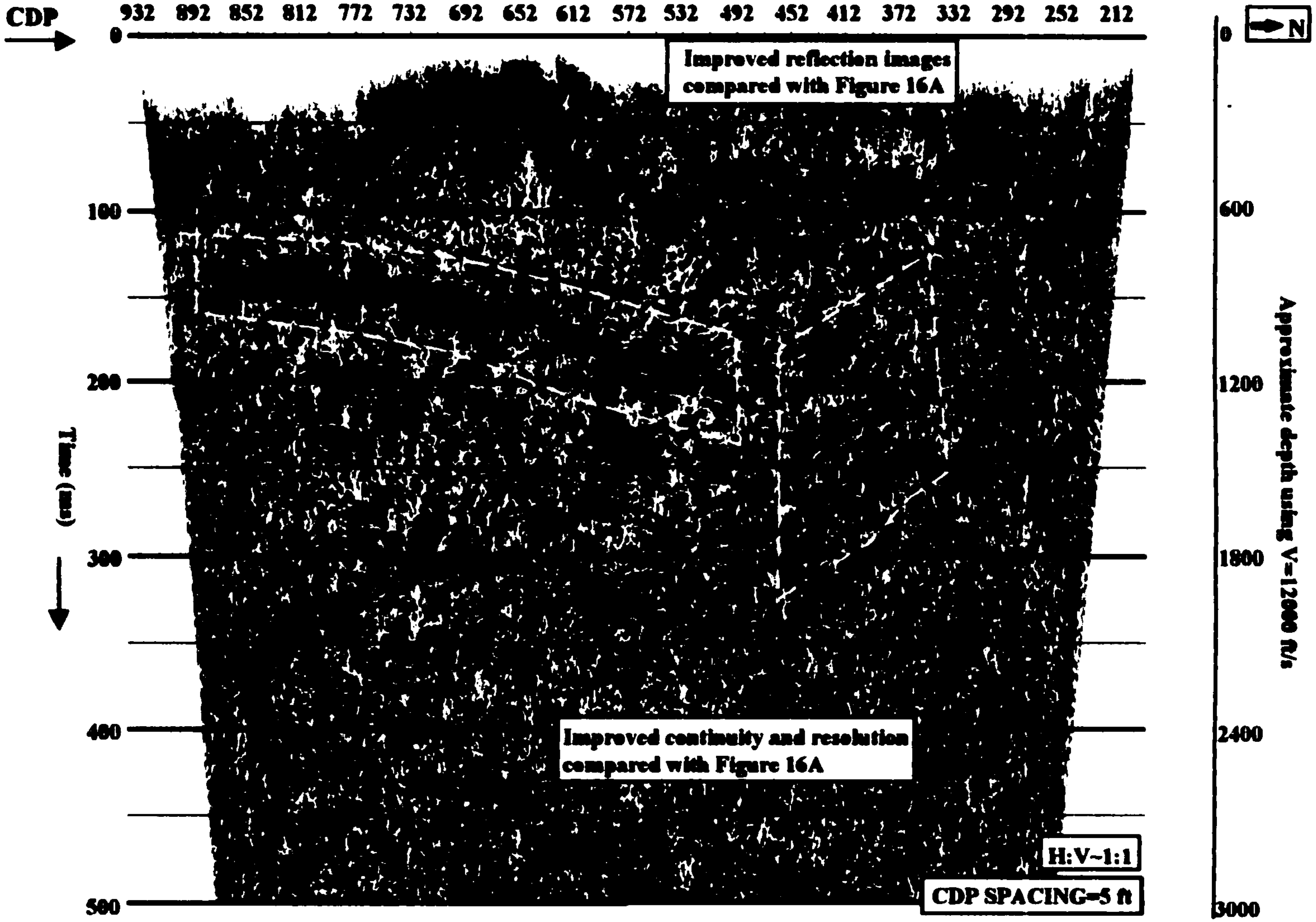

Figure 16B Stacked section with Vibroseis whitening and refraction statics. Continuous spectral balancing is not included. The reflection images, the continuity and the resolution are improved (yellow boxes) compared with Figure 16A.

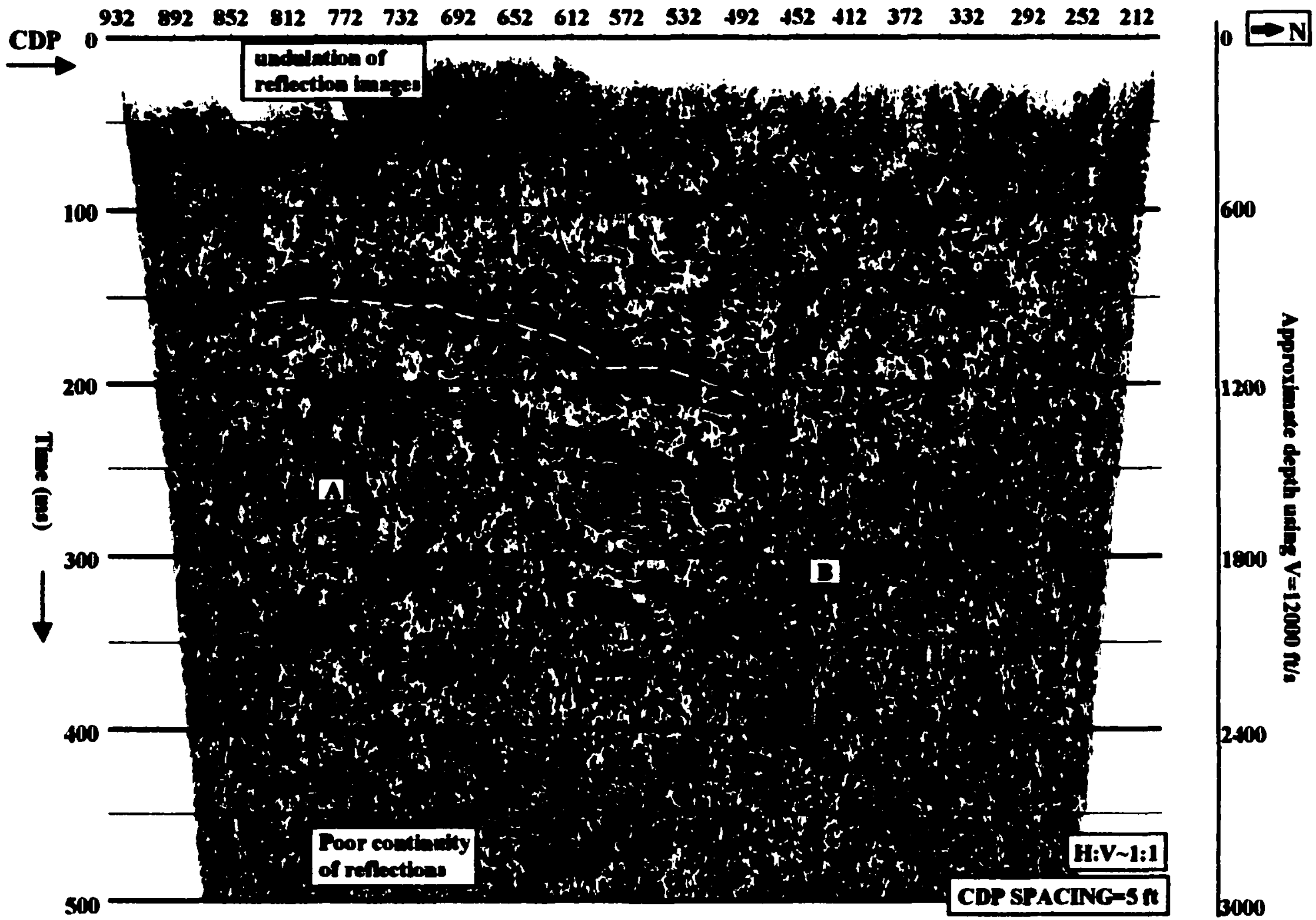

Figure 16C Stacked section with no refraction statics, but with VSW. Continuous spectral balancing is not included. The undulation of reflection images (yellow line) is caused by long wavelength statics problems. The reflection images inside the two green boxes are poorer in continuity and resolution than in Figure 16B due to short wavelength statics problems.

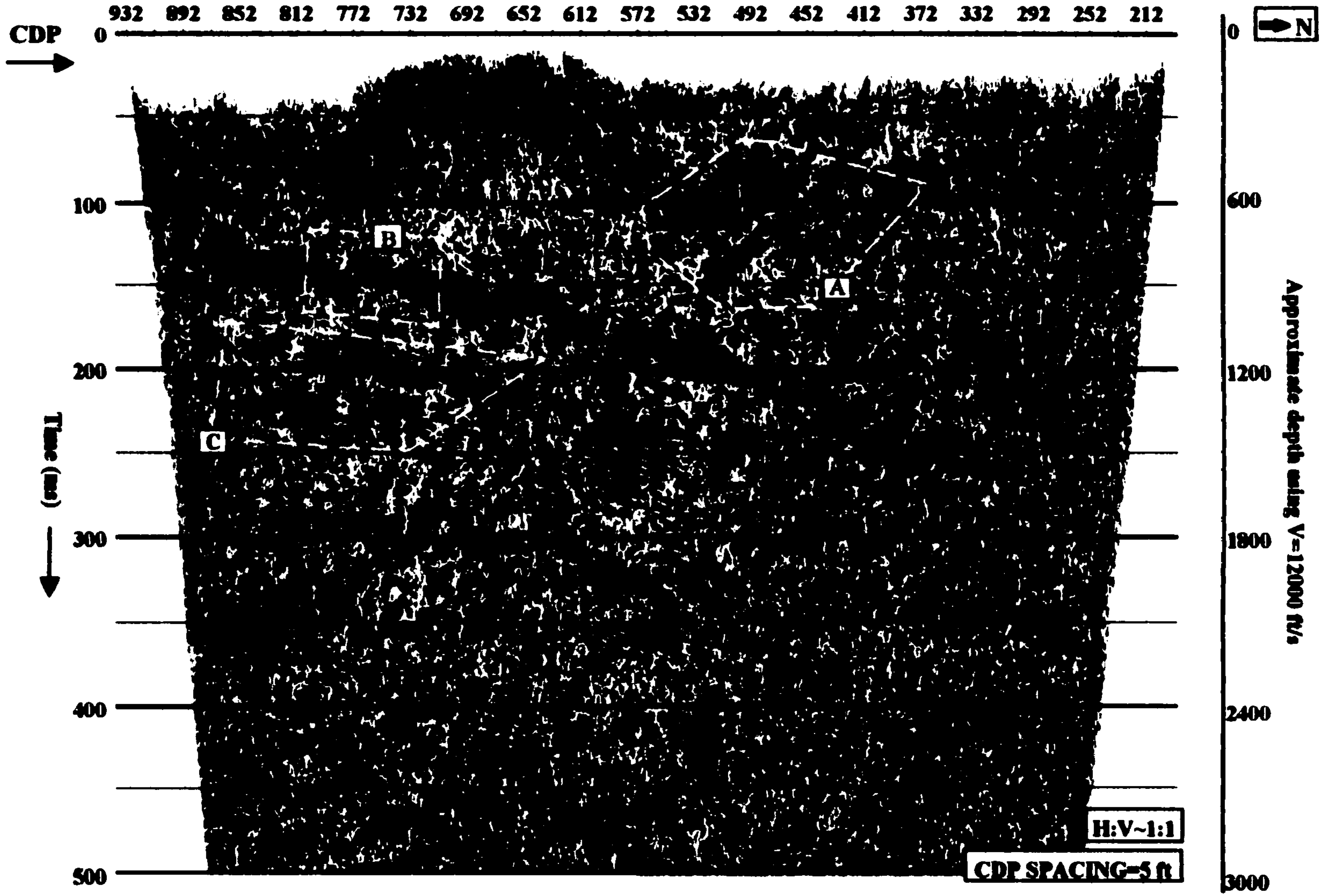

Figure 16D Stacked section with continuous spectral balancing. VSW and refraction statics are included. Compared with Figure 16B, it has an overall higher resolution, less north-dipping noise inside box A, better continuity of reflection images inside boxes B and C.

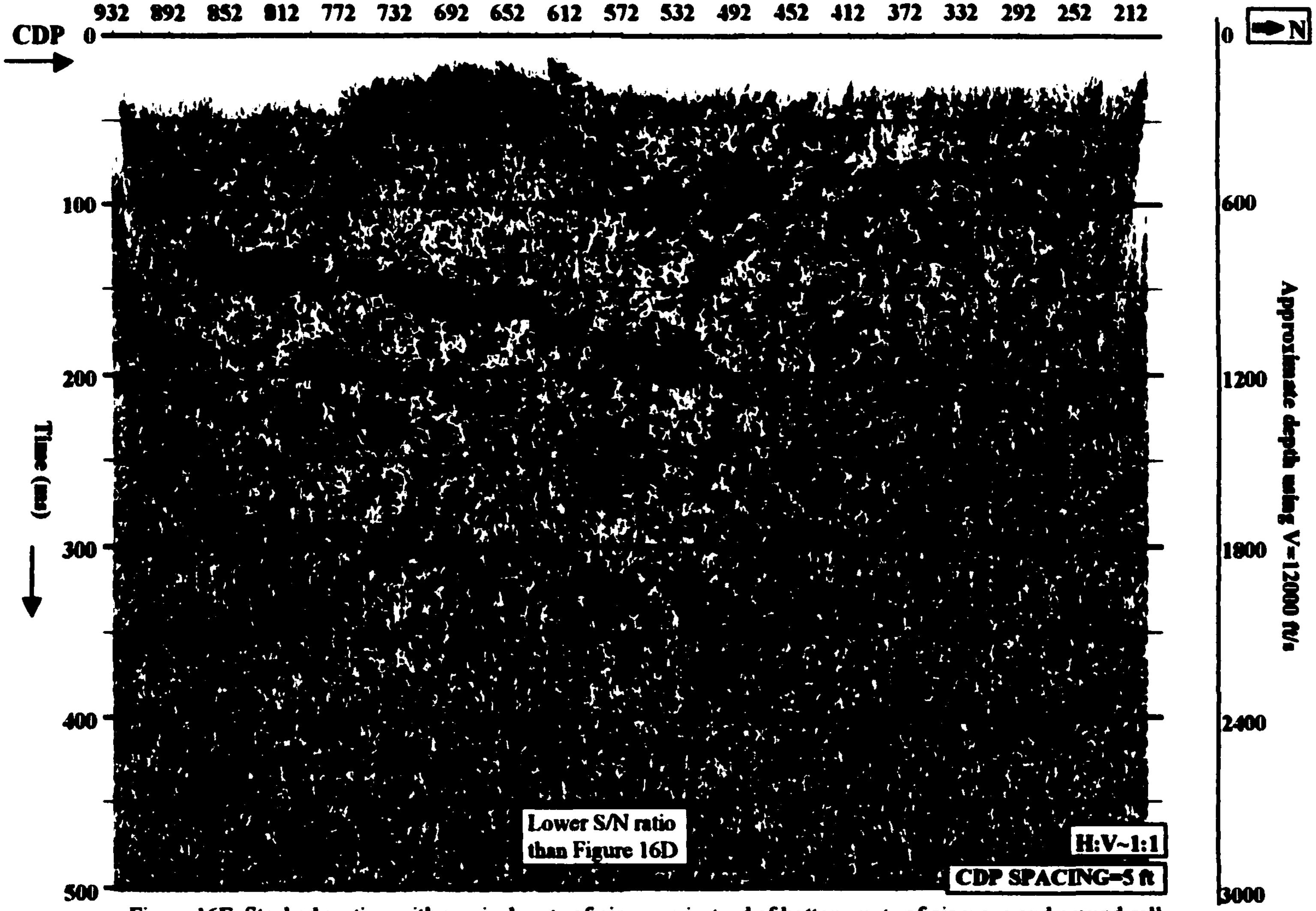

Figure 16E Stacked section with surgical mute of air-wave instead of bottom mute of air-wave and ground-roll. VSW, refraction statics, and continuous spectral balancing are included. Lower S/N ratio results, especially on the northern part inside the polygon, compared with Figure 16D.

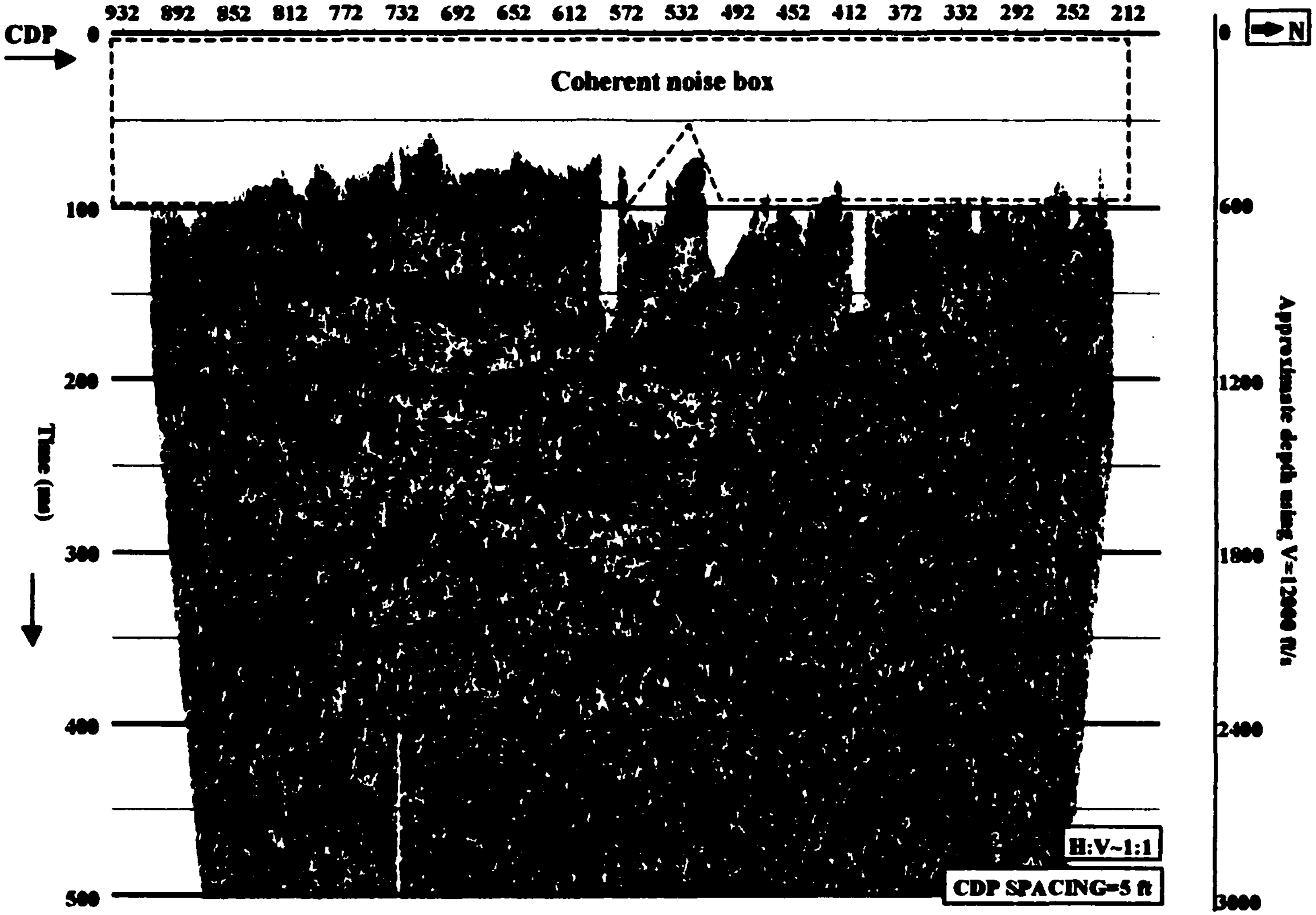

Figure 16F Stacked section with severe top mute instead of moderate top mute. VSW, refraction statics, and continuous spectral balancing are included. The deeper part of this figure is the same as Figure 16D. Because the severe top mute almost zeroed out the first 100 ms in the stacked section (Figure 16F), whereas the moderate top mute did not zero out the first 100 ms in the stacked sections (Figure 16A--E), the first 100 ms is considered to be coherent noise box, since the moderate top mute has kept most of the parallel events in the shot gathers (i.e., reverberated refractions, Figure 10).

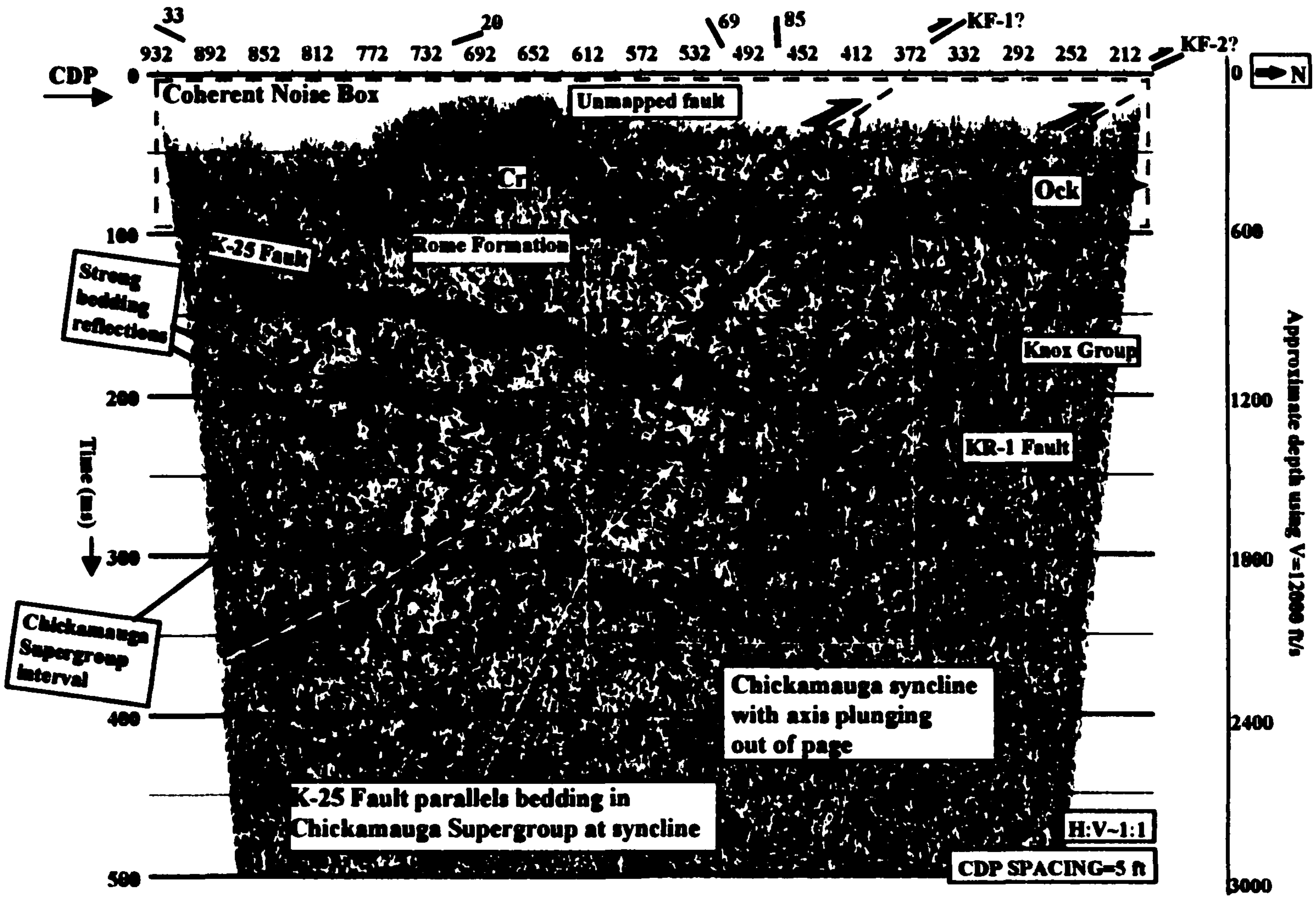

Figure 17 Geological interpretation (based on discussions with Lemiszki). At the top are bars showing approximate dips projected into the section. Numbers give true dips (directions shown in Figure 5) of surface rocks. Approximate dips of mapped faults are also shown. Major features interpreted: K-25 Fault; Chickamauga bedding reflections; Chickamauga syncline; KR-1 reverse fault; minor faults cutting the Chickamauga Supergroup. Yellow dashed line below 200 ms on the south end shows an event to be explained later in depth migration.

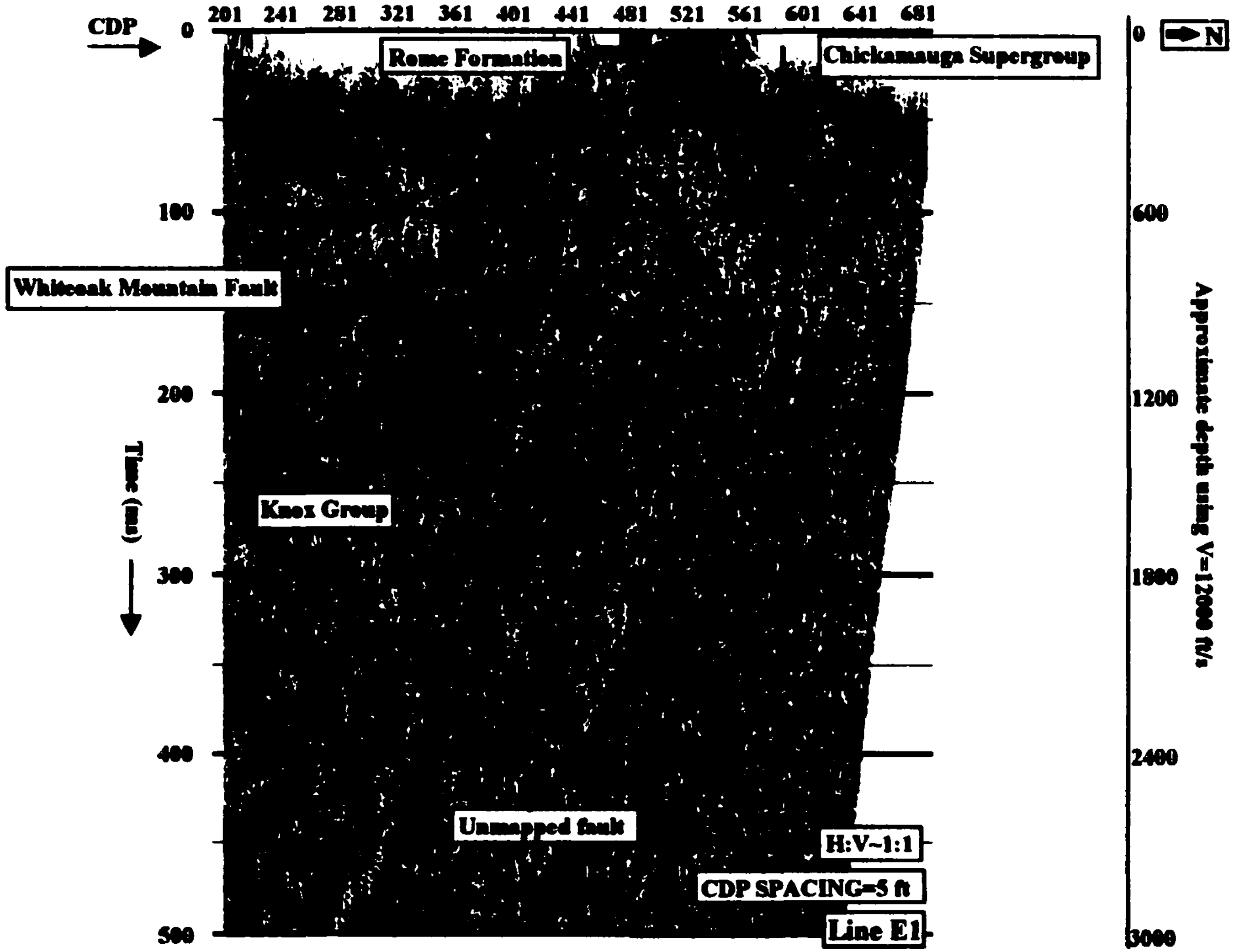

Figure 18A Seismic section and geological interpretation of Line E1. On the surface, Line E1 crosses the Whiteoak Mountain Fault at approximately CDP 600 (Figure 5). Major features interpreted: Whiteoak Mountain Fault; Unmapped fault.

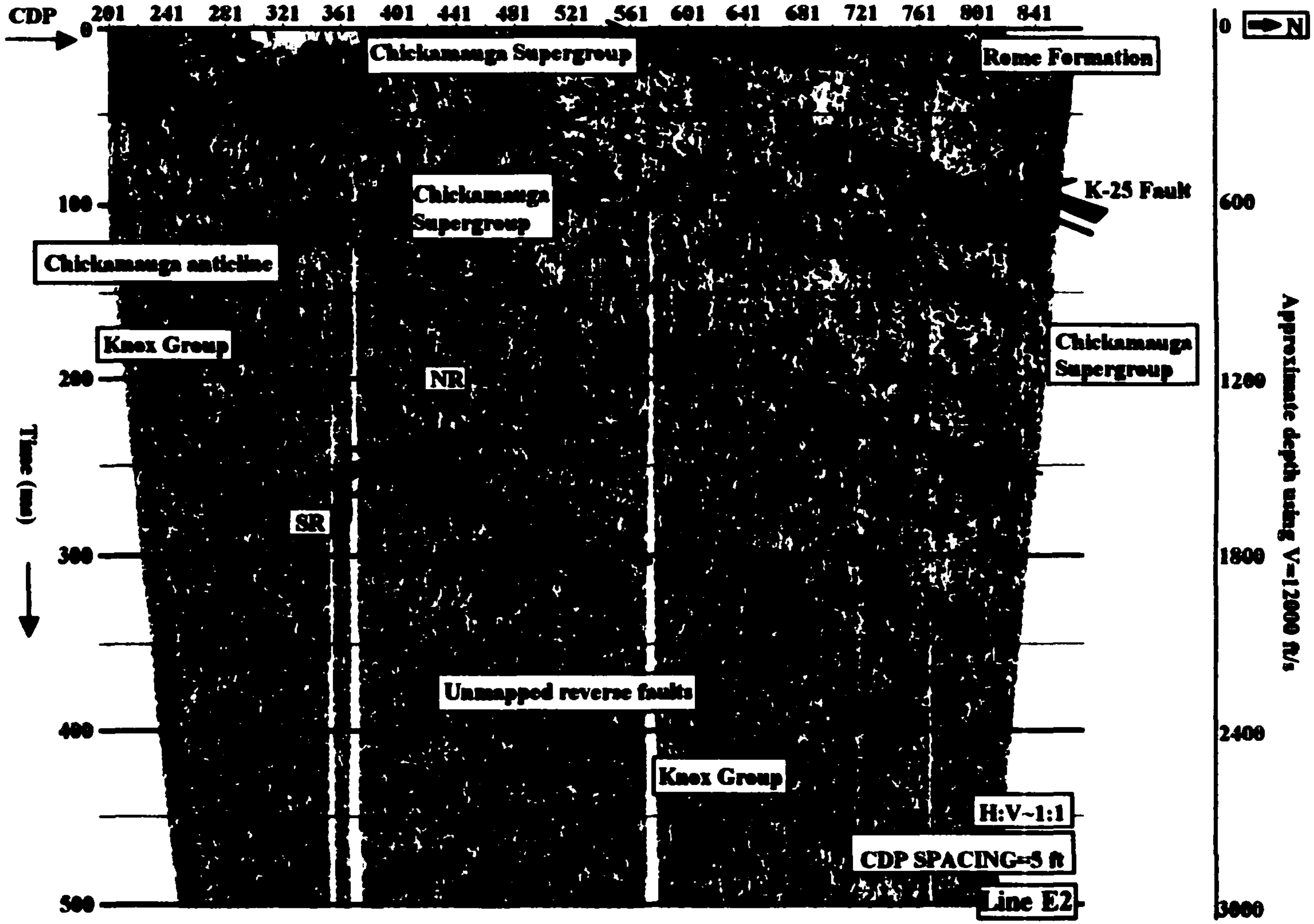

Figure 18B Seismic section and geological interpretation of Line E2. On the surface, Line E2 crosses the K25 at approximately CDP 540 (Figure 5). Major features interpreted: Chickamauga anticline; K-25 Fault; Unmapped faults; Chickamauga Supergroup reflections.

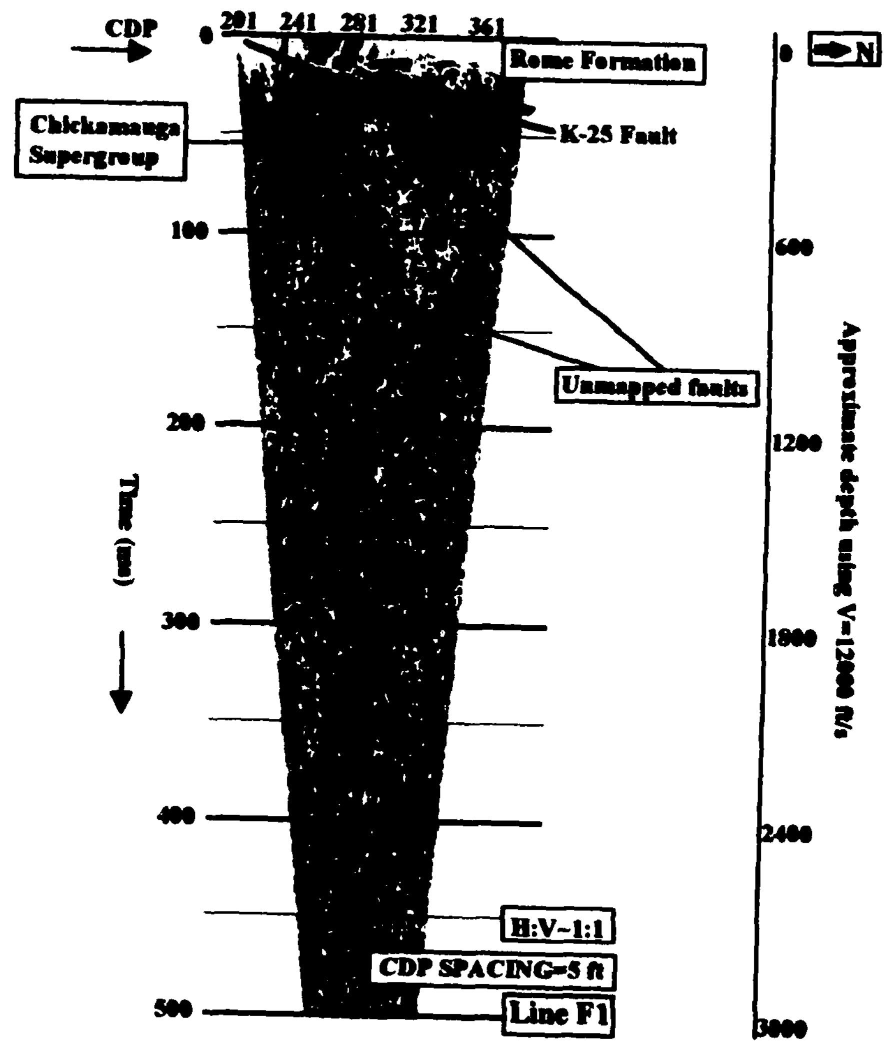

Figure 18C Seismic section and geological interpretation of Line F11. On the surface, Line F1 crosses the K-25 Fault at approximately CDP 230 (Figure 5). Major features interpreted: K-25 Fault; unmapped faults; Chickamauga Supergroup reflections.

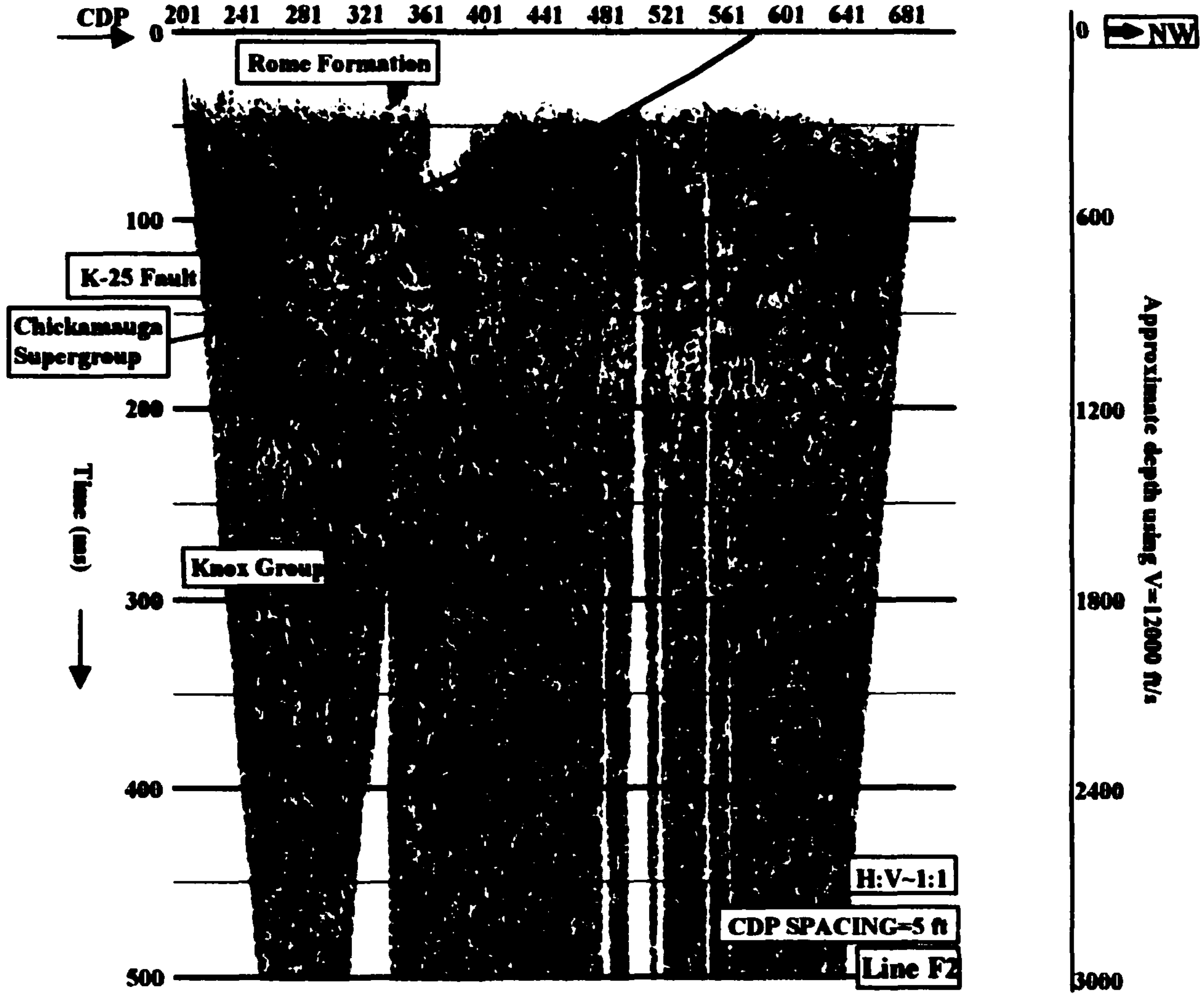

Figure 18D Seismic section and geological interpretation of Line F2. On the surface, Line F2 crosses the K-25 Fault at approximately CDP 600 (Figure 5). Major features interpreted: K-25 Fault; Chickamauga Supergroup reflections; minor unmapped faults.

Formation /Group	Age	Sample	Sample Number	*Pressure (Atm)* *200* *Equivalent Depth (ft)* *1968*	*400* *3937*	*600* *5905*	Average Density (g/cm^3)	Acoustic Impedance (g/cm^2 sec)
				Velocity (ft/sec)				
Knox Group	Ordovician	Upper Knox Dolomite	1-2A	**20,177**	20,734	20,997	2.82±0.00	$1.71x10^6$ – $1.80 x 10^6$
			1-2B	**19,947**	20,538	20,702		
		Kingsport Dolomite	4-11A	**19,192**	19,750	20,341	2.79±0.00	$1.64x10^6$ – $1.81x10^6$
			4-11B	**20,833**	21,128	20,292		
		Longview Limestone	4-10A	**20,964**	21,686	21,719	2.71±0.00	$1.79x10^6$
		Chepultepec Limestone	4-5A	**21,161**	21,489	21,522	2.72±0.00	$1.73x10^6$ – $1.78x10^6$
			4-5B	**20,958**	21,128	21,161		
	Cambrian	Chepultepec Dolomite	4-6A	**21,161**	21,489	21,522	2.83±0.00	$1.73x10^6$ – $1.88x10^6$
			4-6B	**20,932**	21,128	21,161		
		Copper Ridge Sandstone	4-7A	**17,946**	18,471	18,996	2.71±0.00	$1.48 x 10^6$ – $1.63x10^6$
			4-7B	**18,602**	19,324	19,718		
		Copper Ridge Dolomite	4-8A	**19,816**	20,111	20,734	1.8±0.01	$1.71x10^6$ –$1.78x10^6$
			4-8B	**19,947**	20,374	20,768		
Rome Formation		Rome Shale	5A1	**11,155**	12,139	13,451	2.67±0.02	$0.88x10^6$ – $1.09x10^6$
			5A2	**10,826**	12,139	12,467		
		Rome Dolomite	5B1	**24,278**	24,278	23,950	2.83±0.00	$2.06x10^6$ – $2.09x10^6$
			5B2	**24,278**	24,278	24,278		

Figure 19 Representative laboratory ultrasonic velocity measurements, densities, and acoustic impedance for rock samples at Price Mountain, Montgomery, Virginia (modified from Kolich, 1974). The ultrasonic velocities were measured under hydraulic pressures in laboratory to simulate conditions at burial depths (200 atm ~ 1968 ft). The first column of the velocity values (bold) will be relevant for the depth of interest at K-25. Only the Rome Formation and the Knox Group rock samples were included because there was no sample from the Chickamauga Supergroup. It can be seen that lithology is the most important factor controlling the range of velocities.

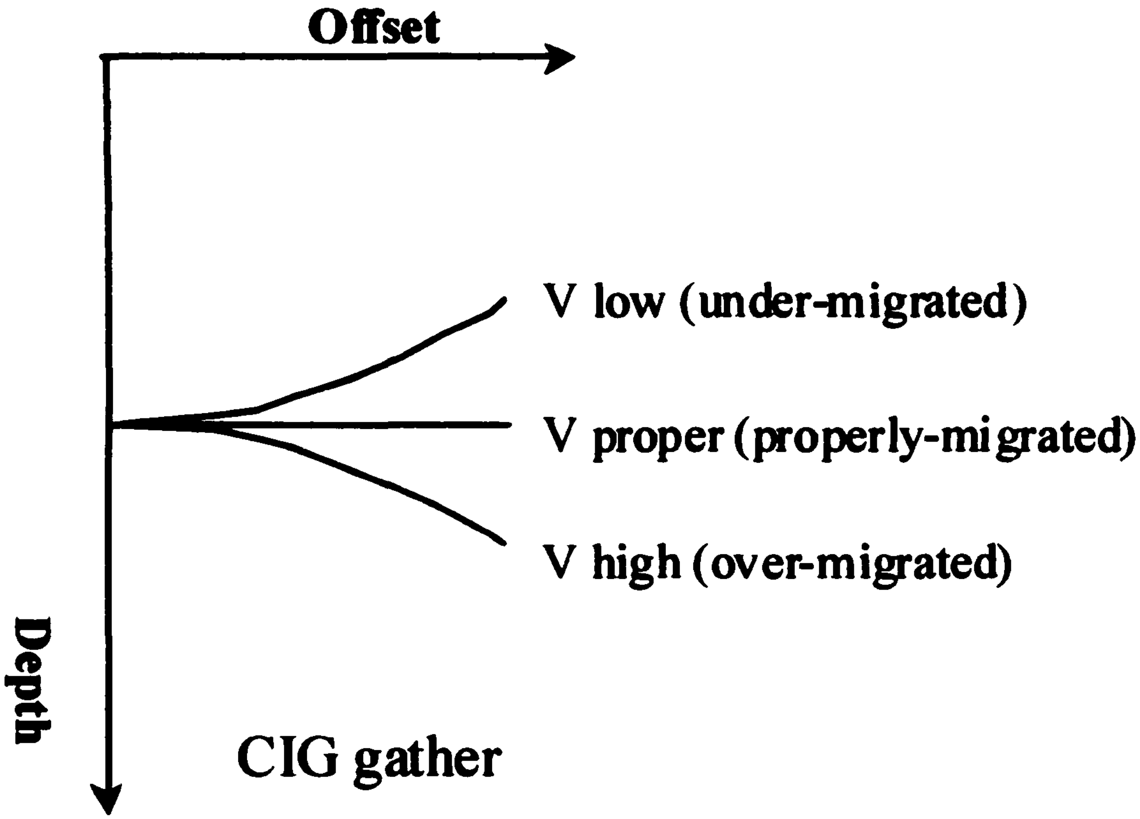

Figure 20 A schematic diagram for the alignment pattern of a reflection event in a common image gather (CIG) in response to the accuracy of migration velocity in prestack depth migration.
A proper velocity makes the reflection event aligned flat for all offsets (properly-migrated).
A low velocity makes the reflection event tailed-up toward increasing offsets (under-migrated).
A high velocity makes the reflection event tailed-down toward increasing offsets (over-migrated).

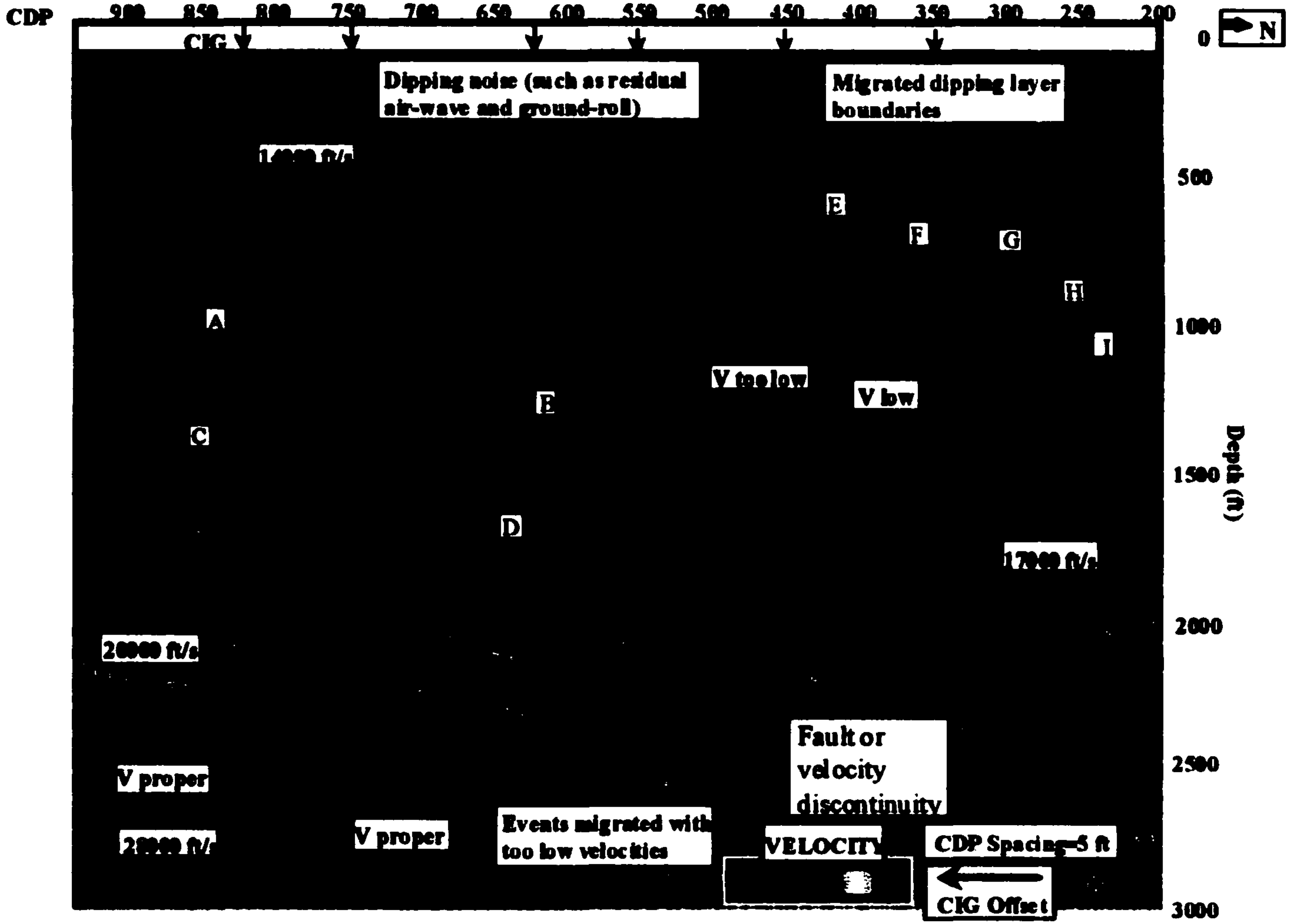

Figure 21A First velocity–depth model for Kirchhoff prestack depth migration of Line I. Every 10th CIG is displayed as overlay in variable density mode on top of velocity model. Green ellipses with letters indicate migrated reflection events corresponding to Figure 21B and Figure 21C. The black ellipse indicates a fault or velocity discontinuity. Polygonal areas with red lines indicate noise interference. Other polygonal areas indicate proper migration (V proper) and under-migration (V low). Arrows at the top of the figure indicate the CDP locations for detailed CIG gather displays (Figure 21C).

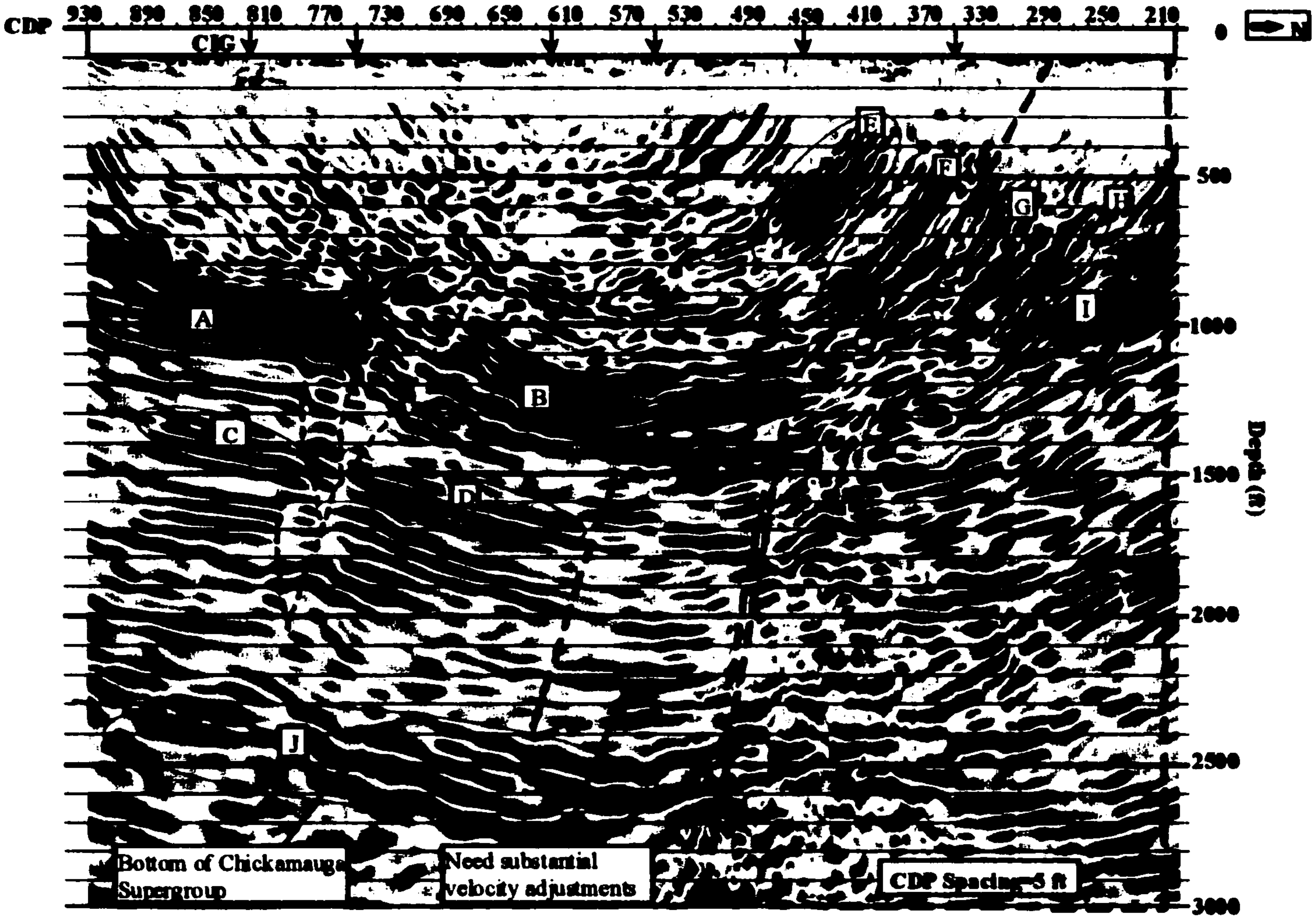

Figure 21B Prestack depth migrated section of Line 1 using first velocity model. Arrows at the top of the figure indicate the locations for detailed CIG gather displays (Figure 21C). Green ellipses with letters indicate migrated reflection events corresponding to Figure 21A and Figure 21C. Green dashed lines represent the interpretation of reflection events. The thin black dashed lines indicate a possible fault zone imaged by the depth migration.

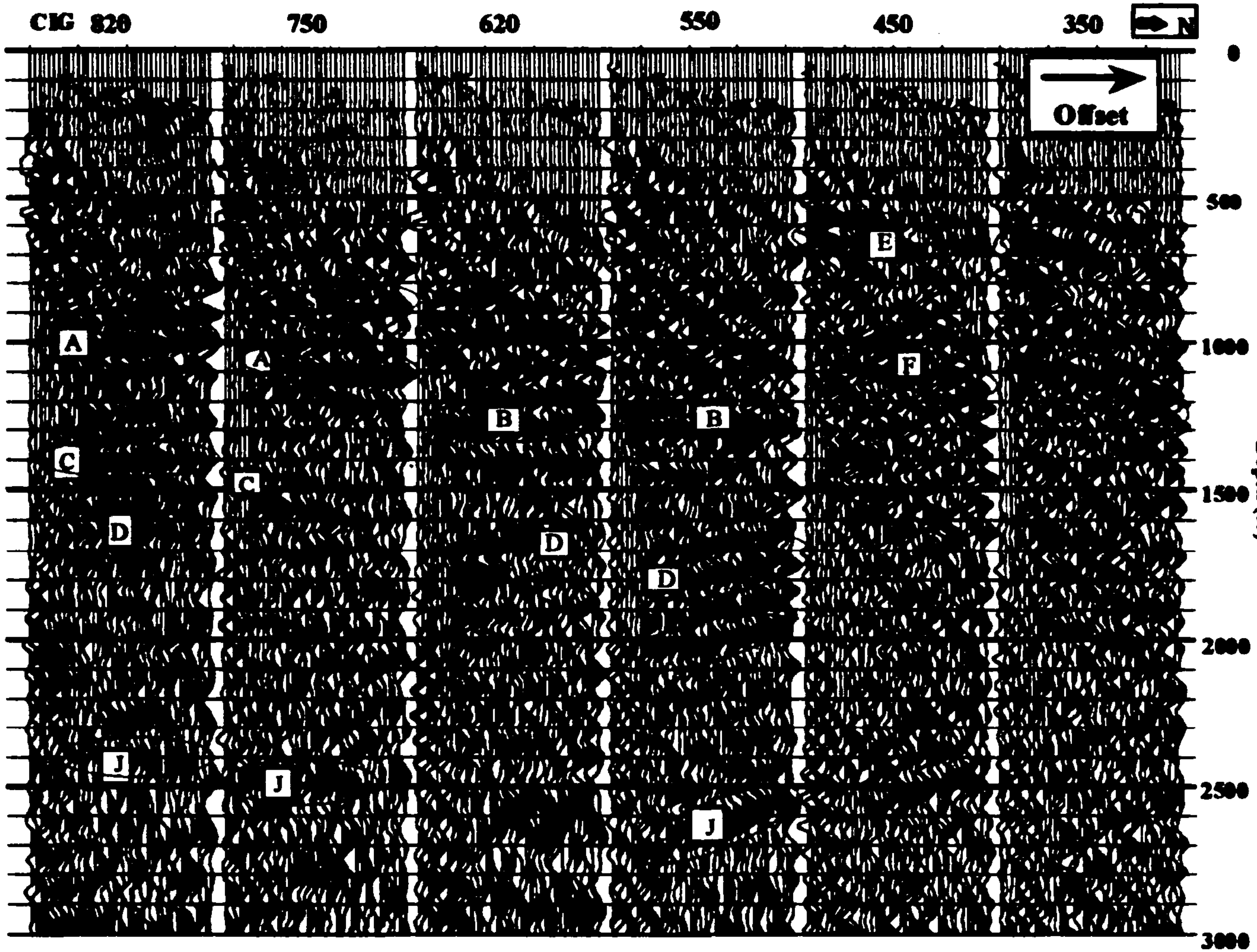

Figure 21C Selected CIG gathers displayed in VAW mode to show the flatness of events at different locations. Ellipses with letters indicate the reflections events that correspond to the migrated section (Figure 21B). Those nearly flat events (such as event A and event B) are properly migrated. Those tailed-up events (such as event D and event J) toward larger offsets are under-migrated with low velocity. Red lines indicate noise interference (residual air-wave and ground-roll).

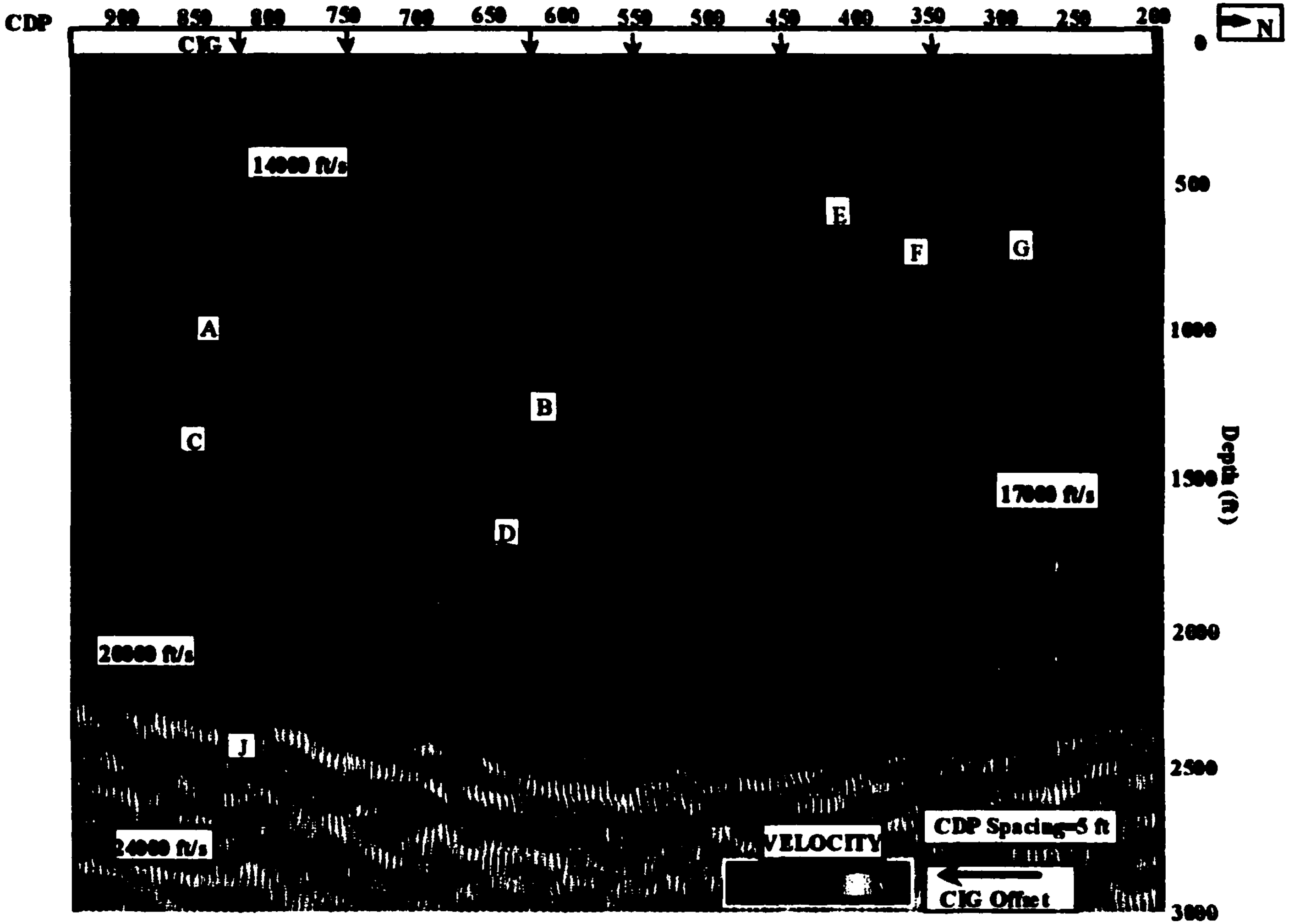

Figure 22A Second velocity--depth model for Kirchhoff prestack depth migration of Line I. This is a smoother velocity--depth model in which the fault/velocity discontinuity in Figure 21A has been removed. Green ellipses with letters indicate migrated reflection events corresponding to Figure 22B and Figure 22C. Arrows at the top of the figure indicate the CDP locations for detailed CIG gather displays (Figure 22C).

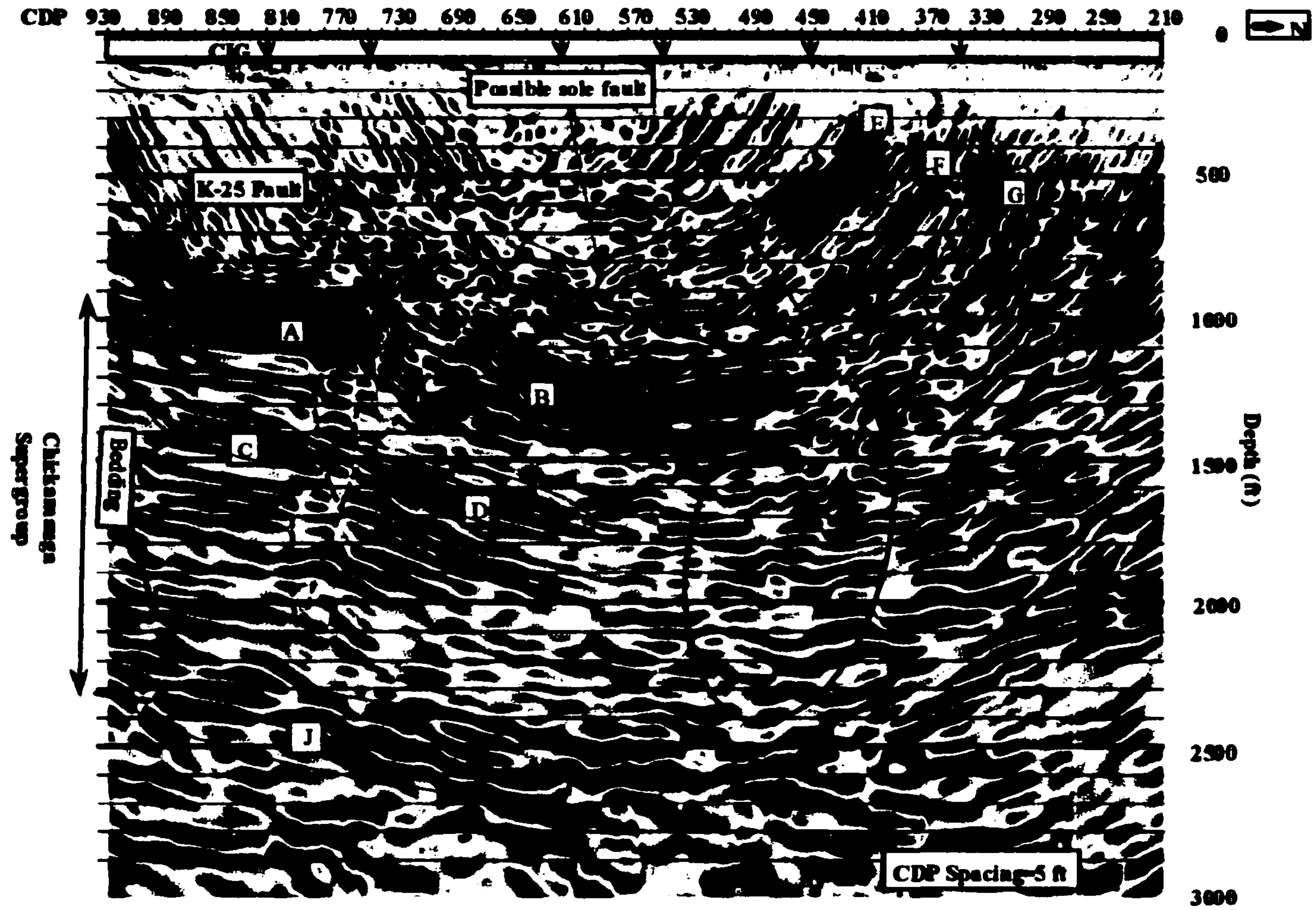

Figure 22B Prestack depth migrated section of Line I with second velocity model. Green dashed lines are interpreted reflection events denoted by letters. A and B are the K-25 Fault separating the Rome Formation from the underlying Chickamauga Supergroup. C and D are bedding plane reflections within the Chickamauga Supergroup. J is the bottom of the Chickamauga Supergroup. E and F are distinct reflections possibly from the KF-1 and KF-2 faults. Black dashed lines indicate a possible fault zone (flower structure). The polygonal box enclose a sole fault. The black ellipse indicate better reflection continuity than in Figure 21B due to a smoother velocity model.

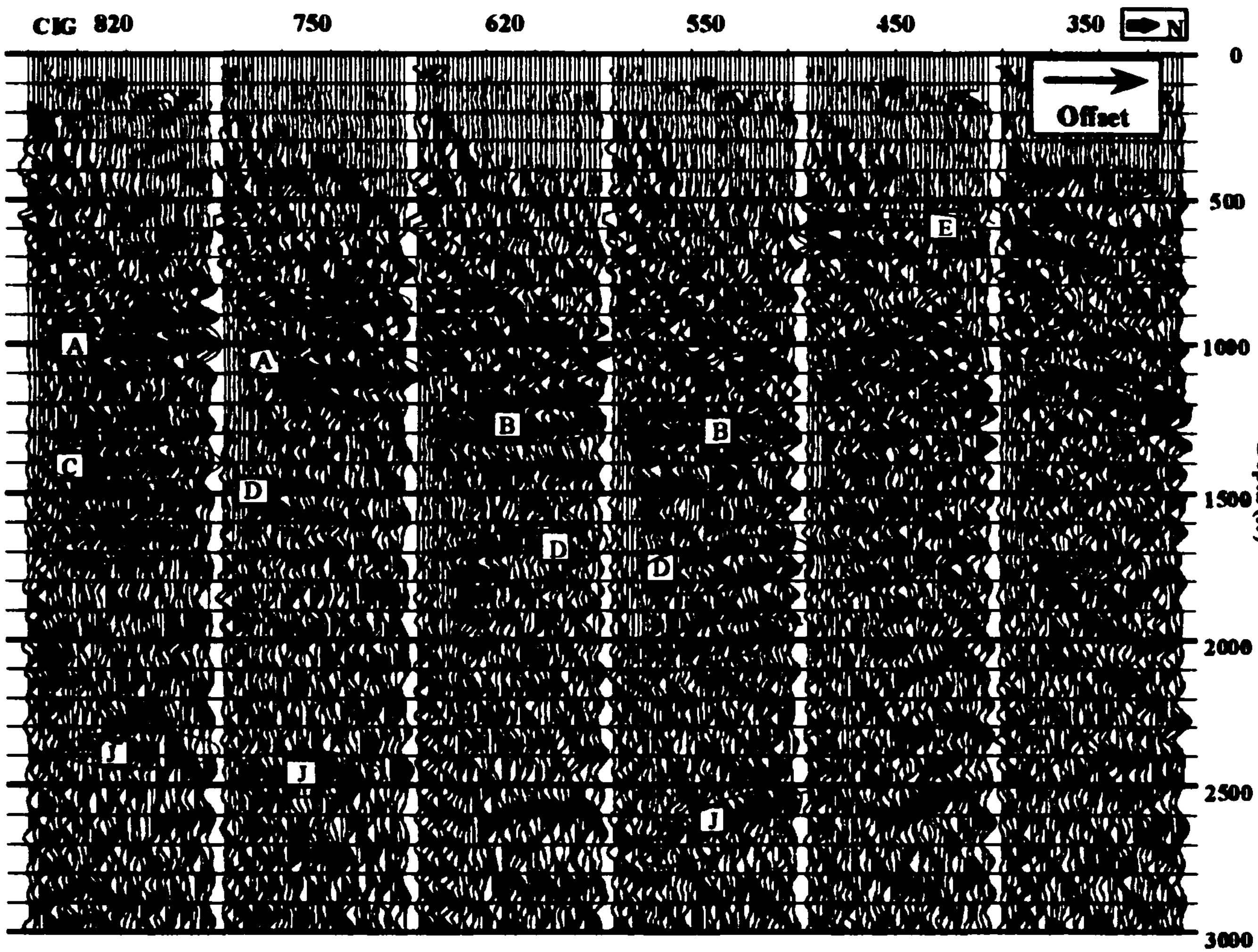

Figure 22C Selected CIG gathers displayed in VAW mode to show the flatness of events at different locations. Ellipses with letters indicate the reflections events that correspond to the migrated section (Figure 22B). Those nearly flat events (such as event A and event B) are properly migrated. Those tailed-up events (such as event J and northern part of event D) toward larger offsets are under-migrated with low velocity. Red lines indicate noise interference (residual air-wave and ground-roll).

CHAPTER 2 DATA PROCESSING OF NEAR-SURFACE SEISMIC DATA FROM THE GYPSY OUTCROP SITE, OKLAHOMA

2.1 INTRODUCTION

The Gypsy Outcrop Site is located approximately 15 miles west of Tulsa, Oklahoma (Figure 1). It was selected by British Petroleum (BP) as a test site for an integrated reservoir description program. The test site is approximately a 1200×600 ft^2 rectangle. Geologic mapping of a highway cut bounding the site is supplemented by the lithology logs from 22 shallow boreholes at 100–200 ft intervals north of the highway cut. These boreholes range in depth from 35 to 80 ft (Doyle et al., 1992).

Near-surface seismic reflection and refraction data were acquired at the Gypsy Outcrop Site through a combined effort from Conoco, University of Oklahoma, and University of Tulsa. This collaborative effort was funded by the Oklahoma Center for the Advancement of Science and Technology (OCAST) to test the use of shallow geophysical techniques to map stratigraphic boundaries between clastic sediments in an intra-borehole volume.

The objective of the seismic surveys was to map between the boreholes the boundaries found in the boreholes, and to locate boundaries beneath the boreholes. The existence of the shallow boundaries was already known from borehole coring and Ground Penetrating Radar (GPR) surveys. The seismic surveys were expected to provide more detailed lateral control for the shallow boundaries than the boreholes and deeper depth imaging (up to 150 ft) than the GPR surveys (up to 30 ft). Thus, the present seismic survey is much shorter and shallower than in conventional reflection profiling, and the resulting survey difficulties require major modifications in approach.

2.2 GEOLOGICAL SETTING

The shallow stratigraphy of the Gypsy Outcrop Site consists of the Gypsy sandstone (Figure 2). The Gypsy sandstone is an informal name for the lower most sandstone of the Vamoosa Formation of Pennsylvanian (Virgilian) age (Doyle et al., 1992). The lower contact of the Gypsy sandstone is with the marine shales and sandstones of the Tallant Formation, while the upper contact is with the Vamoosa Formation.

Six ancient river channels were mapped by Doyle et al. (1992). The lower contact of each channel sand body is erosional; and the upper contact is either erosional, cutting into younger channels, or conformable with floodplain deposits. Figure 3A is an example isopach map for one of the channel sand bodies, C1. Other channel sand bodies have similar trends (N to NW) and thickness distributions. Each of the channel sand bodies is up to 21 ft thick and 560 ft wide. Figure 3B is a schematic cross-section of the channel sand bodies (C1–C4) exposed on the north wall of the highway cut.

Suppose the dominant frequency for the seismic reflections to be 120 Hz, and the velocity to be 5000 ft/s. Then the wavelength of the seismic reflection is 41.6 ft, and the seismic resolution is 10.4 ft (a quarter of the wavelength). Because the channel sand bodies are generally more than 10 ft (up to 21 ft) thick, it is possible to image some of the channel boundaries. On the other hand, because the individual lithofacies are generally thin (less than 10 ft), their boundaries cannot be resolved. For the mudstone and siltstone facies thicker than 10 ft, it is possible to resolve the top and/or the bottom of these facies. It would be interesting to see whether the seismic reflection surveys will be able to image some of the channel boundaries and lithofacies boundaries.

2.3 SEISMIC SURVEYS

Figure 4 shows the locations of the seismic lines, including the refraction line, the CMP reflection line (Line 2628), and the expanding spread profile (ESP Line). Noise tests were carried out to determine the amount of source charge and the number of source stackings at each shot point. A source spacing of 10 ft and a receiver spacing of 5 ft were decided to give a 6 fold CMP survey for Line 2628. Whereas a 2 ft source spacing and a 2 ft receiver spacing were decided to give a 24 fold for the ESP survey. Time sampling intervals (0.1 ms for Line 2628 and 0.05 for ESP Line) were decided to record possible high frequencies. Low-cut analog filters were used for both Line 2628 and the ESP Line. Table 1 lists the survey parameters of both Line 2628 and the ESP Line.

Refraction Line

The refraction survey was carried out to obtain a velocity–depth model for the very near-surface. Because the refraction survey used first arrivals (refractions) and assumed only one refractor boundary, only a simple velocity model was obtained, including one refractor boundary and velocities above and below the refractor.

A Bison 9024 seismograph with 24 receiver channels was used for recording and a 12 gauge Betsy Shotgun was used as the seismic source. Time sampling interval was 0.1 ms; recording length 100 ms; receiver spacing 5 ft. The refraction survey used typical Generalized Reciprocal Method survey geometry. Five shots per spread are positioned for the refraction line. One shot point, the Mid-line Shot Point, is placed at the center of the line. Two shot points, i.e., the Forward Shot Point and the Reverse Shot Point, are placed at both ends of the line. Two additional shot points, the Off-end Forward Shot Point and the Off-end Reverse Shot Point, are placed at a distance of approximately half-spread away from both ends of the line.

Figure 5 shows the refraction velocity model, i.e., velocity and boundary points, obtained from the generalized reciprocal method (GRM) for the refraction line (Danbom, 1995). Solid line (red) is the interpreted refractor boundary by fitting through the points. The velocity above the refractor is 2000 ft/s. The velocities below the refractor are 5046 ft/s (west), 5516 ft/s (middle), and 3848 ft/s (east). The refraction velocity model is used for elevation statics and for seismic modeling attempt.

CMP Reflection Line 2628

Line 2628 was designed to obtain a regular CMP stacked section across BH 26-27-28. A Bison 9024 seismograph with 24 receiver channels was used for recording. A 12-gauge Betsy shotgun was used as the seismic source. Time sampling interval was 0.1 ms and the recording length was 100 ms. Source spacing was 10 ft and receiver spacing 5 ft, and a constant minimum offset of 30 ft was maintained.

Figure 6 shows the survey geometry and reflection coverage for Line 2628. A 6-fold of survey was obtained within horizontal locations of 40–350 ft along BH 26-27-28.

ESP Line

In an Expanding Spread Profile (personal communication, Danbom, 1995), the sources and the receiver spreads move in opposite directions, thus the offsets between shot and receiver spread expands/shrinks. A Bison 9024 seismograph with 24 receiver channels was used for recording. A 12-gauge Betsy shotgun was used as the seismic source and steel slugs were used. Time sampling interval was 0.05 ms and recording length 50 ms. Source and receiver spacing were 2 ft.

The ESP Line was specially designed to obtain high stacking fold and wide offset range near BH 27, using the limited number of recording channels (24) available for the Gypsy seismic surveys.

Figure 7 shows the survey geometry and reflection coverage for the ESP Line. A 24 fold of survey is obtained for the ESP Line.

Outcrop Velocity Measurements

There are five reasons to perform outcrop velocity measurements in order to obtain interval velocities needed for the seismic modeling of the ESP Line, which in turn might provide useful information toward the interpretation of the reflection events of Line 2628. First, the reflections from Line 2628 and the ESP Line are too weak and the signal-to-noise ratio is too low to obtain stacking velocities from the seismic reflection data. Second, the refraction velocity model (Figure 5) is much shallower and much less detailed than the reflection layer boundaries. Third, there is no well-log velocity measurement (i.e., sonic log) at the Gypsy Outcrop Site. Fourth, VSP velocity measurement was tried by putting a hydrophone into BH 27 filled with water and generating seismic waves with a sledge hammer near BH 27, but no seismic signal could be received, probably due to coupling problems between the ground, the PVC pipe, and the hydrophone. Fifth, there is no available laboratory velocity measurement from core samples.

Outcrop velocity measurements were carried out at the north wall of the highway cut 800 ft to the south of the seismic lines. At each measurement location on the outcrop face, a single receiver and a Single Channel Bison Seismograph were kept still, whereas a sledge hammer source and a lead source plate were moved away at 2 ft intervals. First arrival times were read from the seismograph and written down by hand. Further discussion of the outcrop velocity measurements will be presented later in the section of seismic modeling attempt.

2.4 PRELIMINARY ANALYSIS OF CMP REFLECTION LINE 2628

This section presents the preliminary analysis of Line 2628, including unfiltered shot gathers, band-pass filtering, and F-K filtering. The purpose is to find out whether there are reflections in the shot gathers and whether the reflections can be enhanced through the various filtering processes.

Unfiltered Shot Gathers

Figure 8 shows 12 unfiltered shot gathers of Line 2628. The shot gathers vary in general appearance, including arrival times of possible reflections, amplitude of air-wave noise, and amplitude and moveout of ground-roll. These variations even occur from shot to shot. The amplitude differences are probably caused by variations of shot-hole conditions such as shot-to-ground coupling, wetness of ground, and muffling of shot holes in attempt to reduce air-wave energy.

Possible reflections are marked with purple lines and 'R' (Figure 8). They are identified as events having hyperbolic curvature. However, most of these reflections span less than

10 traces out of the 24 traces in each shot gather, such as in shot 1 and shot 8. This very limited number of farther offset traces is inadequate to show the event curvature that would be expected for reflections. In addition, the possible reflections do not have consistent moveout patterns and amplitudes. The narrow trace span and the inconsistent arrival times will reduce the effective stacking-fold to less than 3-fold, regardless of the nominal 6-fold stack of Line 2628 (Figure 6). CMP Stacking will, therefore, produce very little S/N improvement.

Air-wave is marked with blue lines and 'Air' (Figure 8). The air-wave has an approximate velocity of 1100 ft/s. The air-wave has higher predominant frequency than other events (possible reflections and ground-roll). This is because air-wave travels in the air, so its high frequency components are not attenuated as much as other events. The air-wave is stronger in certain shots (1, 8, 9, 10, 12) than in others. This variation is caused by the difference in the muffling conditions of the shot holes.

Possible ground-roll is marked with green lines and 'GR' (Figure 8). These events have higher apparent velocity than the air-wave, slower apparent velocity than possible reflections, and somewhat lower frequency content than the reflections. The ground-roll is stronger in shots 5–11 than in others. This variation is caused by the changes of seismic conditions at ground surface such as shot-to-ground coupling. Inside the air-wave and ground-roll cone (illustrated in shot 1 of Figure 8), both air-wave and ground-roll exist and they dominate the shot gathers.

Band-pass Filtering

Band-pass filtering was used to separate signal from noise for Line 2628 based on frequency differences.

Amplitude spectra of the shot gathers of Line 2628 were examined and it was seen that most of the shot gathers have energy limited within 0-200 Hz. Some shot gathers show significant energy above 200 Hz, as can also be seen as the high frequency noise in Figure 8 (blue lines, 'Air').

The best trapezoidal band-pass filter was determined by progressively testing the low-cut to reject ground-roll noise which was believed to be in the low-frequency range, and by progressively testing the high-cut to reject high-frequency noise such as air wave. The best band-pass filter was decided to be (35, 70, 160, 240) Hz. This filter was applied to the shot gathers of Line 2628. Compared with the unfiltered shot gathers, air-wave and ground-roll noise have been slightly reduced, however, the possible reflections still span only a limited number of traces similar to those in Figure 8 before filtering. In addition, the band-pass filtering has increased the ringing of the wavelets, appearing as nearly parallel events in the filtered shot gathers. The failure of the band-pass filtering is due to the limited frequency spectral separation from ground-roll noise. Because improvement was so questionable, figures from band-pass filtering are not included here.

An unconventional band-pass filtering (Steeples, 1997) was also tried on the shot gathers of Line 2628. It uses very high low-cut frequency (up to 400 Hz) in the band-pass filters. In the Steeples' example, after applying the unconventional band-pass filtering, reflections stood out as strong events because of the reduction of low-frequency noise.

Following Steeples' approach, a band-pass filter – (400, 500, 1000, 2000) Hz – is applied to the shot gathers of Line 2628. Unfortunately, no reflections could be seen and everything that could be seen is noise. Re-examination of the amplitude spectra of the unfiltered shot gathers shows that the shot gathers have very low amplitude spectra for high frequencies (> 300 Hz). Therefore, either there is no reflection at all in the high frequency range (> 300 Hz) or the high frequency reflections are very weak – weaker than the background noise in the survey. Hence, in either case, the unconventional band-pass filtering would not be effective.

The lack of high-frequency coherent energy may be due to scattering from fractures, surface inhomogeneity, and the presence of water-table below most of the possible shallow reflecting boundaries.

F-K Filtering

The use of F-K to filter out linear coherent noise is well known (Yilmaz, 1991). However, many people have also pointed out the limitations of F-K filtering. Some even prefer not to use F-K filtering because it has smearing effects (Sheriff, 1991) in that seismic-trace data received by different receivers are averaged. Nevertheless, F-K filtering is an easy-to-use filtering option readily available in most seismic data processing software packages, and some people have used F-K filtering successfully on near-surface data (Yilmaz, 1991). Therefore, F-K filtering was tested to filter out the linear coherent noise (air-wave and ground-roll) of Line 2628.

Although the results of this section do not conclusively show reflections, figures showing filtering attempts are presented here because they characterize the problem of S/N separation for this data better than the band-pass attempts for which no figures were shown.

Figure 9 shows F-K filtering tests in order to determine the best F-K filter for Line 2628. Figure 9(a1) is the unfiltered shot gather 1 after elevation statics correction with a velocity of 2000 ft/s. The reason for applying elevation statics is to remove known trace-to-trace time shifts caused by elevation changes of the seismic survey thereby increasing continuity of events. The red line (R), in Figure 9(a1), as well as in Figures 15(a2)-(a5), identifies a possible reflection. Figure 9(b1) is the F-K spectrum of Figure 9(a1). It shows quite a lot of nearly parallel slopes (e.g., S1, S2, S3) with apparent velocities of approximately 1100 ft/s. They correspond with the aliased air-wave. In addition, there are other slopes that are not passing through the origin (F=0, K=0), but instead they are falling into the negative wave-number quadrangle. These are other aliased noise and they interfere with the F-K spectrum of the possible reflections. Thus, a polygonal F-K filter is more appropriate than a fan F-K filter to remove the aliased noise shown in Figure 9(b1).

An F-K polygon is drawn in Figure 9(b1) to illustrate how the polygon separates the F-K spectra of reflections from those of noise in the F-K domain. The F-K spectra of possible reflections are considered to be within the polygon. Thus the region inside the polygon is to be passed while the region outside the polygon is to be rejected. In Figure 9(b1), the lower bound of the F-K polygon is chosen to be OC, which has an apparent velocity of approximately 1300 ft/s, slightly faster than air-wave (1100 ft/s). Events slower than 1300 ft/s (inside triangle OCD) will be rejected. The upper bound of the polygon is chosen to be AB, which has the same slope as that of OC. The events S1, S2, S3, which correspond to the aliased air-wave or other aliased events, are above the upper bound of polygon and are therefore to be rejected. OA is chosen to exclude most of the negative wave numbers, which corresponds to negative moveout in the shot gathers. However, it is decided not to completely reject all the negative wave numbers, considering that some reflections have a small amount of negative moveout or they are nearly flat at small offsets. Removing all the negative wave numbers would damage these components.

Figure 9(a2) and Figure 9(b2) show the first pair of F-K filtering test. The polygonal filter in Figure 9(b2) is identical to that in Figure 9(b1). Applying the polygonal filter in Figure 9(b2) removes high-frequency components of the air-wave, but it leaves a strong residual air-wave. The F-K spectrum corresponding to Figure 9(a2) is shown in Figure 9(b2).

Figure 9(a3) and Figure 9(b3) show the second pair of F-K filtering test. In Figure 9(b3), the upper bound of the polygon is moved downward to reject the aliased event A2-B2' in

Figure 9(b2). To do so, A3-B3 is made to be parallel to A2-B2' and moved downward to exclude the F-K spectrum above A2-B2'. Other sides of the new polygon are kept the same as in Figure 9(b2). Figure 9(a3) is the shot gather after applying the polygonal F-K filter in Figure 9(b3) to the shot gather in Figure 9(a1). There is very little air-wave left in Figure 9(a3) along the blue line, as compared with Figure 9(a2). However, there is a linear event, as marked by the green line in Figure 9(a3), with an apparent velocity of 1667 ft/s. This is ground-roll and needs to be further filtered out.

Figure 9(a4) and Figure 9(b4) show the third pair of F-K filtering test. The polygonal F-K filter in Figure 9(b4) is designed to filter out the events parallel to the green line in Figure 9(a3). These events have an apparent velocity of 1667 ft/s. For this purpose, the lower bound of the F-K polygon is raised from 1300 ft/s to 2000 ft/s, with all other sides of the polygon being the same as in Figure 9(b3). Figure 9(a4) is the shot gather after applying the polygonal F-K filter in Figure 9(b4) to the shot gather in Figure 9(a1). It shows that the linear event marked in green line in Figure 9(a3) has been filtered out. The possible reflection (red line) to the right side of the air-wave looks smoother than in Figure 9(a3). The arrival times of the possible reflections look similar in both Figure 9(a3) and Figure 9(a4). The linear event marked in green is another ground-roll mode, which has become visible because the stronger, slower ground-roll has been attenuated. It has an apparent velocity of approximately 3125 ft/s.

Figure 9(a5) and Figure 9(b5) show the fourth pair of F-K filtering test. The polygonal F-K filter in Figure 9(b5) is designed further to filter out the linear event marked in green line in Figure 9(a4). The lower bound of the F-K polygon is raised even further to 3000 ft/s, as compared with the 2000 ft/s in Figure 9(b4). Figure 9(a5) is the shot gather after applying the polygonal F-K filter in Figure 9(b5) to the shot gather in Figure 9(a1). Figure 9(a5) shows that the possible reflection (red line, R) appears to be even smoother than those in Figure 9(a4). This continuity is an artifact caused by the F-K filtering. The effect of F-K smearing is even more obvious for the direct arrivals (ellipses, Figure 9) in which the number of traces crossed by reflections increases with severity of filtering (Figure 9(a1) to Figure 9(a5)). Therefore it is concluded that the polygonal F-K filter in Figure 9(b5) has over-done the F-K filtering and that the polygonal F-K filter in Figure 9(b4) is the best.

Figure 10 shows shot gathers 1-12 after applying the best F-K filter. The linear coherent events with slow apparent velocities have been filtered out and the shot gathers have become much less noisy. The shot gathers have become more consistent in waveform and amplitude. However, the possible reflection (red line, R) does not cross a sufficient number of traces to convincingly demonstrate that they are indeed reflections. Some parallel events (within red polygons) may be artifacts largely due to the narrow pass-band of the F-K filter.

Thorough F-K filter testing shows that F-K filtering reduces the amplitude of air-wave, but ground-roll is more difficult to remove. This is because ground-roll is dispersive, so that removing a strong, lower velocity ground mode results in seeing a weaker, higher velocity mode, which has nearly the same amplitude and apparent velocity of the possible reflections. If separation of ground-roll from possible reflections is further attempted, then serious smearing is introduced because the pass region of the F-K polygon has become very narrow.

Because of the failure to obtain reliable reflections, even after band-pass and F-K filtering, it was decided not to carry the processing through NMO and stacking, or alternatively, to attempt prestack partial migration (DMO), for Line 2628.

2.5 SEISMIC MODELING ATTEMPT OF ESP LINE

Seismic data processing was attempted for the ESP Line in hope that the higher survey fold of the ESP Line would produce useful information toward the data processing of the CMP Line 2628. Unfortunately, the shot gathers of the ESP Line are also very noisy and similar filtering difficulties were also encountered. Therefore, seismic raytrace modeling of the ESP Line was attempted. This section summarizes the difficulties encountered in the seismic modeling attempt.

Velocity–Depth Model

A 1-D velocity–depth model is assumed for the seismic modeling of the ESP Line, based on the fact that the CMP coverage of the ESP line is short and the refraction survey shows gentle dips near B.H. 27. It is further assumed that the velocities from the outcrop velocity measurements at the highway cut can be combined with the depth values and lithofacies units at B.H. 27 to form a 1-D velocity–depth model which is necessary for the seismic modeling of the ESP Line.

Outcrop Velocity Measurements

Figure 11 shows the time–distance curves and linear-regression of the outcrop velocity measurements. Factors such as fractures, faults, facies changes, and highway noise might affect the time-readings in the outcrop velocity measurements and are therefore noted.

Table 2 lists the channel numbers, lithofacies, and velocities from the outcrop velocity measurements at the highway cut, based on Figure 11. In this table, the velocity information (Figure 5) from the refraction survey is also incorporated.

The velocities (5054 ft/s and 5516 ft/s) of the Channel 4 X-bedded and ripple-laminated sandstone units (inside blue box, Table 2) are considered to be somewhat accurate seismic velocities for the shallow Gypsy Sandstone. These velocities were based on the shallow refraction survey (Figure 5) and many data points of P-wave first arrival times were used to obtain these refractor velocities through the generalized reciprocal method (S. Danbom, 1995, Personal communication). The two red boxes in Table 2 show the velocities (3930 ft/s, 4563 ft/s, 4433 ft/s) of X-bedded sandstones inside Channel 6. The velocity value of 8095 ft/s inside Channel 4 seems to be a good value considering that typical velocity of consolidated sandstone to be > 10000 ft/s and that the sandstone unit is less consolidated at the near-surface and not filled with water.

However, even the velocities marked in the colored boxes in Table 2 are questionable because they are slower than 50% of the velocities obtained by F.Z. Wang (1994) for the Gypsy Downhole Site, —19 miles NW of the Gypsy Outcrop Site. Through the interpretation of horizontal path logs from a depth of 700 ft to 1300 ft, Wang found that in the Gypsy interval (920 -1020 ft) the velocities were 11,200 ft/s and 10,900 ft/s for the upper and lower Gypsy formation, respectively (F.Z. Wang, 1994, p. 34). This was slower than the overlying shales and underlying marine sandstone (12,500 and 12,700 ft/s, respectively). Considering that porosity may reach 20% in the Gypsy formation and that the water table is above the Gypsy formation at the Gypsy Downhole Site, the Time-Average Equation suggests that the matrix velocity would be somewhat higher than the above figures.

Because the water-table at the Gypsy Outcrop Site is deeper than 60 ft, it is reasonable to assume than the lithofacies of the outcrop face are dry with air-filed porosity. Assuming the shallow sandstone velocity to be V=4500 ft/s, the velocity in air to be Vf=1100 ft/s, and the sandstone matrix velocity to be Vm=13000 ft/s, then the time-average equation states that

$$\frac{1}{V}=\frac{\phi}{Vf}+\frac{1-\phi}{Vm}$$

where ϕ is the sandstone porosity; V – sandstone velocity, Vf – fluid (air) velocity; Vm matrix velocity.

Solving for ϕ yields a value of 16.7%. On the other hand, a porosity value of 20% would give a velocity value of 4109 ft/s, while 25% a value of 3509 ft/s, for the shallow sandstone, keeping constant the velocities in air and in the sandstone matrix.

Because the porosities of the Gypsy sandstones could reach 20%, sandstone velocities could be as low as 4109 ft/s; in case of high porosity of 25%, then sandstone velocities could be as low as 3509 ft/s. Therefore, the velocities in Table 2 higher than 3500 ft/s are possible. However, the velocities slower than 3000 ft/s in Table 2 are very questionable, because this would require porosities as high as 35%.

The smaller velocities than expected from the time-average equation and the variations of velocities are possibly caused by the following factors:

1) Fractures are open in the near surface (15 ft depth), due to highway outcrop blasting. This causes the velocities to be even smaller than predicted by the time-average equation.

2) Severe weathering are present at the outcrop face due to highway outcrop blasting, making the shallow units much less consolidated, therefore slower in velocity.

3) Some of the velocities in sandstones measured at the highway cut are approximately the same (such as those marked in colored boxes). However, many of the velocities measured in these same units (marked by dots in Table 2) are extremely low, being

less than 1/4 the velocities measured in the downhole site by F.Z. Wang (1994). Velocities in units of similar lithologies (marked by stars) are also widely scattered.

4) The large velocity variations for the same lithofacies in Table 2 are not plausible. Maybe the assumption of measuring the direct P-wave velocity is incorrect at the Gypsy Outcrop Site. Direct P-wave first arrival time was assumed to be read from the oscilloscope of the single channel Bison seismograph, using a vertical component geophone as the receiver. However, with a sledge-hammer source hitting downward, a down-going P-wave was generated. But the vertical component geophone might have only detected a small portion of the motion of the direct arrival, which was mostly horizontal, and therefore the vertical portion could be very weak. In order for the vertical component of motion to be strong, the receiver has to detect the motion of a down-going and then up-going P-wave (diving wave) or refraction. But this might not be the case. The geophone might have detected a much stronger and yet later arrival such as ground-roll and/or converted P-SV wave, rather than the P-wave. Because the display of the oscilloscope was so limited in viewable area and in dynamic range, there was no way of making sure of measuring the first arrival of the P-wave. Therefore, the measured velocities might be the P-SV and/or the ground-roll velocities.

Seismic Modeling Attempt

Due to the difficulties discussed above, it is decided that the velocity–depth model based on the outcrop velocity measurements is far from accurate. Even though seismic modeling based on this incorrect velocity model was attempted, the results will not be presented here, because this might introduce incorrect generalization and thus erroneous conclusions.

2.6 INTERPRETATION OF EVENTS IN SHOT GATHERS OF ESP LINE

Figure 12 shows the interpretation of events in shot gathers of the ESP Line, based on characteristics of events similar to those in Figure 8 for the CMP Line 2628. The air-wave and the ground-roll are interpreted based on linear moveout. The air-wave has a typical apparent velocity of 1100 ft/s (blue lines, Figure 12). Multiple ground-roll modes exist in some shot gathers and have apparent velocities in the range of 1200–3000 ft/s.

Only one reflection event (red lines, R, Figure 12) is interpreted based on reasonable curvature and apparent velocity. Other reflection events are too weak to be seen. The explanation for the lack of reflections in the real data is that the velocity contrasts are too small, thus only very weak reflections are observed from layer boundaries under BH 27.

Because all shot gathers are centered at B.H. 27, and because the receivers are finer-spaced (2 ft for ESP Line, vs. 5 ft for CMP Line 2628), the shot gathers are more consistent in moveout pattern and in amplitudes. As the minimum offset of the shot–receiver spread decreases from 98 ft (shot 1) to 14 ft (shot 22), air-wave and ground-roll interference becomes more serious. The near-offset shot gathers (19 and 22) have no indication of the possible reflection event. The far-offset shot gathers seem to contain more reflection information.

2.7 COMPOSITE WALK-AWAY DISPLAY

Figure 13 is a composite walk-away display formed by juxtaposing three shot gathers of the ESP Line so that they appear as one shot gather with continuous offsets and an offset range equal to that of Line 2628, but with denser trace spacing. Events recognizable on the composite walk-away will be a guide in identifying the same event on shot gathers from Line 2628, which has a lower S/N ratio and a lower trace density.

In Figure 13, event types are a lot easier to recognize, compared with those in the individual shot gathers of the ESP Line (Figure 12). Air-wave (blue lines), ground-roll (green lines) and refraction dominate the composite walk-away. The reflection event (solid purple line, offset range 70–144 ft) occupies only a small part of the composite walk-away. The dashed purple line shows the projection of the reflection event along a possible hyperbolic trajectory, with a two-way zero-offset traveltime to be approximately 27 ms. It has a depth of approximately 67.5 ft, assuming an average velocity of 5000 ft/s. This depth is approximately at the boundary between the Gypsy Sandstone and the Tallant Marine Sandstone.

The green dots show the equivalent CMP traces for Line 2628 if it were for the same survey geometry as of Line 2628. Only 3 valid traces, which are in the far offsets of the composite walk-away, would be in the equivalent CMP gather, because the other 3 traces are in the air-wave and ground-roll interference. It is almost impossible to recognize a reflection if only three traces are present. A lot more traces are present in the composite walk-away display, so it is more advantageous.

2.8 CONCLUSIONS AND RECOMMEDNATIONS

The trapezoidal band-pass filtering of Line 2628 has failed due to the lack of spectral separation between possible reflections and the air-wave and ground-roll noise.

It was very difficult to remove the dispersive ground-roll noise modes present in the shot gathers of Line 2628 by the F-K filtering, because removing a stronger and lower-apparent velocity ground-roll mode made a weaker and higher-apparent ground-roll mode. The remaining ground-roll modes have approximately the same amplitudes and apparent velocities as the possible reflections. Further F-K filtering of these modes introduced serious smearing artifacts. Therefore the F-K filtering should not be applied at all for Line 2628.

Seismic modeling was attempted in an effort to predict the possible reflections of the ESP Line. However, the velocities needed for the seismic modeling could only be obtained through the outcrop velocity measurements at the highway cut and combined with the refraction velocities. Even though some velocities look reasonable, assuming sandstone porosities of up to 25% with air in the pore space, most of them are too low and they vary a lot even for the same lithofacies in the shallow Gypsy stratigraphy. Fracturing, weathering, and the detection of the wrong type of the seismic wave were considered possible causes for the velocities being very low. Because of the inaccuracy of the velocity–depth model, it was decided not to present the seismic modeling results.

The interpretation of events in shot gathers of the ESP Line showed that only one possible reflection event exists and that the far-offset shot gathers have less interference from air-wave and ground-roll noise.

The composite walk-away display convincingly illustrated that only one reflection event exists in the far offsets, and that the near offsets are dominated by noise. The possible reflection, which is at approximately 27 ms in two-way time, is at a depth of approximately 67.5 ft, assuming an average velocity of 5000 ft/s. The depth of the possible reflector is approximately at the boundary of the Gypsy Sandstone vs. Tallant Marine Sandstone. Therefore the Gypsy Sandstone stratigraphy seems to be seismically indistinct.

The composite walk-away display suggests that if a real walk-away noise test were carried out, then we would not expect the ESP survey to bring in any substantial improvement on the recognition of reflections. In other words, we should have carried out the walk-away tests before doing the CMP Reflection Survey (Line 2628) and the

ESP Survey. Walk-away noise tests are strongly recommended for near-surface seismic study sites with similar difficulties as the Gypsy Outcrop Site.

Another recommendation based on the composite walk-away display is that fine receiver spacing (2 ft) and a lot of receiver channels (e.g., 96) should have been used in the CMP Reflection Line 2628. These survey parameters would have been similar to the composite walk-away display, thereby providing enough traces in the far offsets. In addition, longer recording time length (100 ms) is recommended because there might be reflections at deeper depth.

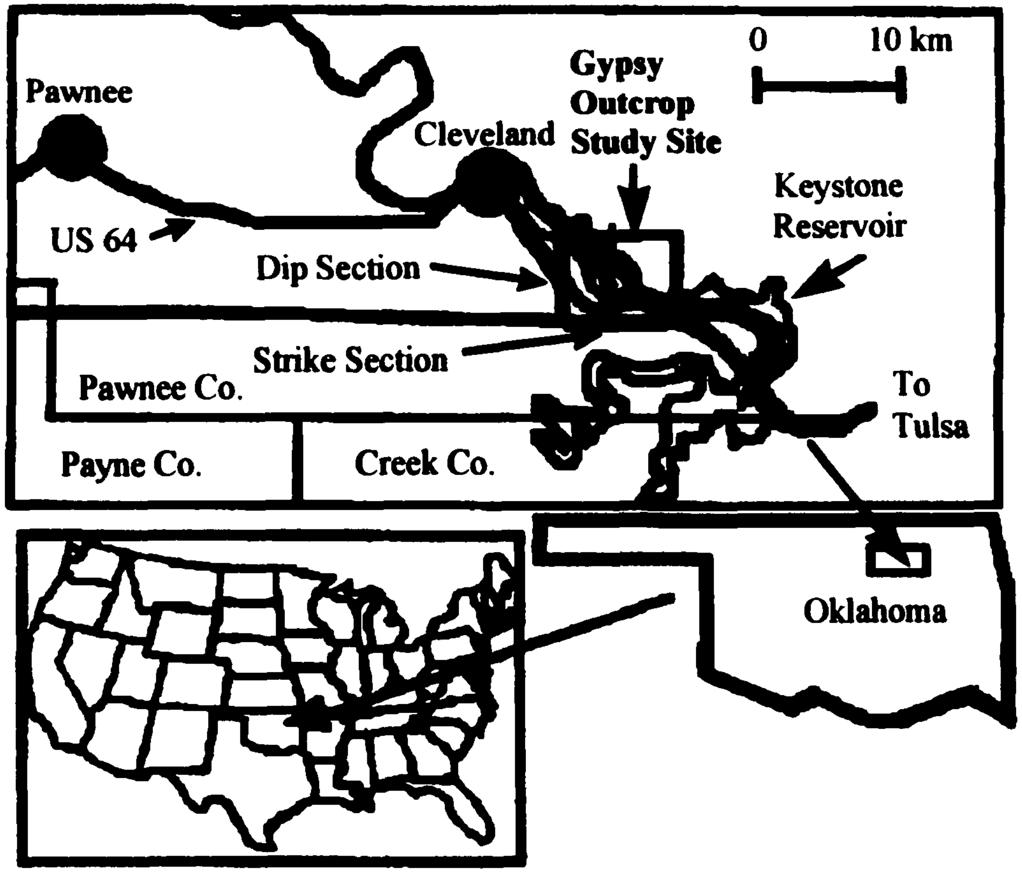

Figure 1 Location map showing Gypsy Outcrop Site, approximately 15 miles west of Tulsa, Oklahoma (modified from Doyle et al., 1992; Deng, 1996). The Gypsy Outcrop refers to the north wall of the strike-section of the roadcut of the US highway 64, unless specially noted.

Age	Group	Formation	Surface Stratigraphy	Informal Subsurface Markers
Pennsylvanian	Virgilian	Pawhuska	Turkey Run Ls.	Barnes Sd.
		Vamoosa	Kanwaka Sh. Eigin Ss.	
			Wyona Ss. Cheshewalla Ss.	Endicott Sd.
	Missourian	Tallant	Revard Ss.	
			Big heart Ss.	Tonkowa Sd.
		Barnsdall	Okasa Ss.	

↕ Gypsy Sandstone (Wyona Ss. / Cheshewalla Ss. – Endicott Sd.)

Figure 2 Shallow stratigraphy of the Gypsy Outcrop Site (modified from Doyle et al., 1992), which consists of the Gypsy sandstone of the lower-most Vamoosa Formation of Pennsylvanian (Virgilian) age. Ls.=limestone; Ss.=sandstone; Sh.=shale; Sd.=sand.

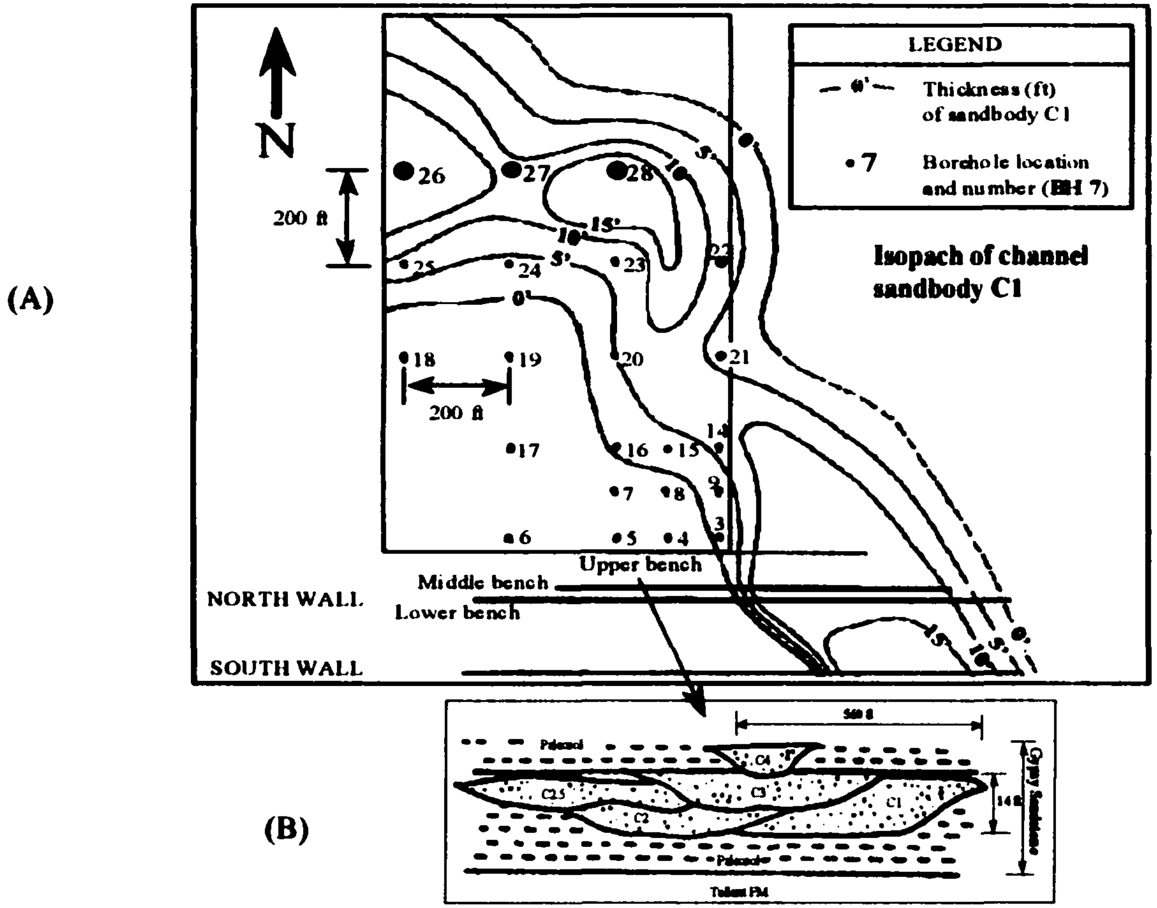

Figure 3 Example isopach map of one of the channel sandbodies (C1) and cross-section of all named channel sandbodies (modified from Doyle et al., 1992). (A) Isopach map of channel sandbody C1 at the Gypsy Outcrop Site based on lithology logs at 22 boreholes. The north and south walls of the highway roadcut are shown. (B) Schematic cross-section of stacked channel sandbodies exposed on the north wall.

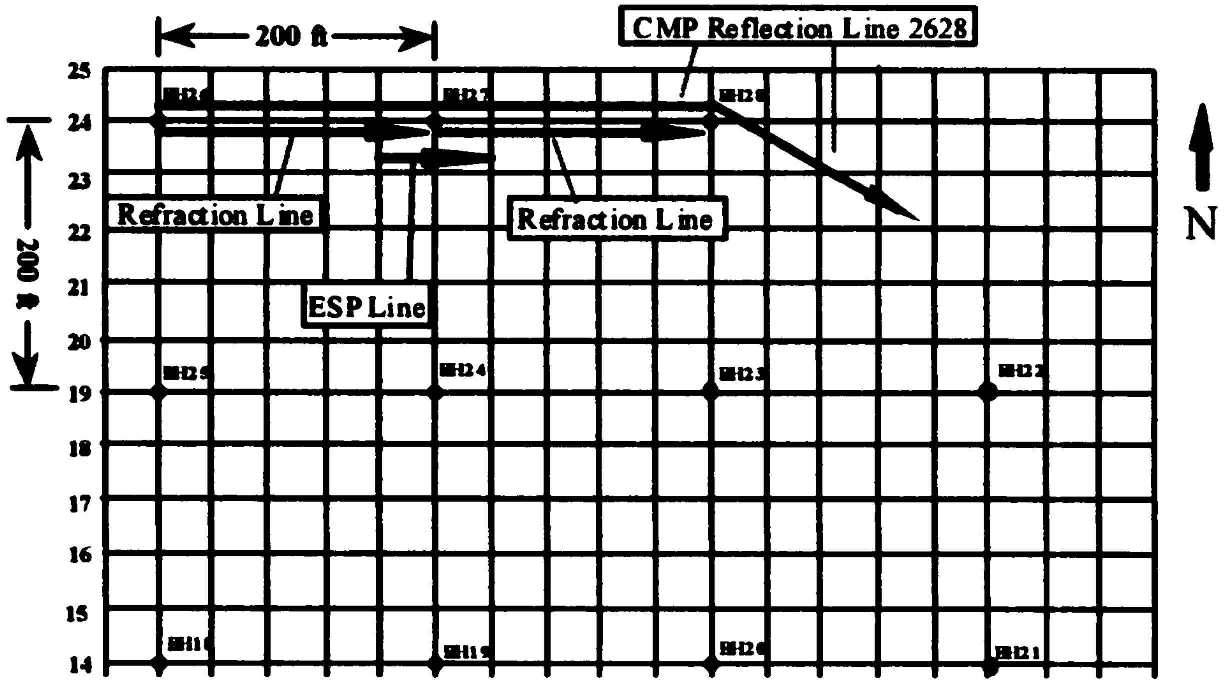

Figure 4 Locations of the seismic surveys at the Gypsy Outcrop Site (modified from Richard Weindell, 1997, personal communication). The seismic surveys include the refraction line, the CMP reflection line (Line 2628), and the expanding spread profile (ESP). Seismic lines occupy the same line location along BH26-27-28. The highway cut is approximately 800 ft to the south of BH 26-27-28.

Source of information	Observers' data sheet (from S. Danbom)
Name of survey	CMP Reflection Line 2628
Date of acquisition	Nov., 1994
Type of seismic source	12 gauge Betsy Shotgun
Recording Instrument	Bison 9024 seismograph, 24 channels
Geophone peak freq.	30 Hz
Recording frequency	Low cut 124 Hz, high cut 500 Hz
Sampling interval	0.1 ms
Record length	100 ms (equivalent to approximately 200 ft in depth)
Receiver spacing	5 ft
Source spacing	10 ft
First shot location	30 ft west of BH 26; (Source spacing, i.e., source move-up=10 ft)
First receiver spread	0 ft ---115 ft at 5 ft receiver spacing. Receiver move-up = 10 ft.
Source-receiver offset	Minimum = 30 ; maximum = 135;
Number of shots	37
Source stacking	3 shots

(A)

Source of information	Observers' data sheet (from S. Danbom)
Name of survey	Expanding Spreading Profile
Date of acquisition	Nov. 29, 1995
Type of seismic source	12 gauge Betsy shot gun
Recording Instrument	Bison 9024 seismograph, 24 channels
Geophone peak freq.	30 Hz
Recording frequency	Low cut 300 Hz, high cut 1000 Hz
Sampling interval	0.05 ms
Record length	50 ms (equivalent to approximately 100 ft in depth)
Receiver spacing	2 ft
Source spacing	2 ft
First shot location	58 ft west of BH 27 (flag 1@ 140 ft east of BH 26, move forward at 2 ft interval)
Source-receiver offset	Minimum = variable (0) , maximum = 142;
Number of shots	24
Source stacking	3, later changed to 2.

(B)

Table 1 Seismic survey parameters at the Gypsy Outcrop Site.
(A) Line 2628 (B) ESP Line

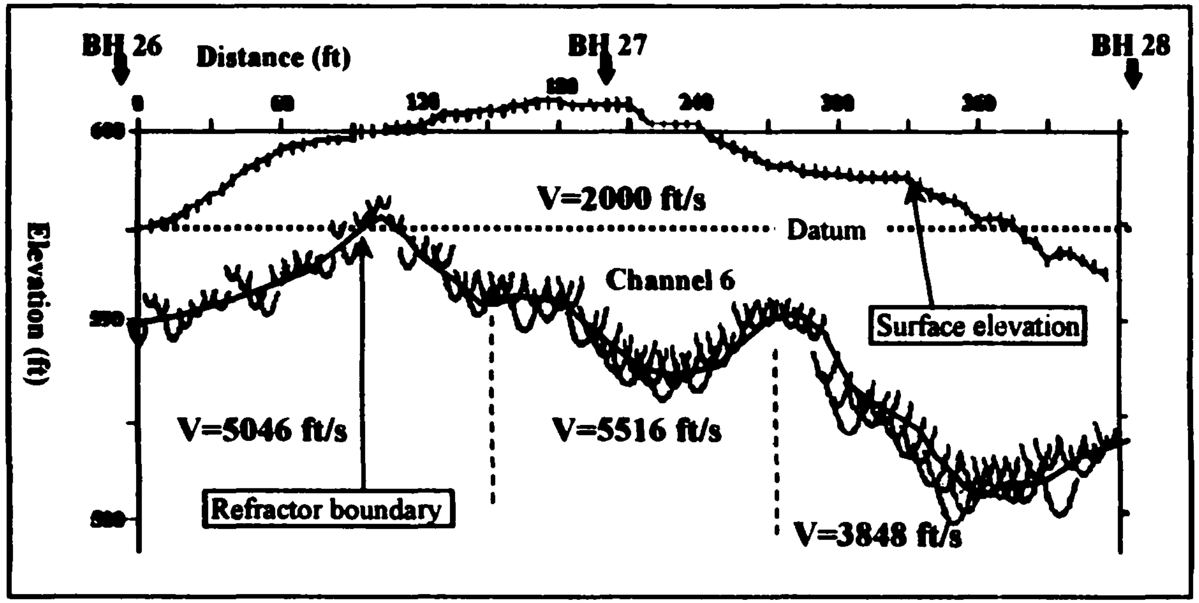

Figure 5 Velocity and refractor boundary points obtained from the Generalized Reciprocal Method for the refraction line (modified from Danbom, 1995). Solid line (red) is the interpreted refractor boundary by fitting through the points.

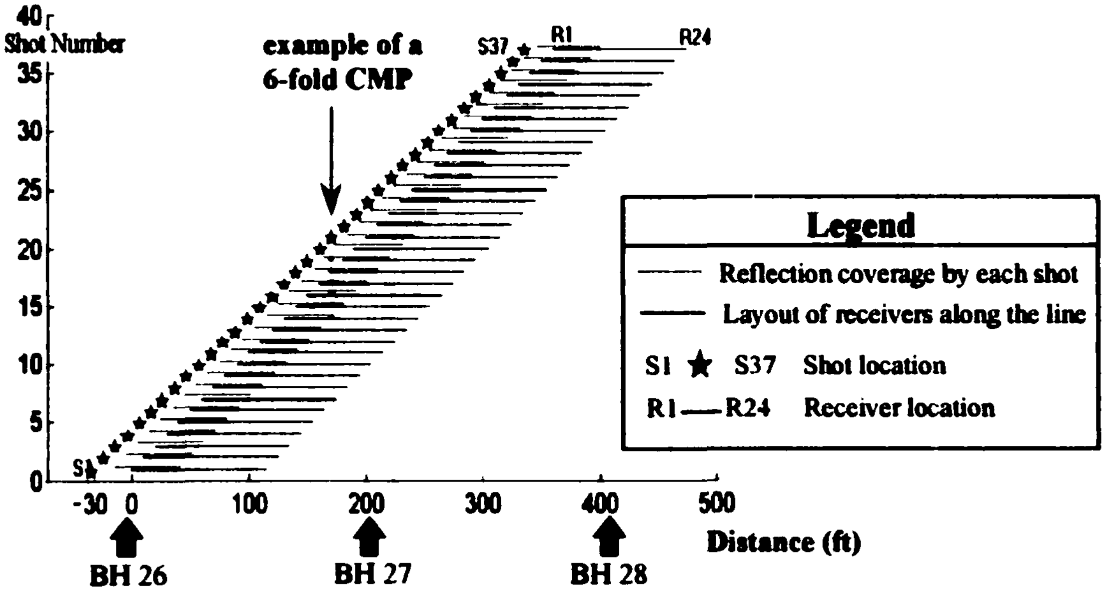

Figure 6 Survey geometry and reflection coverage for Line 2628. The shots and the receivers were laid out along BH 26-27-28, with reflection coverage (red lines) for the entire line, resulting in 6-fold of survey (blue dots) for the CMPs at 40--350 ft.

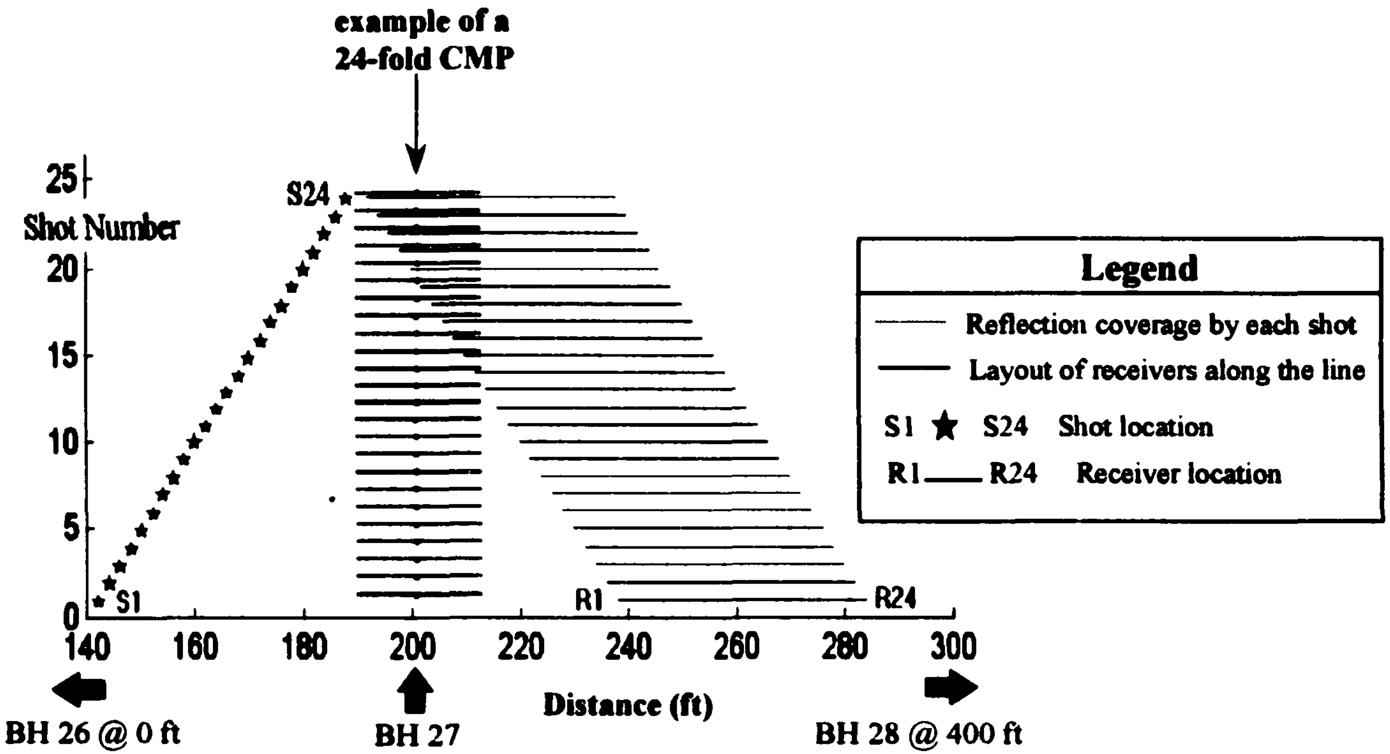

Figure 7 Survey geometry and reflection coverage of the ESP Line near BH 27. The shots and receivers were all laid out along BH 26-27-28, with reflection coverage (red lines) centered at BH 27, resulting in a constant 24 fold of survey (blue dots) for CMPs at 188-212 ft.

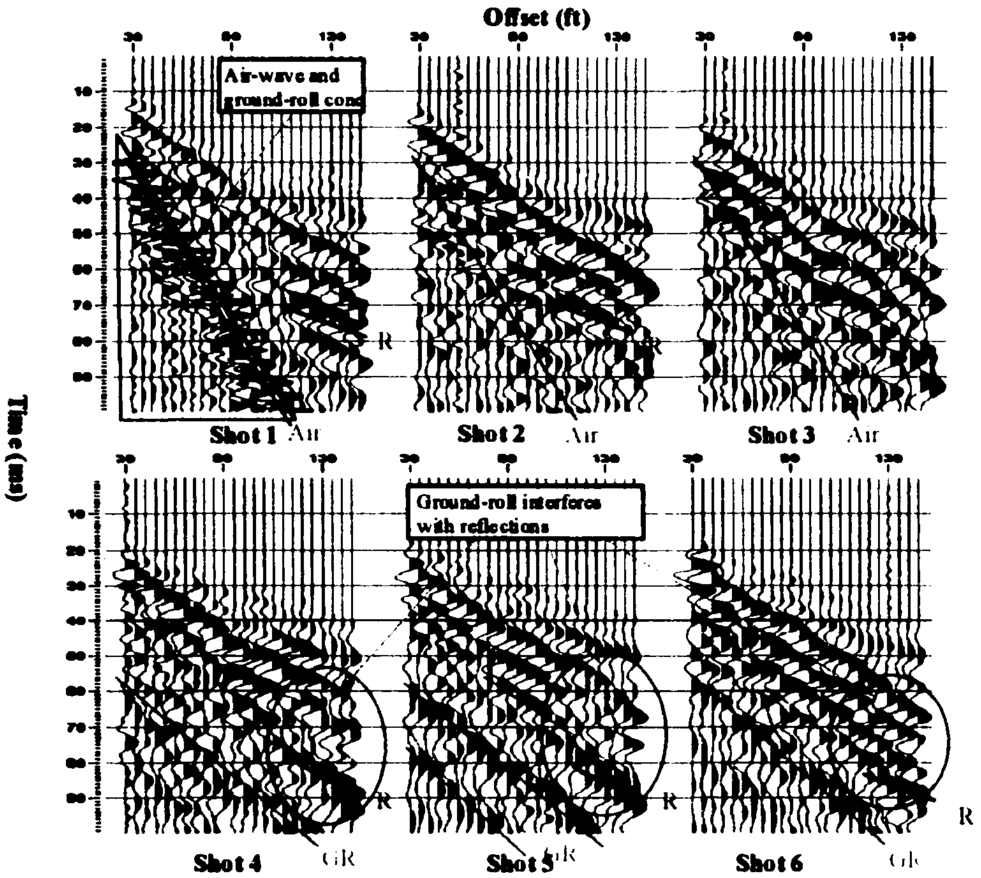

Figure 8 Unfiltered shot gathers 1-12 for Line 2628. Possible reflections (R, purple lines), and air-wave (Air, blue lines) and possible ground-roll (GR, green lines) are identified in the shot gathers. The triangle shows an example region of air-wave and ground-roll noise cone where both air-wave and ground-roll exist and dominate the shot gather. Ground-roll also exists beyond the air-wave and ground-roll cone and the ellipses show example locations where ground-roll interferes with reflections.

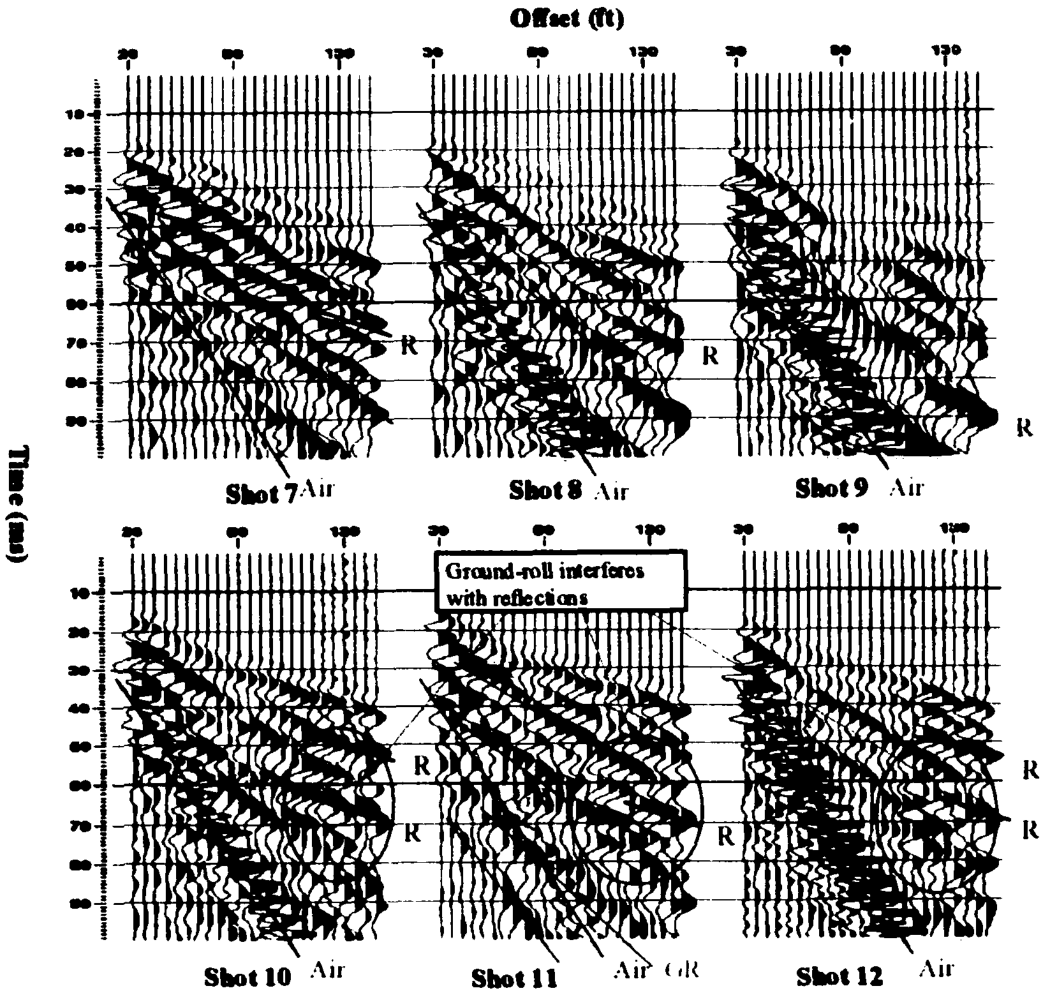

Figure 8 (Continued) Unfiltered shot gathers 1-12 for Line 2628.

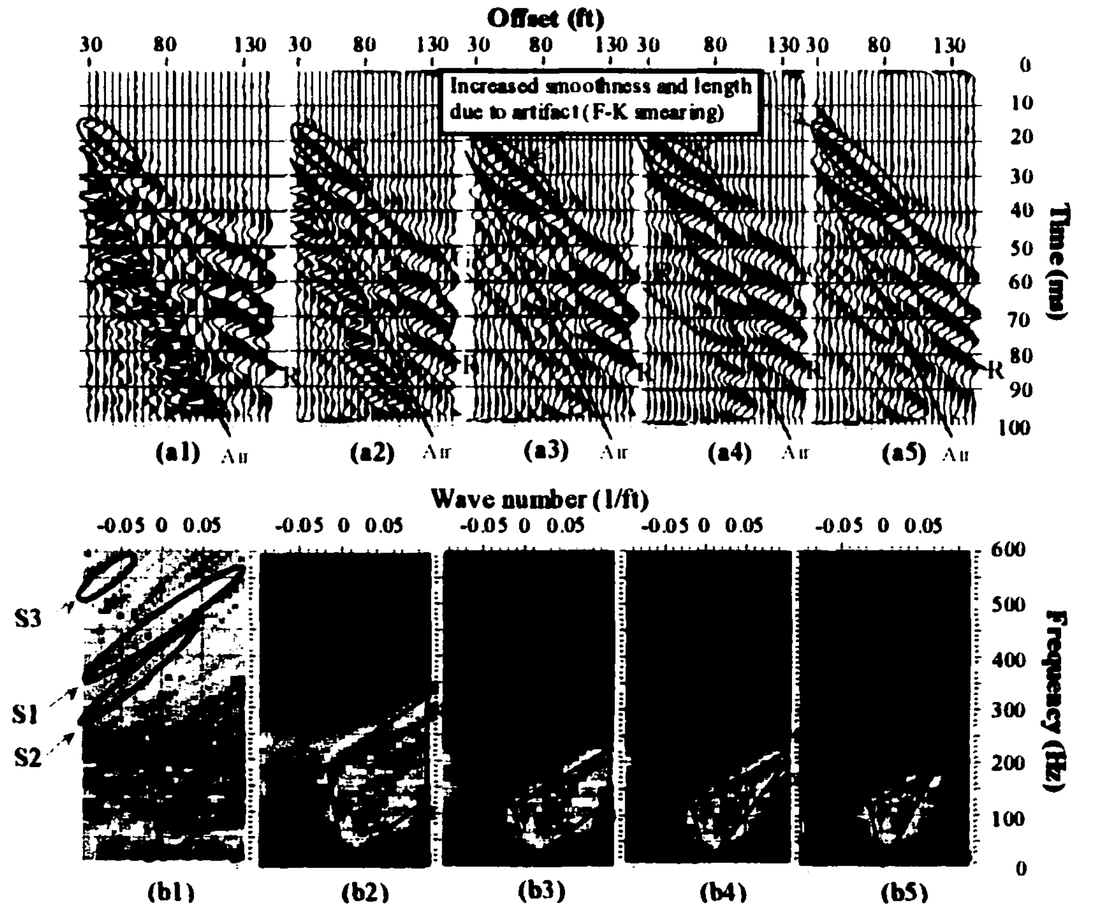

Figure 9 F-K filter tests of Line 2628. (a1) Unfiltered shot gather 1 after elevation statics was applied; (b1) F-K spectrum of (a1). (a2)--(a5) shot gathers after filtering using the polygonal F-K filter in (b2)--(b5). The red line (R) identifies a possible reflection. (b2)--(b5) F-K spectra corresponding to (a2)-(a5), along with the F-K polygonal filters to be used on data in (a1) to obtain (a2)--(a5). The polygons are the pass regions of the ideal filters and they narrow down both the aliased coherent noise (upper bound of the polygons) and the unaliased coherent noise (lower bound of the polygons) as they progress from (b2) to (b5).

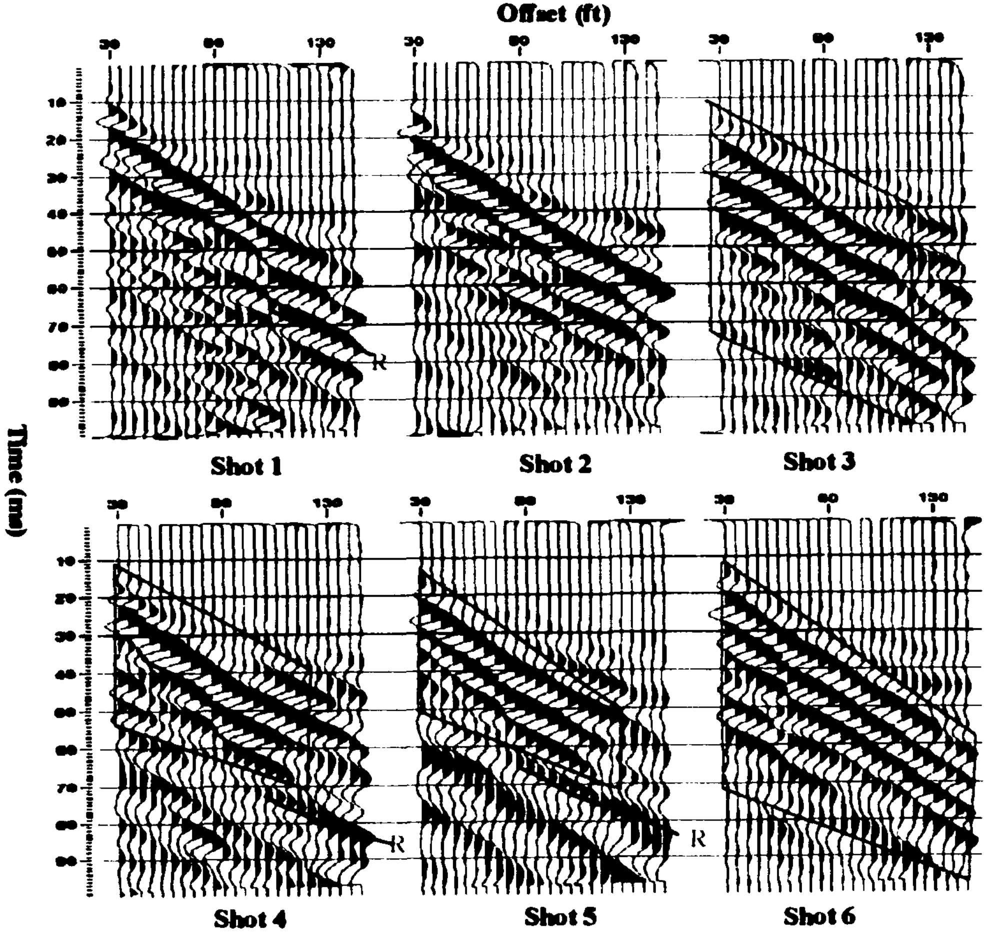

Figure 10 F-K filtering result using the best polygonal F-K filter in Figure 9(b4). Events with red lines (R) are possible reflections. The parallel, nearly-linear, events inside polygons are unlikely to be reflections.

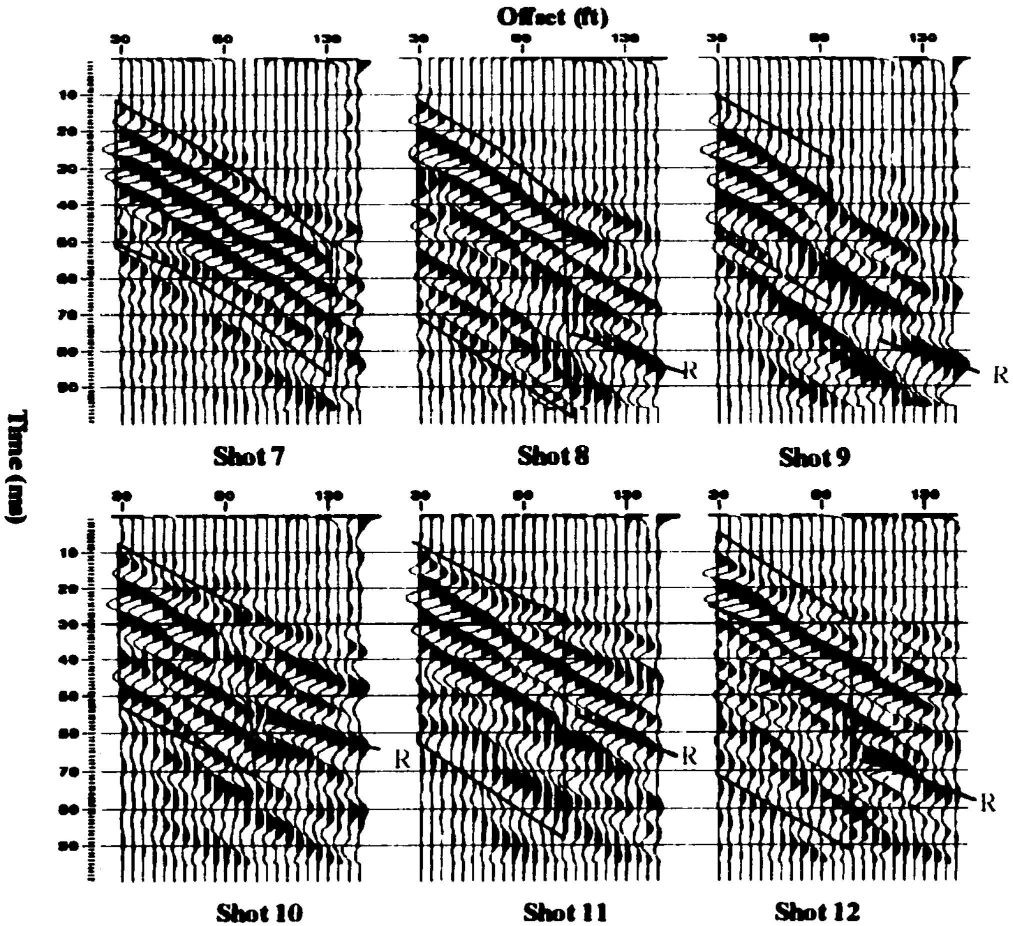

Figure 10 (Continued) F-K filtering result using the best polygonal F-K filter in Figure 9(b4).

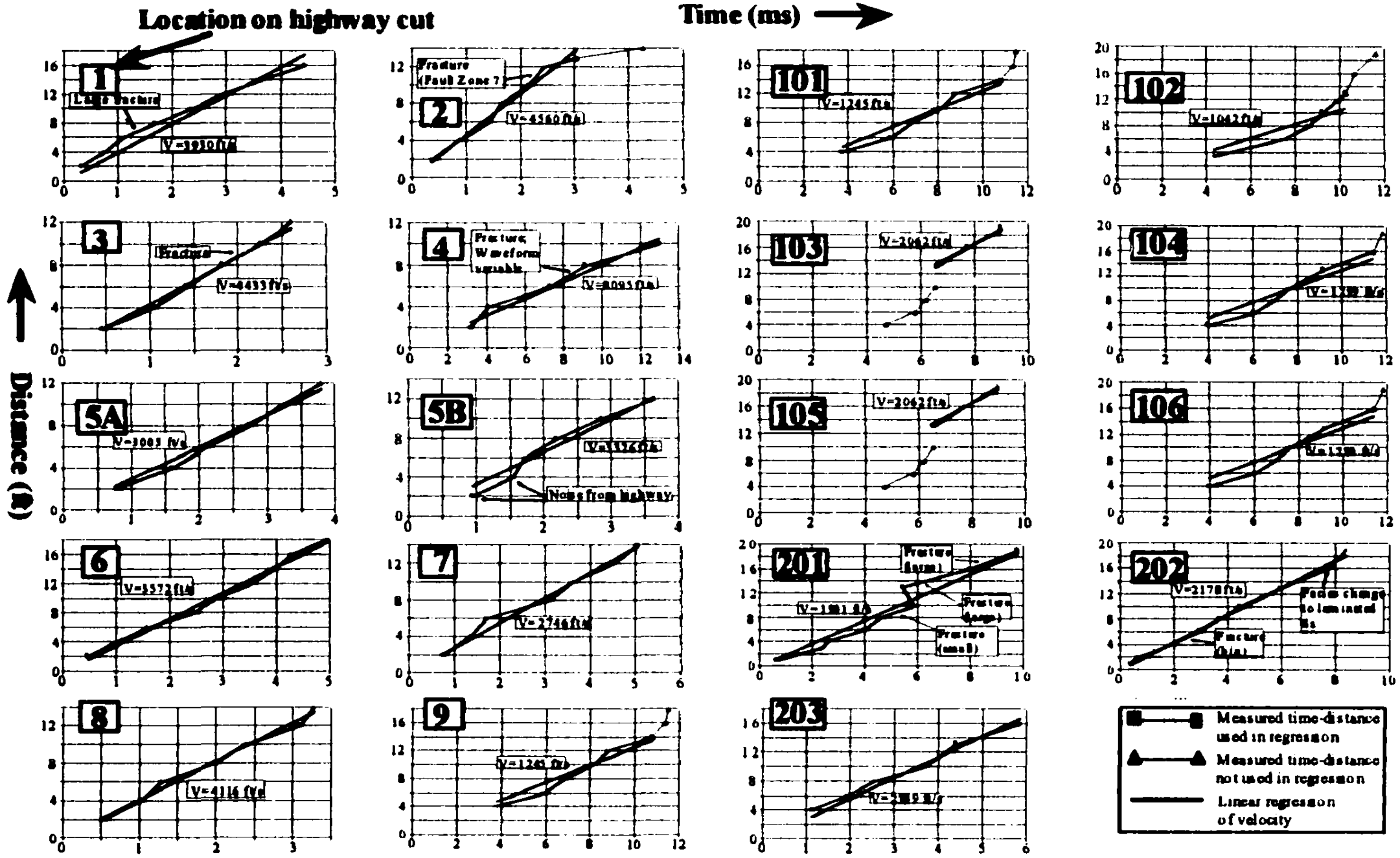

Figure 11 Outcrop velocity measurements and linear regression (straight lines) of time--distance curves to obtain velocities in the lithofacies at the highway cut. Triangular data points are excluded from the linear regression because they deviate from linear trend. Fractures, faults, facies changes, and highway noise are factors that cause errors in time readings. More points in fitting means higher quality in the linear regression.

Chan	Lithofacies	Location	Vel. (ft/s)	Quality	Method	Comments
6	X-bedded plan-bed	BH 26-27-28	2000 ●	low	Refraction Survey	Few points observed; Highly weathered; exposed at surface
6	X-bedded	Loc. 1	3930	Med.	Outcrop Velocity	Usually 4-8 points observed. Fractures result in lower velocities.
6	X-bedded	Loc. 2	4560	Med.	Same	Same as above
6	X-bedded	Loc. 3	4433	Med-high	Same	Same as above
6	ripple lam	Loc. 5A	3005	Med-high	Same	Same as above
6	X-bedded	Loc. 201	1901 ●	Med-high	Same	8 points fitting. Fractures may be the cause of low velocity values.
6	X-bedded	Loc 202	2178	High	Same	Good fitting.
4	X-bedded ripple lam	BH 26-27-28	5054 5516	High	Refraction Survey	20-30 points observed. Unexposed boundary. Layers from GRM method.
4	ripple lam	Loc. 4	8095 ★	Med	Outcrop velocity	Possibly seeing channel 4 velocity.
4	ripple lam	Loc. 5B	★3326	Low-med	Same	First two points may be noise.
4	plain bedded	Loc. 6	3572	Med-high	Same	Fitting of 9 points is good.
4	plain bedded	Loc. 7	2746 ●	Med-high	Same	Fitting of 7 points. Seeing velocity of top of channel 4.
4	ripple lam	Loc. 8	4116	Med-high	Same	Fitting of 7 points looks good.
4	X-bedded	Loc. 105	1379 ●	Low	Same	Rough fitting of only 5 points; Time reading errors due to waveform(?)
4	Ripple lam	Loc. 106	★1157	Low-med	Same	Rough fitting. 50 ft E. of location 105.
3	ripple & plain bedded	Loc. 101	1403 ●	Low	Outcrop velocity	Only 4 points to fit in line. Other 3 points wrong (?) in reading due to waveform change. Facies change.
3	plain bedded	Loc. 102	1042 ●	Low	Same	Only 4 points to fit in line (poor). Error in time reading (?).
3	plain bedded	Loc. 103	2062 ●	Low	Same	Only 3 points fit in line. Time reading for first 4 points may be wrong.
3	plain bedded	Loc. 104	1299 ●	Low-med	Same	Fitting of 7 points into rough line.
1	X-bedded	Loc. 203	2039	High	Same	Fitting of 6 points. In channel 1 at Cimmaron turnpike level.

Table 2 Listing of channel numbers, lithofacies, locations of velocity measurements, velocity values obtained, quality of velocity measured, type of velocity measurement and comments about factors affecting quality. The locations and velocities correspond to those shown in Figure 17. More data points means higher quality.

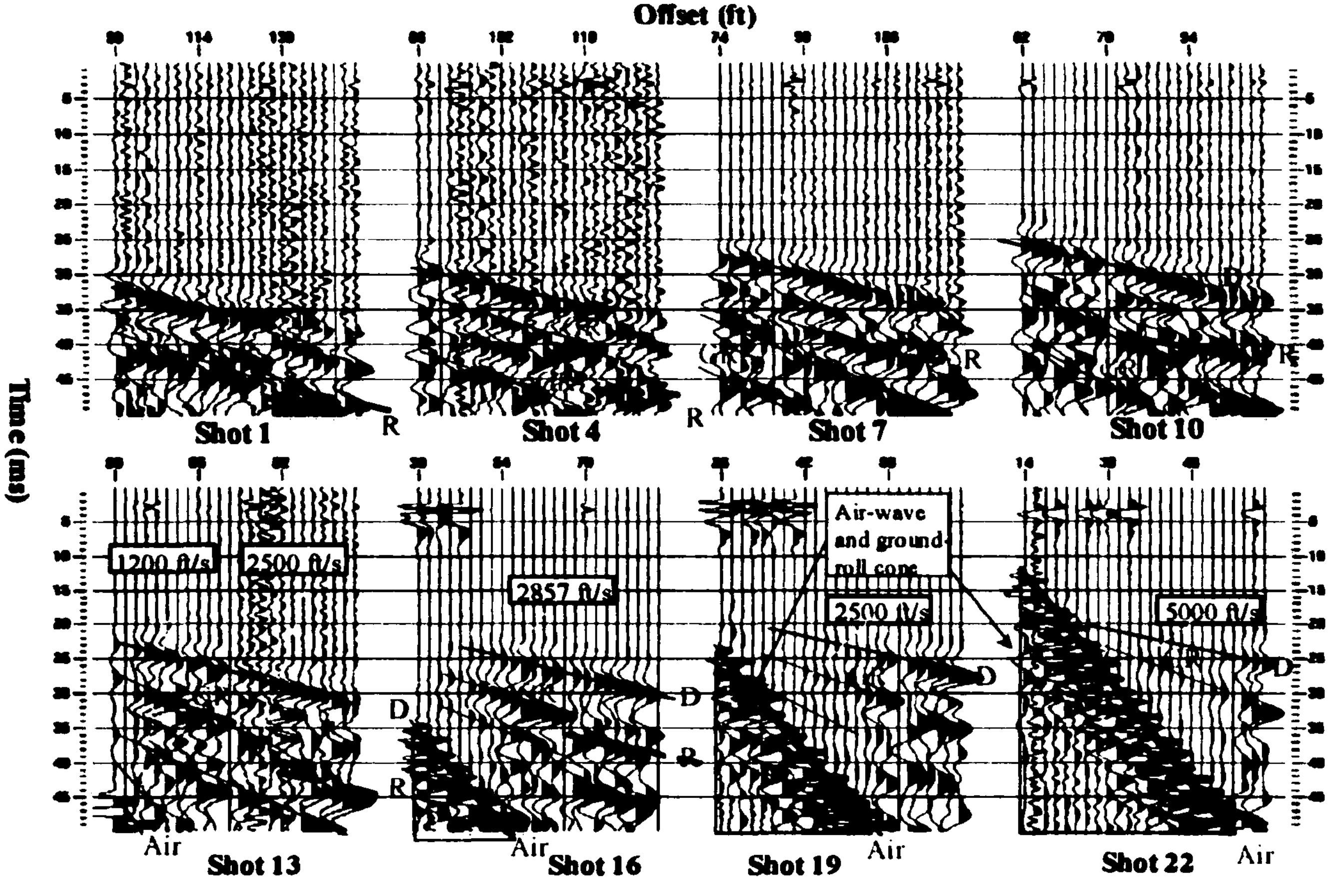

Figure 12 Interpretation of events for the unfiltered field data shot gathers of the ESP Line. Refraction (red lines, 'D') is interpreted with shortest arrival time and linear trend. Air-wave (blue lines, 'Air') is interpreted with its typical velocity of 1100 ft/s. Ground-roll (green lines, 'GR') is interpreted with its linear trend, lack of curvature and slow apparent velocity. Only one possible reflection event (purple, 'R') is interpreted in the shot gathers.

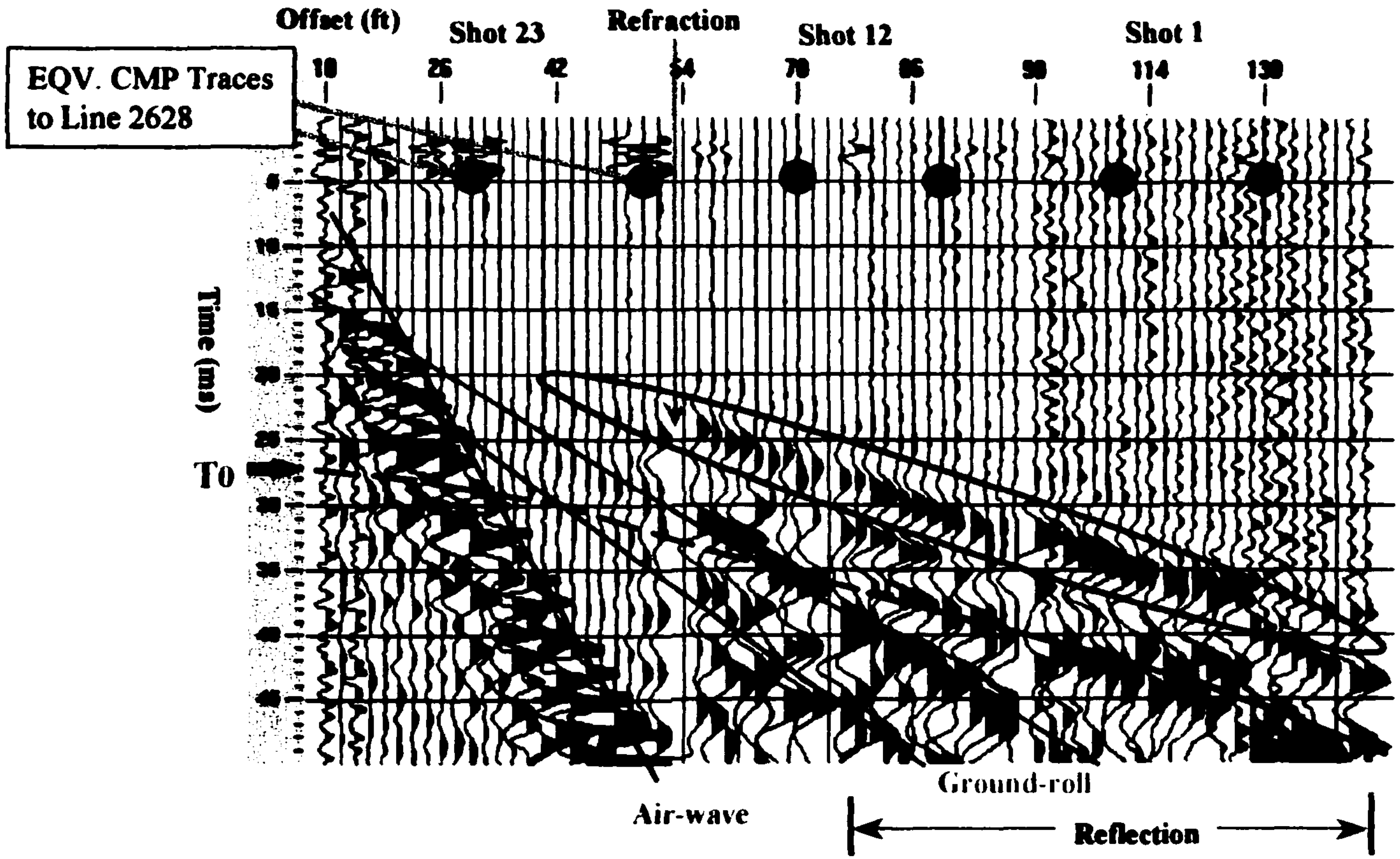

Figure 13 Composite walk-away display formed by juxtaposing three shot gathers so that they appear as one shot gather with continuous offsets having a high density of traces and a large offset range. Event types (air-wave, ground-roll, reflection, and refraction) become a lot easier to recognize due to the much larger offset range. Air-wave, ground-roll, and direct arrival (refraction) dominate the composite walk-away. The reflection (solid purple line) is within offset range 70--145 ft while the dashed purple line projects the two-way zero-offset traveltime (T0) to be approximately 27 ms. The green dots show the equivalent CMP traces for Line 2628 as if it were for the same survey geometry for Line 2628. Merely 3 valid traces would be in the equivalent CMP gather, because the other 3 traces are in the air-wave and ground-roll interference. Thus much finer trace spacing in the far offsets are advantageous.

CONCLUSIONS AND RECOMMENDATIONS

Because the geological targets of the K-25 Site are of sufficient depth (0–1800 ft) and there are enough traces for reflections in the far offsets, there is no problem obtaining interpretable stacked sections. However, it has been shown that special processing techniques, including Vibroseis whitening, refraction statics, and Continuous Spectral Balancing, are important techniques that have made significant improvements to the quality of the stacked sections. These special techniques are recommended for near-surface seismic reflection data processing. Kirchhoff prestack depth migration is important to obtain the structural images in the depth domain, because the geological structures are more reliably interpreted, and, therefore, better decisions for waste monitoring and remediation can be made. Iterative and prestack migration velocity analysis based on the data itself is a reliable technique to obtain migration velocities. Prestack depth migration could be a time-consuming process because the migration velocity updating procedure requires multiple partial and/or full prestack depth migration. However, the effort is worthwhile and significant for important geological and environmental targets such as the K-25 Site.

Because the seismic reflection data for the Gypsy Outcrop Site (Chapter 2) is very noisy, the various filtering methods used in conventional petroleum exploration cannot contribute significant improvement to the S/N ratio of the shot gathers of both the CMP Line 2628 and the ESP Line. Therefore, it is impossible to obtain a meaningful CMP stack, or most likely, to process the data further using prestack partial migration (DMO).

The seismic modeling of the ESP Line was not successful either, because the velocities from the outcrop velocity measurements are too slow and thus implausible. The interpretation of events in the shot gathers of the ESP Line showed that the near-offset shot gathers are in serious interference from air-wave and ground-roll noise and that the far-offset shot gathers have less serious interference. Therefore large offsets should be used in the seismic reflection surveys. The composite walk-away display convincingly illustrated that only one reflection event exists in the large offsets. This reflection event is approximately at the boundary between the bottom of the Gypsy Sandstone and the Tallant Marine Sandstone. Therefore the shallow Gypsy Stratigraphy is seismically indistinct.

For situations similar to the Gypsy Outcrop Site, it is recommended that a walk-away noise test be completed before the actual acquisition of the reflection data. The following new survey parameters are recommended for improved seismic reflection surveys similar to the Gypsy Outcrop Site: smaller receiver spacing (2 ft); more receiver channels (96); smaller shot spacing (2 ft); larger minimum offset (> 70 ft). This will enable seeing possible reflection events on a sufficient number of traces especially in the far offsets, where reflections exist and are relative free from noise interference. This is also important to produce a sufficiently high stacking fold to overcome noise.

The Continuous Spectral Balancing (Appendix A) is an effective technique to suppress reverberative noise and/or ground-roll, such as for the K-25 data sets. It is to some extent effective for the Gypsy Line 2628 and the ESP line, but because the data sets are much noisier and the fold is much lower than the K-25 data sets, the benefit is not so obvious.

For strong linear coherent noise, the Continuous Spectral Balancing is not going to be effective. More robust noise filtering techniques, such as the Local Slant-Sum Adaptive Noise Removal (Appendix B), are recommended. When both strong linear coherent noise and reverberative noise exists, it is recommended to apply Continuous Spectral Balancing before applying Local Slant-Sum Adaptive Noise Removal. There is trade-off in using either of the filtering algorithms. The Continuous Spectral Balancing is highly automatic, requiring only a few input parameters and can be applied in batch mode. Thus it is economic in data processing time and user interaction. But it cannot separate noise from signal when there is little spectral difference. On the other hand, the Local Slant-Sum Adaptive Noise Removal is highly interactive and adaptive to remove linear coherent noise. But it is a time-consuming and thus expensive process, requiring graphically picking events and time windows. More automatic picking of events and time windows should be implemented to substantially reduce user-interactions and hence processing time.

In summary, the data processing of the Gypsy Outcrop Site data sets and the Oak Ridge K-25 data sets shows that field data acquisition and S/N ratio are important factors affecting the success of the seismic reflection method for near-surface problems. If the seismic survey has insufficient fold and the data have serious noise interference, as is true for the Gypsy data sets, then data processing can not improve the situation. In contrast, if the seismic survey has enough fold and signal is relatively separated from noise, at least in the far offsets, as is true for the Oak Ridge K-25 data sets, then conventional data processing will not be a problem and special data processing will further improve results.

REFERENCES

1. O. Yilmaz, 1991, Seismic Data Processing, Society of Exploration Geophysicists.

2. R. E. Sheriff, 1991, Encyclopedic Dictionary of Exploration Geophysics, Third Edition: Society of Exploration Geophysicists.

3. J. A. Hunter, S. E. Pullan, R. A. Burns, R. M. Gagne, and R. L. Good, 1984, Shallow seismic reflection mapping of the overburden-bedrock interface with the engineering seismograph—Some simple techniques: Geophysics, Vol. 49, No. 8, 1381-1385.

4. H. R. Burger, 1992, Exploration Geophysics of the Shallow Subsurface: Prentice Hall: 182-187.

5. Z. H. Deng, 1996, Master's Thesis: University of Oklahoma.

6. J. D. Doyle, M. L. Sweet, K. K. Thomas, E. M. Gustason, 1992, Geological characterization of the IRD Gypsy Study Sites: BP Exploration, Report No. HO920072.

7. J. D. Doyle, M. L. Sweet, 1995, Three-dimensional distribution of lithofacies, bounding surfaces, porosity, and permeability in a fluvial sandstone—Gypsy Sandstone of Northern Oklahoma: AAPG Bulletin Vol. 70, No. 1, 70-80.

8. S. Danbom, 1995, Field notes for the Gypsy Seismic Reflection Expanding Spread Profile, unpublished observer's data sheet.

9. D. W. Steeples, A. G. Green, Thomas V. McEvilly, R. D. Miller, W. E. Doll, J. W. Rector, 1997, A workshop examination of shallow seismic reflection surveying: The Leading Edge, Vol. 16, No. 11, 1641-1647.

10. R. D. Miller, and J. Xia, 1997, Delineating paleochannels using shallow seismic reflection: The Leading Edge, Vol. 16, No. 11, 1671-1674.

11. Zhi-Ming Liu, William E. Doll, 1997, Seismic Reflection Processing for Characterization of a Waste Site: Proceedings of the Symposium on the Application of Geophysics to Engineering and Environmental Problems. SAGEEP'97, Vol. I, 291-299.

12. W. E. Doll, R. D. Miller, and J. Xia, 1998, A noninvasive shallow seismic source comparison on the Oak Ridge Reservation, Tennessee: Geophysics, Vol. 63, No. 4.

13. D. W., Steeples, B. Macy, C. Schmeissner, and R. Miller, 1995, Contrasting near-surface and classical seismology: The Leading Edge, 14, No. 04, 271-272.

14. T. M. Kolich, 1974, Seismic reflection and refraction studies in the Folded Valley and Ridge Province at Price Mountain, Montegomery County, Virginia: Master's Thesis, Virginia Poly-Tech Institute.

15. D. W. Ratcliff, Matthew A. Brzostowski, 1997, A practical approach to seismic imaging of complex geology: SEG Continuing Education.

16. J. Zhu, L. R. Lines, and S. Gray, 1998, Smiles and frowns in migration/velocity analysis: Geophysics, Vol. 63, No. 4.

17. J. Zhu and L. R. Lines, 1998, Comparison of Kirchhoff and reverse-time migration methods with applications to prestack depth imaging of complex structures: Geophysics, Vol. 63, No. 4.

18. W. E. Doll, R. D. Miller, and J. H. Xia, 1996, Enhancement of reflection data at a waste site: [Exp. Abs.] Soc. Explor. Geophys., 877-879.

19. C. Coruh and J. K. Costain, 1983, Noise attenuation by vibroseis whitening (VSW) processing: Geophysics, Vol. 48, No. 5, 543-554.

20. W. E. Doll and C. Coruh, 1995, Spectral whitening of impulsive and swept-source shallow seismic data. [Exp. Abs.] Soc. Explor. Geophys., 398-401.

21. W. E. Doll, R.D. Miller, and J. H. Xia, 1994, Non-invasive shallow seismic source comparison for hazardous waste site investigations. [Exp. Abs.] Soc. Explor. Geophys., 591-594.

22. M. T. Taner, D. E. Wagner, E. Baysal, and L. Lu, 1994. A unified method for 2-D and 3-D refraction statics. Submitted to Geophysics for publication.

23. P. J. Lemiszki, 1994, Geological mapping of the Oak Ridge K-25 Site, Oak Ridge, Tennessee, K-25 Environmental Restoration Program Report K/ER-111.

24. P. J. Lemiszki, 1999, Personal communication.

25. R. Weindell, 1997, Personal communication.

26. C. Stork, 1994, Demonstration of MVA tomography with controls and constraints for determining an accurate velocity model for prestack depth migration: 64th Annual Internat. Mtg., Soc. Expl. Geophys., Expanded Abstracts, 1338-1342.

27. C. Stork, and R. W. Clayton, 1991, An implementation of tomographic velocity analysis: Geophysics, 56, No. 04, 483-495.

28. C. Stork, and R. W. Clayton, 1989, Need for constraints in generalized prestack velocity analysis: 59th Annual Internat. Mtg., Soc. Expl. Geophys., Expanded Abstracts, 1221.

29. G. A. McMechan, H. Chang, J. P. VanDyke, M. Solano, and D. Epili, 1998, 3-D prestack Kirchhoff depth migration: From prototype to production in a massively parallel processor environment: Geophysics, Vol. 63, No. 2, 546-556.

30. L. Pasasa, F. Wenzel, and P. Zhao, 1998, Prestack Kirchhoff depth migration of shallow seismic data: Geophysics, Vol. 63, No. 4, 1241-1247.

31. F. Z. Wang, 1994, Characterization in three dimensions of a low-velocity layer using crosswell seismic travel times, MS Thesis, University of Oklahoma, p. 34-81.

32. F. E. Akbar, P. L. Stoffa, and M. K. Sen, 1998, Three-dimensional plane-wave Kirchhoff depth migration: 68th Annual Internat. Mtg., Soc. Expl. Geophys., Expanded Abstracts, 1708-1711.

APPENDIX A CONTINUOUS SPECTRAL BALANCING

INTRODUCTION

J. P. Lindsey and others at GX Technology originally developed the Continuous Spectral Balancing algorithm. It was shown that the algorithm had been successfully applied to petroleum exploration data sets to solve ground-roll noise problems (Lindsey, 1997, personal communications).

Lindsey kindly granted permission to write the code of the continuous spectral balancing algorithm, based on his descriptions of the algorithm, and to run it in the Shell Crustal Imaging Facility (SCIF) at the University of Oklahoma.

The principle of the algorithm will be explained in mathematical detail. The FORTRAN 77 code has been written and tested by myself. This represents a new application that is different from the original use on petroleum exploration data. The suitability of the algorithm for the new application in the near-surface seismic exploration for environmental and engineering purposes will be investigated both through synthetic data traces and through near-surface seismic reflection data from Oak Ridge K-25 Site and Gypsy Outcrop Site.

MASKING FUNCTIONS AND SUBCHANNELS

Some basic concepts and mathematics need to be introduced before getting into the details of the algorithm itself.

Masking functions multiply the frequency spectrum of the input trace. The Inverse Fourier Transform of the product gives band-limited traces. These traces in turn will be weighted to produce a spectrally-balanced output trace.

Figure 1 shows typical masking functions. The curve marked by triangular dots is one of the masking functions. All other masking functions look exactly like this one except shifted on the frequency axis. These masking functions are overlapping. The summation of all the masking functions is shown as the circular dotted curve.

A subchannel is defined as a band-limited trace corresponding to one of the masking functions. It is obtained by first multiplying the input trace's frequency spectrum with one of the masking functions, then taking the Inverse Fourier Transform of the product.

The bandwidth of each subchannel is defined as frequency distance between the half-amplitude points in the masking function. From Figure 1 it is seen that the bandwidth of each subchannel is the same as the subchannel frequency spacing. They can be calculated with the formula:

$$W = \frac{f_U - f_L}{N_C} \quad (1)$$

where f_L is lower cutoff frequency; f_U is upper cutoff frequency. Note that f_L and f_U are defined at the half-amplitude points also. N_C is the number of subchannels. Given these parameters, the masking functions can be calculated using formula

$$f_C = f_L + W/2 + (n-1) \times W \quad (2)$$

$$M_n(f) = \begin{cases} \cos^2((f - f_C)/(2 \times W)) & \text{if } |f - f_C| \le W \\ 0 & \text{otherwise} \end{cases} \quad (3)$$

where f is frequency; f_C is the center frequency of the masking function; n represents the n-th subchannel; $M_n(f)$ is the masking function for the n-th subchannel, $n=1\sim N_C$.

Figure 1 shows a particular case with f_L=30 Hz, and f_U = 150 Hz, and N_C=6. Note that the summation of all masking functions results in a flat spectrum from f_L to f_U, with either ends being half of a cosine-squared, bell-shaped ramp. Thus, according to the linearity and stacking property of Fourier Transform, the summation of all the subchannels without any further processing will be equivalent to doing a band-pass filtering with the dotted curve as the filter spectrum. However, in the continuous spectral balancing algorithm, these subchannels will not be simply summed; but rather, they will be used to dynamically evaluate the relative strength of each subchannel at any instantaneous time and weighted toward the output trace, resulting in a balanced summation as output.

HILBERT TRANSFORM AND ENVELOPE OF SEISMIC TRACE

As mentioned above, the relative strength of each subchannel will be evaluated and weighted toward the output trace. First is to calculate the envelopes of all the subchannels. Second is to calculate the modulation functions, which will be used as weighting factors for the subchannel traces toward the output trace.

This part of the text provides mathematical basis of how to calculate the envelope of a seismic trace. Assume that there is a seismic trace x(t), which is a real and continuous function of time variable t. The Hilbert Transform of x(t) is defined as

$$y(t) = h(t) * x(t) = \frac{1}{\pi t} * x(t) \tag{4}$$

where * denotes convolution; $h(t) = \frac{1}{\pi t}$ is called the Hilbert Operator; x(t) and y(t) together constitute a complex trace,

$$z(t) = x(t) + iy(t) \tag{5}$$

where i is the imaginary number, $i = \sqrt{-1}$.

Because of (5), the seismic trace x(t) is also called a real trace, the Hilbert Transform y(t) is also called an imaginary trace, and the z(t) is called a complex trace.

The envelope E(t) is calculated as:

$$E(t) = \sqrt{x^2(t) + y^2(t)} \tag{6}$$

The rest of the text involves the derivation and the efficient calculation of the envelope in the Fourier Transform Domain instead of using the less efficient mathematical formula (4) in the time domain.

Let Y(f) be the Fourier Transform of y(t); X(f) of x(t); H(f) of h(t). Taking Fourier Transforms on either sides of (4) gives

$$Y(f) = H(f) \times X(f) = \int_{-\infty}^{+\infty} h(t) e^{-2\pi f t} dt \times \int_{-\infty}^{+\infty} x(t) e^{-2\pi f t} dt \qquad (7)$$

And $$H(f) = \int_{-\infty}^{+\infty} h(t) e^{-2\pi f t} dt = \int_{-\infty}^{+\infty} \frac{1}{\pi t} e^{-2\pi f t} dt = \begin{cases} i & if \quad f \geq 0 \\ -i & if \quad f < 0 \end{cases} \qquad (8)$$

The Hilbert Transform, y(t), is obtained by taking the inverse Fourier Transform of Y(f):

$$y(t) = \int_{-\infty}^{+\infty} Y(f) e^{-2\pi f t} df = \int_{-\infty}^{+\infty} H(f) X(f) e^{-2\pi f t} df \qquad (9)$$

Therefore, to obtain the Hilbert Transform of a trace x(t), an equivalent method is first to do the Fourier Transform X(f), then to multiply it with H(f), then to do the Inverse Fourier Transform of the product Y(f).

In formulae (7)–(9), only one Forward Fourier Transform of x(t), one multiplication of H(f) with X(f), and one Inverse Fourier Transform are involved to calculate the Hilbert

Transform of a seismic trace. The total computation is of order $O(N \log_2(N))$. Here N is the number of samples per trace to perform Fourier Transforms. Therefore calculating the Hilbert Transform in the Fourier Transform Domain is much faster than from the mathematical convolution formula (4) directly in the time domain, which involves multiplication and summation at every time sample:

$$y(t) = \sum_{\tau=0}^{t} \frac{1}{\pi\tau} x(t-\tau) \tag{10}$$

The total computation of (10) is of order $O(N^2)$.

CONTINUOUS SPECTRAL BALANCING ALGORITHM

It is time now to talk about the algorithm itself because all the basic concepts have been introduced. Figure 2 is a simplified data flow chart as it goes from an input data trace to a spectrally balanced output data trace.

Step 1: Rectangular Fast Fourier Transform

The input trace is subjected to a rectangular Fast Fourier Transform (FFT). If it is not a binary number of samples in length (such as 512, 1024, 2048, etc.), zeros are padded to its end to make it so. The rectangular transform is the first form of an FFT output, where the cosine transform and the sine transform results are separate. These are called the "Real" and "Imaginary" parts of the output frequency spectrum.

$$X(f)=\int_{-\infty}^{+\infty}x(t)e^{i2\pi ft}dt=\int_{-\infty}^{+\infty}x(t)\cos(2\pi ft)\cdot dt+i\int_{-\infty}^{+\infty}x(t)\sin(2\pi ft)\cdot dt$$
$$=\mathrm{Real}(\int_{-\infty}^{+\infty}x(t)e^{i2\pi ft}dt)+i\,\mathrm{Imag}(\int_{-\infty}^{+\infty}x(t)e^{i2\pi ft}dt) \quad (11)$$

where i is an imaginary number, $i=\sqrt{-1}$; Real denotes "real part"; Imag denotes "imaginary part".

Step 2: Frequency Masking and Inverse Transformation

Masking functions and subchannels were introduced in the previous section, titled "masking functions and subchannels". A "masking" function is used to multiply the values of both real and imaginary parts of the frequency spectrum of the input trace. Thus

$$MXn(f)=Mn(f)\times X(f)$$
$$=Mn(f)\times \mathrm{Real}(X(f))+iMn(f)\times \mathrm{Imag}(X(f)) \quad (12)$$

where $M_n(f)$ is the n-th masking function, n=1–Nc (Number of Subchannels). $MX_n(f)$ is the spectrum of the n-th subchannel. The "real trace", marked "Real" in Figure 2, is obtained by taking the Inverse Fourier Transform of $MX_n(f)$.

$$xn(t)=\int_{-\infty}^{+\infty}MXn(f)e^{2\pi ft}df \quad (13)$$

Hilbert Transform (introduced in the section titled "Hilbert transform and envelope of seismic trace") is used to calculate the envelope of a subchannel. The Hilbert Transform of a trace is called the "Imaginary Trace", marked "Imag" in Figure 2. Based on (7)–(9), multiplying the subchannel spectrum, $MX_n(f)$, with the Hilbert Filter H(f) gives:

$$Yn(f) = H(f) \times XMn(f) \tag{14}$$

where $Y_n(f)$ is the spectrum of the imaginary trace. Recall formula (8),

$$H(f) = \begin{cases} i & if(f \geq 0) \\ -i & if(f < 0) \end{cases} \tag{15}$$

The Inverse Fourier Transform of Y(f) gives the imaginary trace:

$$yn(t) = \int_{-\infty}^{+\infty} Yn(f)e^{2\pi ft}\, df \tag{16}$$

Note that in Figure 2 there are links to other subchannels, which work exactly the same way as the current n-th subchannel.

Step 3: Processor

The box labeled "Processor" in Figure 2 is a complicated process. It will be explained in detail later. The processor calculates a modulation function for each subchannel based on the envelopes of all subchannels. The modulation function is multiplied with the subchannel trace to contribute toward the output. It is the modulation function that makes the continuous spectral balancing take effect.

Step 4: Sum

The sum of all the modulated subchannels results in the output trace. This will be explained at the end of the next section.

PROCESSOR DIAGRAM

The processor calculates a modulation function to multiply with the subchannel trace. Figure 3 is the processor diagram that explains the processor box in Figure 2. The real trace of the subchannel is passed directly to the "Modulation" box, where the input real trace (n-th subchannel) is multiplied with a modulator, $M_n(t)$. The rest of the diagram involves the calculation of the modulator $M_n(t)$.

Envelope Calculation

In the box labeled "Calculate Envelope", the real trace $x_n(t)$ and the imaginary trace $y_n(t)$ are used to calculate envelope of the n-th subchannel:

$$E_n(t) = \sqrt{x_n^2(t) + y_n^2(t)} \tag{17}$$

Logic and Envelope Averaging

In the box labeled "Logic and Envelope Averaging", envelopes from all subchannels are examined for the maximum value for any fixed time. The corresponding subchannel envelope is excluded toward the calculation of the average envelope for any given time. This exclusion is based on the assumption that the maximum envelope corresponds to ground-roll, which normally has the maximum amplitude (energy) among all subchannels.

Thus
$$\bar{E}(t)=\left\{\sum_{n=1(\text{Subchannel})}^{Nc\,(\text{except}N\max)} E_n(t)\right\}\Big/(Nc-1) \tag{18}$$

where $\bar{E}(t)$ is the average envelope at any given time. N_{max} is the subchannel number with the maximum envelope at any given time t.

Division

In the box labeled "DIVISION", the average envelope, $\bar{E}(t)$, is used as a numerator toward the calculation of the modulator, $M_n(t)$. Whereas, the envelope for the n-th subchannel, $E_n(t)$, is used as a denominator. Thus the modulator is expressed as

$$M_n(t)=\frac{\bar{E}(t)}{E_n(t)} \tag{19}$$

Because $E_n(t)$ in (19) may have very small values causing the modulation function $M_n(t)$ unstable, either a small value needs to be added to the denominator $E_n(t)$, or else the quotient $M_n(t)$ has to be clipped at certain large value to ensure stability.

Thus formula (19) is modified as

$$M_n(t)=\frac{\bar{E}(t)}{E_n(t)+\varepsilon} \tag{20}$$

where ε is a small value.

Therefore, the final output of the continuous spectral balancing algorithm is expressed as

$$Z(t) = \sum_{n=1}^{Nc} M_n(t) \times \mathcal{X}_n(t) = \sum_{n=1}^{Nc} \frac{\bar{E}(t)}{En(t)+\varepsilon} \times \mathcal{X}_n(t) \quad (21)$$

Just as a reminder, Nc is the number of subchannels; $M_n(t)$ is the modulator for the n-th subchannel. $\mathcal{X}_n(t)$ is the trace signal of the n-th subchannel; En(t) is the envelope of of the n-th subchannel; $\overline{E}(t)$ is the average envelope of all subchannels except the subchannel with the maximum envelope at a given instaneous time t.

Formula (21) is the all-in-one summarizing formula of the continuous spectral balancing algorithm. According to (20) and (21), for ground-roll and air-wave noise having strong energy limited in a narrow frequency band, the modulation function $M_n(t)$ is going to be small because the denominator En(t) is going to be large; however, the numerator will remain small because the maximum envelope is excluded toward the calculation of the average envelope. Therefore the subchannel corresponding to narrow-band ground-roll and air-wave will be given a much smaller weighting factor toward the output trace.

Parameters for Input

The following are the major parameters to be specified for the algorithm:

(1) Nc --- Number of subchannels;

(2) f_L --- Lower cutoff frequency (Hz);

(3) f_U --- Upper cutoff frequency (Hz);

(4) ε --- Stability factor (a small value to avoid instability of modulation function).

Basically these parameters need to be experimented to find out the optimum parameter combination. The following are some general guidelines that might be helpful.

(1) N_C – The computation time will be approximately directly proportional to the Nc, since envelopes and weight factors are all computed based on subchannels. Thus the Nc can not be too large. Another reason is that when the Nc is too large, each subchannel will represent too narrow a frequency band, thus the subchannel traces may not be properly modulated toward the output. One more reason is that when the Nc is too large, the ramp of the lowest and the highest subchannel will be too steep, resulting in a problem similar to the sharp edge of a band-pass filter.

On the other hand, Nc can not be too small, because the channel with the maximum envelope at any fixed time will not be properly isolated from neighboring subchannels with reflection signals. Generally Nc can be chosen to be between 6 and 20. The best Nc may be the one that is capable of limiting the noise with maximum envelope in one subchannel.

(2) f_L and f_U – These can be chosen to allow the frequency band with reflections to be passed while rejecting high and low frequency components. There is no need to include the frequency bandwidth containing no reflections, just as in a band-pass filter.

(3) ε -- It should actually be a relative stability factor. The maximum absolute value in each seismic trace is searched, and then multiplied by ε to give the actual value to be put in the modulator part of equation (21). Pat Lindsey mentioned another method to substitute the small value of ε. That is to limit the maximum value of the modulators, with too-big modulators being clipped in the program. However, this latter method is not currently implemented. As a rule of thumb, ε can be something like 0.001 – 0.0001. If ε is too small, e.g., less than 10^{-6}, some unpredictable artifacts may result.

SYNTHETIC EXAMPLES

Synthetic traces are used to test the continuous spectral balancing algorithm. Figure 4 verifies Fourier Transform and Hilbert Transform using a sinusoid trace. Figure 4a is a synthetic trace with a 50 Hz sinusoid for the first 500 ms. The trace length of 500 ms is increased to 512 ms to make it a power of 2. For practical consideration to avoid wrap around noise problem (Yilmaz, 1991) associated with Fourier Transforms, the trace length is doubled into 1024 ms, padded with zero. The padding increases the cost in computations, but avoids the wraparound effects. Figure 4b and 4c are the real and the imaginary parts of the Fourier Transform. Figure 4d is the amplitude spectrum. Figure 4b–4d show that the large amplitude in the spectra corresponds with the frequency of the input trace, 50 Hz. The spectrum is not a spike at 50 Hz, however, because the trace is not a perfect sinusoid but rather, only the first 500 ms of the 1024 samples. The Hilbert Transform (Figure 4e) is an approximately 90 degree phase shift of the input trace (Figure

4a) and that the envelope (Figure 4f) is nearly flat (1.0). There are some vibrations in the envelope, however, especially at the end points of the unfiltered trace. To solve this problem, linear tapering can be applied to the input data trace (Figure 4a) before applying Fourier Transforms. The linear taper is (1, 40, 460, 500). Figure 4g shows the Hilbert Transform of the tapered trace. The tapering results in much weaker deviations from the ideal value 1.0 in the envelope for the interior samples (50 ms--450 ms) (Figure 4h). Therefore, input data had better be tapered (preconditioned) before continuous spectral balancing processing.

Figure 5 tests the continuous spectral balancing using a synthetic trace (Figure 5a) consisting of a zero-phase wavelet (75 Hz central frequency) convoluted with reflection coefficients ($R_{60\ ms}$=0.4, $R_{100\ ms}$=1.0, $R_{150\ ms}$=0.6, $R_{300\ ms}$=1.0, $R_{400\ ms}$=0.4). The amplitude spectrum of the entire trace (Figure 5c) is not as smooth as that of a single wavelet (Figure 5b). This is reasonable because the reflection coefficients and time shifts have effects on the spectrum of the trace. The Hilbert Transform of the trace (Figure 5d) shows a 90-degree phase shift in each of the individual wavelets in the unfiltered trace (Figure 5a). It is observed that taking twice the Hilbert Transform of the unfiltered trace will result in a trace that is a 180 degree shift, i.e., negative from the unfiltered trace. This is proof that the Hilbert Transform is performed correctly. Figure 5e shows the envelope of the entire trace (Figure 5a). Figure 5f is the spectrum of the spectrally balanced single wavelet corresponding to Figure 5b. It has a much flatter spectrum than that of the unfiltered single wavelet. This proves that continuous spectral balancing is taking effect. Figure 5g shows the spectrally balanced trace, which has narrower wavelet width than the unfiltered trace (Figure 5a). However, Figure 5g is much more ringy. The spectrum of the spectrally-balanced trace (Figure 5h) looks flatter than that of the unfiltered trace (Figure 5c) in that frequencies away from the central frequency have been boosted. Note that the non-smoothness (spikes) in the spectrum might be attributable to reflection coefficients and time delays in the trace, therefore it is reasonable.

Figure 6 shows the spectral balancing of a trace consisted of three sinusoids: $\sin(2\pi f_1 t) + 0.6 \sin(2\pi f_2 t) + 0.15 \sin(2\pi f_3 t)$, where f_1=30 Hz, f_2=70 Hz, f_3=100 Hz, t is time in seconds. Figure 6b is the amplitude spectrum. The 100 Hz sinusoid has much smaller amplitude than the other two sinusoids. The spectrally-balanced trace (Figure 6c) shows different waveforms from the unfiltered trace, because the weaker frequency components have been boosted (Figure 6d). However, the interior part (50–450 ms) of Figure 6c has smaller amplitude than both ends. This is a problem caused by no tapering. Taking a tapering (1, 40, 460, 500) ms of the input trace, the spectrally-balanced trace (Figure 6e) has smaller artificial amplitude jumps at the ends. The amplitude spectrum (Figure 6f) shows similar amplitude contrast among the three frequency components, (30, 70, 100) Hz.

Figure 7 shows the continuous spectral balancing with a synthetic shot gather. The synthetic shot gather has the same survey parameter setting as that of the Gypsy Reflection Line 26-28. These include: minimum offset (30 ft), maximum offset (145 ft), receiver spacing (5 ft), time sampling interval (0.1 ms), record length (100 ms). Because the reflection event and the linear coherent noise have the same spectra, the continuous spectral balancing will not work.

Figure 7a is the synthetic shot gather consisted of a reflection event and a linear coherent noise (air-wave), both generated using the same zero-phase wavelet:

$$\exp(-\alpha\,(2\pi ft)^2)\cos(2\pi ft),$$

within time duration of $(-T_L/2, T_L/2)$; where $\alpha = 0.08$, $f=75$ Hz, $T_L = 3T$, $T=1/f$; t= time; T= dominant period. Figure 7b is the average amplitude spectrum of the entire shot gather (Figure 7a). Figure 7c is the spectrum of the data inside the window in Figure 7a. Figure 7c is the shot gather after continuous spectral balancing using filter parameters: $N_C=10$, $\varepsilon=0.001$, $F_L=10$ Hz, $F_U=200$ Hz. The waveforms for both the reflection event and the linear coherent noise look the same. Figure 7d is the shot gather after applying continuous spectral balancing to (a). The central peaks of the waveforms look narrower than in the unfiltered shot gather (Figure 7a). However, undesirable side lobes have resulted for both the reflection event and the linear coherent noise. Figure 7d illustrates that when there is little spectral difference between reflection events and linear coherent noise, continuous spectral balancing will fail to suppress noise and improve reflections. Figure 7e shows the amplitude spectrum of the entire shot gather (Figure 7d). Compared with the spectrum of the unfiltered shot gather (Figure 7b), Figure 7e shows flatterer spectrum. Figure 7f shows the spectrum of the data inside the window in Figure 7d. Figures 7c and Figure 7f are analogous to the spectra of the single wavelet in Figure 5b and Figure 5f. Even though flatterer spectra have been resulted, the effectiveness of the continuous spectral balancing cannot be judged from the spectra alone, as has been illustrated in Figure 7d, where the character of the resulted waveforms are more useful measure of the effectiveness of the filtering. In summary, continuous spectral balancing should not be applied unless there is enough spectral differences between reflection signals and linear coherent noise modes.

CONTINUOUS SPECTRAL BALANCING OF REAL DATA

Continuous spectral balancing has been applied to both Oak Ridge K25 Line I (Chapter 1) and the Gypsy Line 2628 (Chapter 1). The following shows the results for the shot gathers of the two sites.

Oak Ridge K-25 Line I

A continuous spectral balancing filter having the following parameters was applied to the shot gathers of Oak Ridge K-25 Line I: Number of subchannels (10), Lower cutoff frequency (20 Hz), Higher cutoff frequency (150 Hz), Relative stability factor (0.0001).

Figure 8 and Figure 9 show a comparison of shot gathers before and after the above filtering. Figure 8 includes five VSW correlated shot gathers. Figure 9 includes the corresponding shot gathers after notch and band-pass filtering, and continuous spectral balancing. In Figure 8, the reverberative noise is prominent in shot gathers 1022, 1025, 1100 and 1101 (e.g., ellipses in Figure 8); while in Figure 9, the reverberative noise is substantially reduced and it is a lot easier to see reflections. In Figure 8, the 60 Hz noise dominant the far offsets of shot gather 1311, so it is almost impossible to see reflections deeper than 200 ms in the far offsets of shot gather 1311. In Figure 9, the 60 Hz noise is removed and the reflections can be seen more clearly.

In summary, the notch and band-pass filtering, and the continuous spectral balancing have substantially reduced the reverberative noise and the 60 Hz noise, greatly improving the signal-to-noise ratio of the shot gathers of the Oak Ridge K-25 Line I.

Gypsy CMP Line 2628

Figure 10 shows unfiltered shot gathers 1-12. Air-wave (blue lines) is strong in some of the shot gathers (e.g., 1, 8, 9, 10, 12). Both air-wave and ground-roll exist inside the air-wave and ground-roll cone, so it is hard to see any reflections inside the air-wave and ground-roll cone. Ground-roll (green lines) exists also beyond the air-wave and ground-roll cone. There are ringing or parallel events (ellipses in Figure 10). Due to these noise problems, it is very hard to see the possible reflections – they do not cross enough traces.

The continuous spectral balancing has been applied to the shot gathers of Line 2628, with the following parameters: Number of subchannels (10), Lower cutoff frequency (15 Hz), Higher cutoff frequency (315 Hz), Relative stability factor (0.001).

Figure 11 shows the continuous spectral balancing of Line 2628. It has higher time resolution and much less ringing than Figure 10 due to the whitening of the frequency spectra. It is easier to interpret the possible reflections (purple lines) and they have better lateral continuity and/or wider span of traces. The amplitude of the air-wave is reduced. The apparent frequency of the air-wave also becomes lower. However, the air-wave and the ground-roll noise are still apparent and strong in these shot gathers. Nevertheless, the resultant shot gathers (Figure 11) of the continuous spectral balancing are better than those of the band-pass filtering of the shot gathers of the Gypsy Outcrop Site, with higher time resolution, less ringing and wider reflection span. Continuous spectral balancing should be used as the filtering option for the Gypsy Reflection Line 2628.

CONCLUSIONS

The continuous spectral balancing is a useful filtering technique to remove the reverberative and ringing noise present in shot gathers. The substantial improvement of S/N ratio of the shot gathers, as shown in the sample shot gathers of the Oak Ridge K-25 Line I, will bring in improved S/N ratio for seismic imaging such as CMP stacking and migration. The shot gathers of the Gypsy Outcrop Site have been improved to some extent. Therefore, the continuous spectral balancing is a useful filtering (time processing) method to deal with noise problems in a trace-by-trace fashion.

However, in both Oak Ridge K-25 Line I and Gypsy Reflection Line 2628, the signal-to-noise ratio, in the linear-coherent noise dominated areas, such as along the air-wave trend, inside the air-wave and ground-roll cone, and along the ground-roll trend, cannot be improved significantly. In such cases, apparent velocity and/or slope based methods, such as Local Slant-Sum Adaptive Noise Removal (Appendix B) and local tau-p methods, do not require differences in frequency spectra and would therefore be more useful.

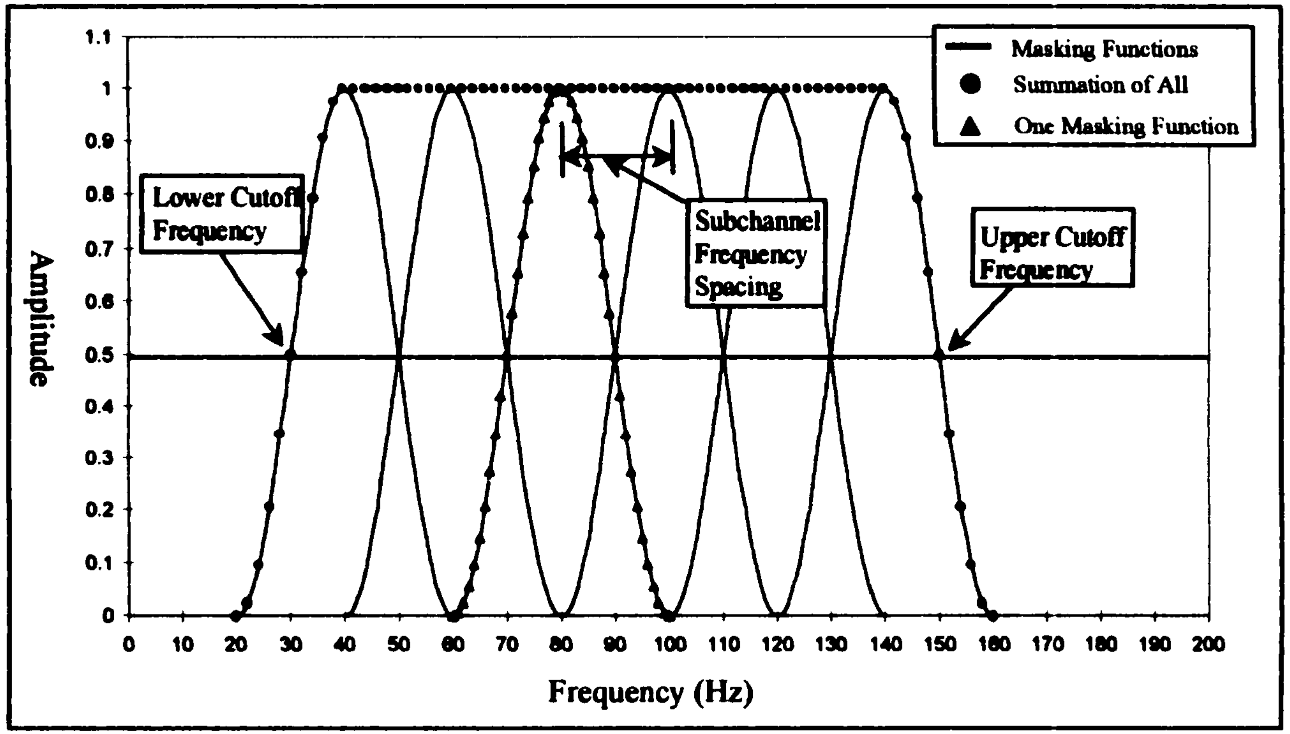

Figure 1 Typical masking functions. Each masking function is a bell-shaped, cosine-squared function. One of the masking functions is marked by triangular dots. The summation of all masking functions is marked by round dots. (Modified from Pat Lindsey, 1997, personal communications).

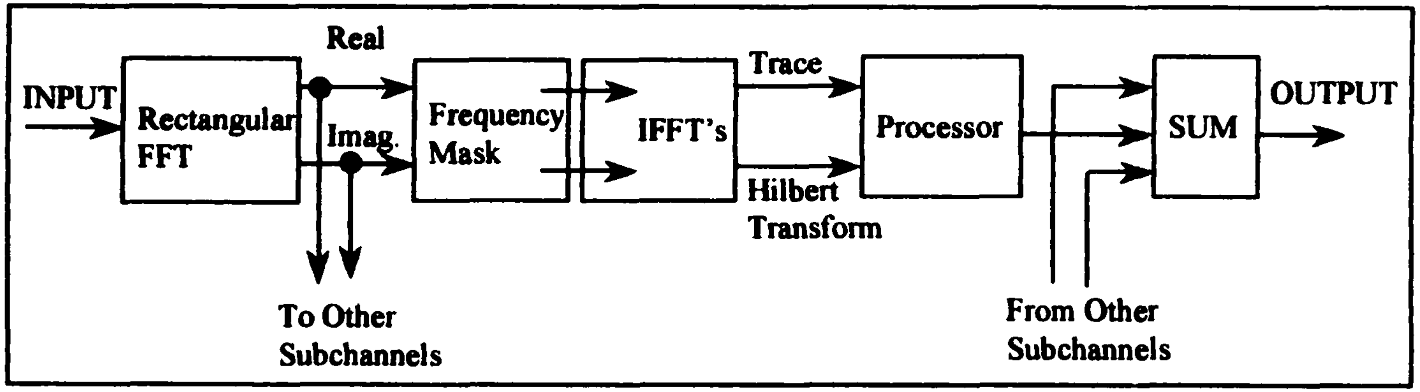

Figure 2 Main-flow diagram of the continuous spectral balancing algorithm. (Modified from Pat Lindsey, 1997, personal communications).

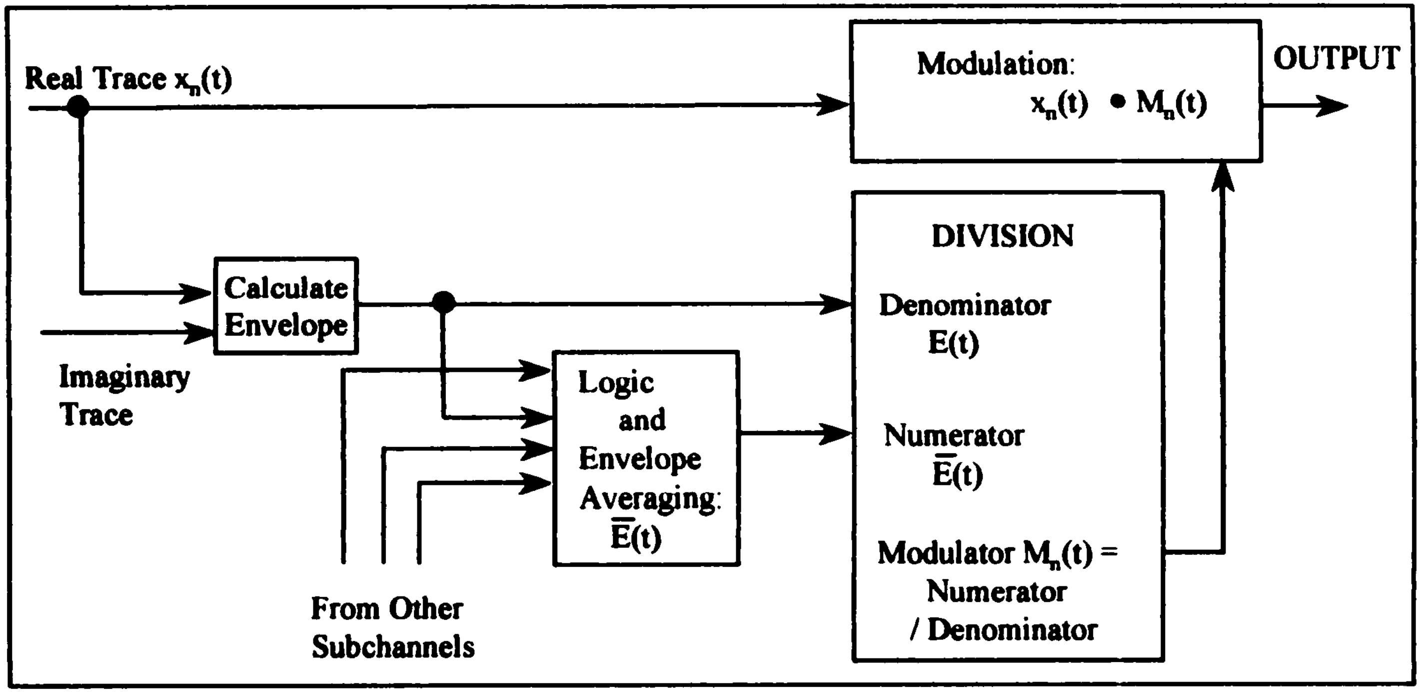

Figure 3 Processor diagram of signal flow and mathematical operations for the n-th subchannel. (Modified from Pat Lindsey, 1997, personal communications).

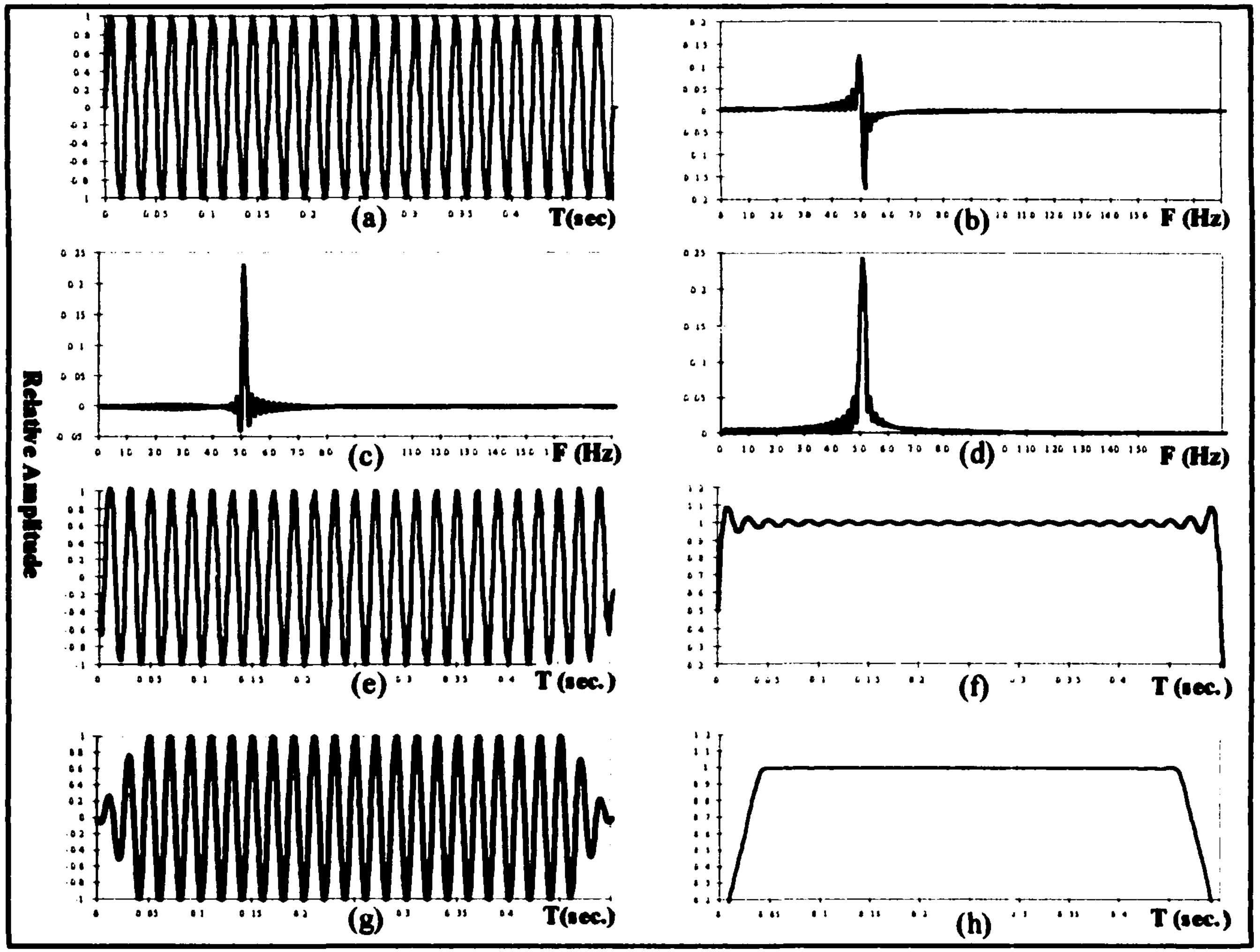

Figure 4 Verification of Fourier Transform and Hilbert Transform. (a) Data trace of a single sinusoid (50 Hz, 500 ms); (b) Real part of FFT of (a); (c) Imaginary part of FFT of (a); (d) Amplitude spectrum of (a); (e) Hilbert transform of (a); (f) Envelope of (a); (g) Hilbert transform of the trace linearly tapered at both ends; (h) Envelope of the linearly tapered trace.

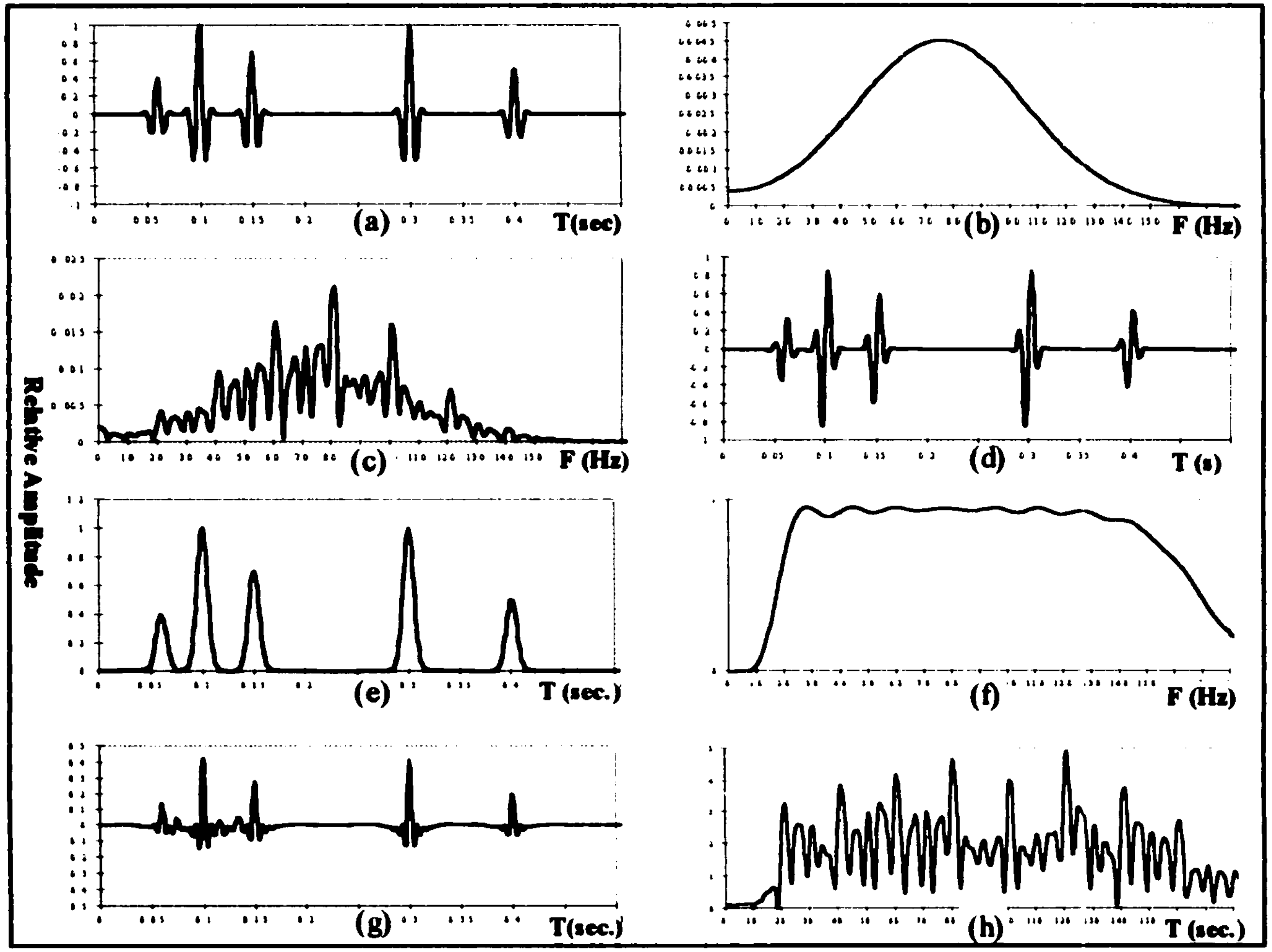

Figure 5 Verification of Fourier Transform and Hilbert Transform with zero phase wavelets. (a) Synthetic trace with a zero phase wavelet convoluted with reflection coefficients. (b) Amplitude spectrum of the single wavelet at 150 ms; (c) Amplitude spectrum of the synthetic trace; (d) Hilbert Transform of trace; (e) Envelope of trace; (f) Amplitude spectrum of the balanced single wavelet that corresponds to (b). (g) Continuous spectral balanced trace. (h) Amplitude spectrum of the balanced trace.

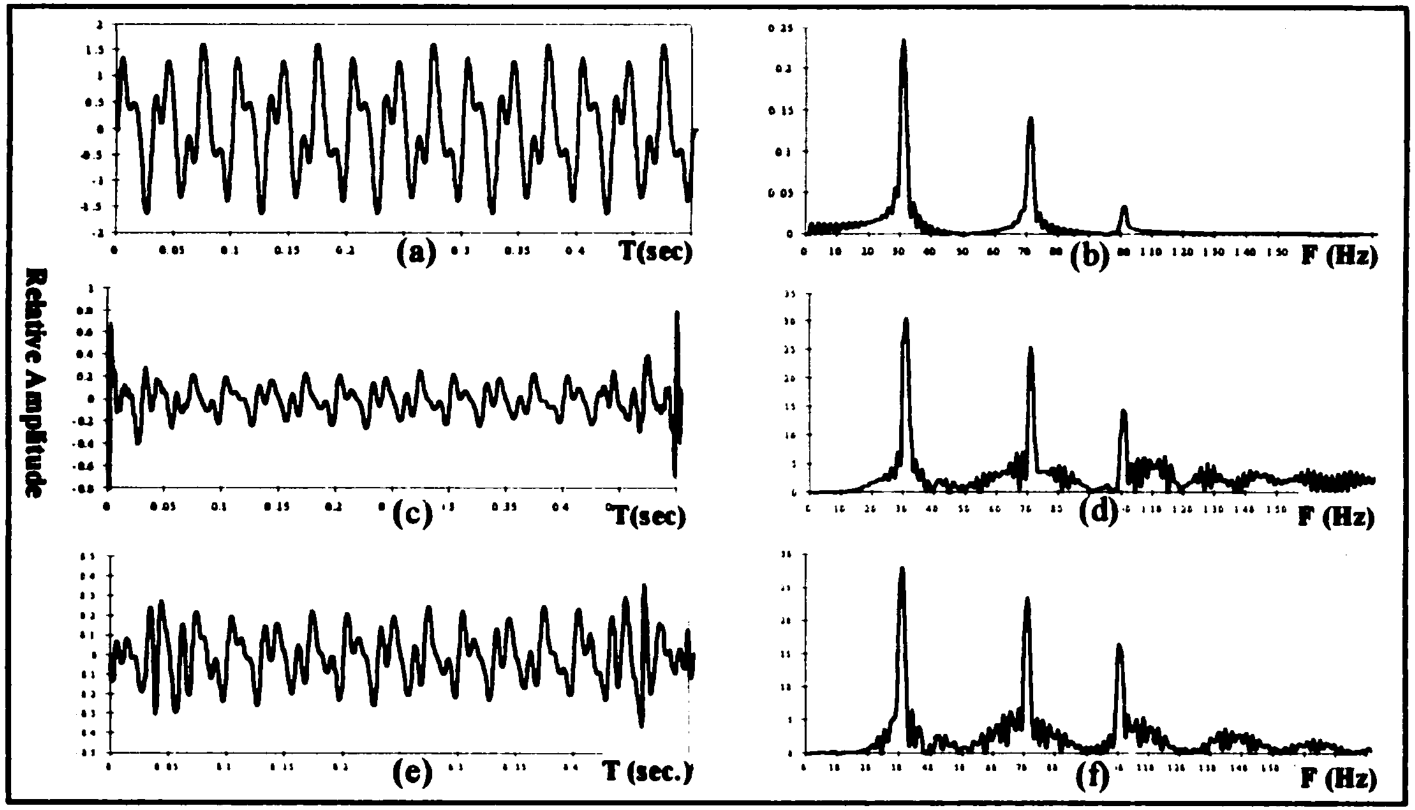

Figure 6 Continuous spectral balancing of synthetic data. (a) A trace consisted of three sinusoids of 30, 70, and 100 Hz, and amplitudes 1.0, 0.70, 0.15, respectively. (b) Amplitude spectrum of trace; (c) Continuous spectral balanced trace; (d) Amplitude spectrum of spectral balanced trace. (e) Continuous spectral balanced of the tapered trace, with a tapering of (1, 40, 460, 500) ms; (f) Amplitude spectrum of (e).

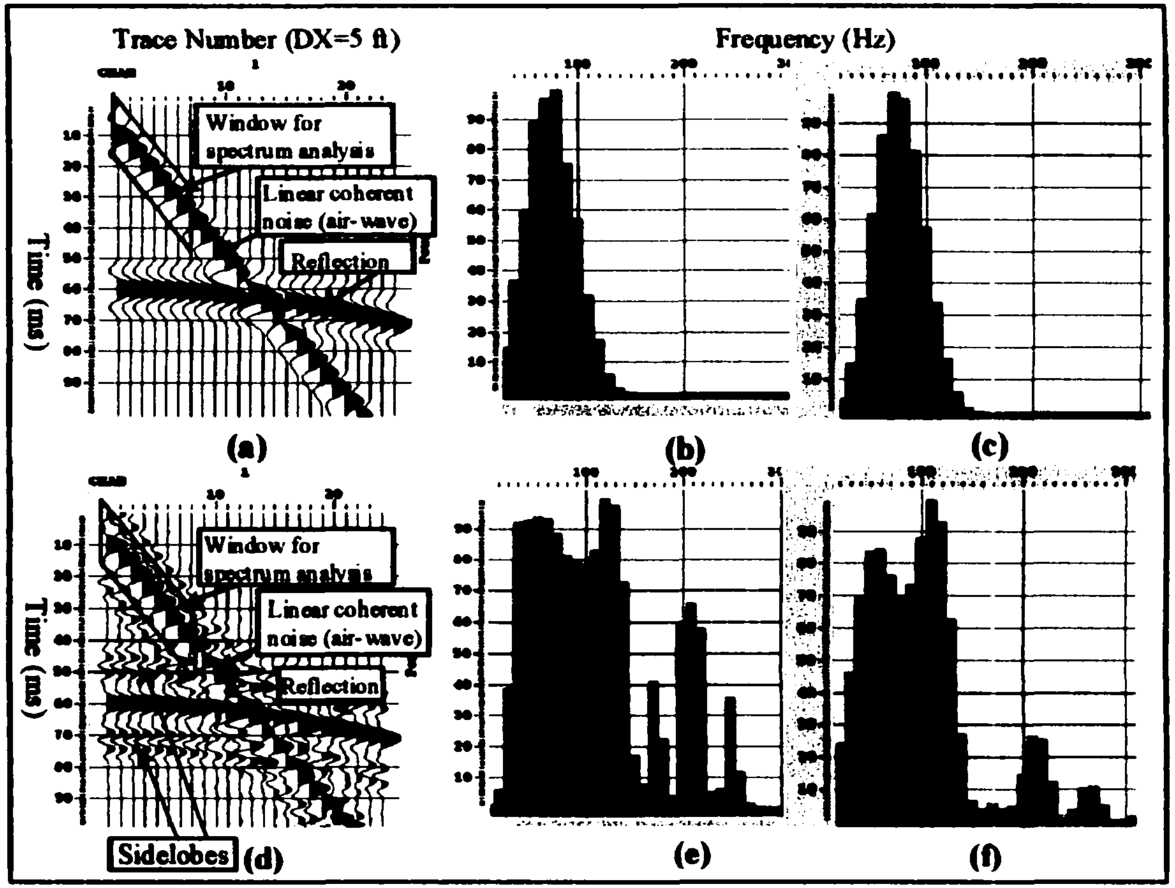

Figure 7 Continuous spectral balancing on synthetic shot gather to illustrate that signals and noise must have sufficient spectral differences. In the case of small differences, the continuous spectral balancing will fail to suppress the linear coherent noise, or even make it worse. (a) Synthetic shot gather consisted of a reflection event and a linear noise event, with the same zero phase wavelet; (b) Average spectrum of the entire shot gather (a); (c) Average spectrum of the data inside the window in (a); (d) Shot gather after applying continuous spectral balancing to (a). The sidelobes of the wavelets are much bigger, showing that the continuous has failed to suppress the linear coherent noise and that undesirable sidelobes (ringing) have resulted. (e) Average spectrum of the entire spectral balanced shot gather (d); (f) Average spectrum of the data inside the window in (d).

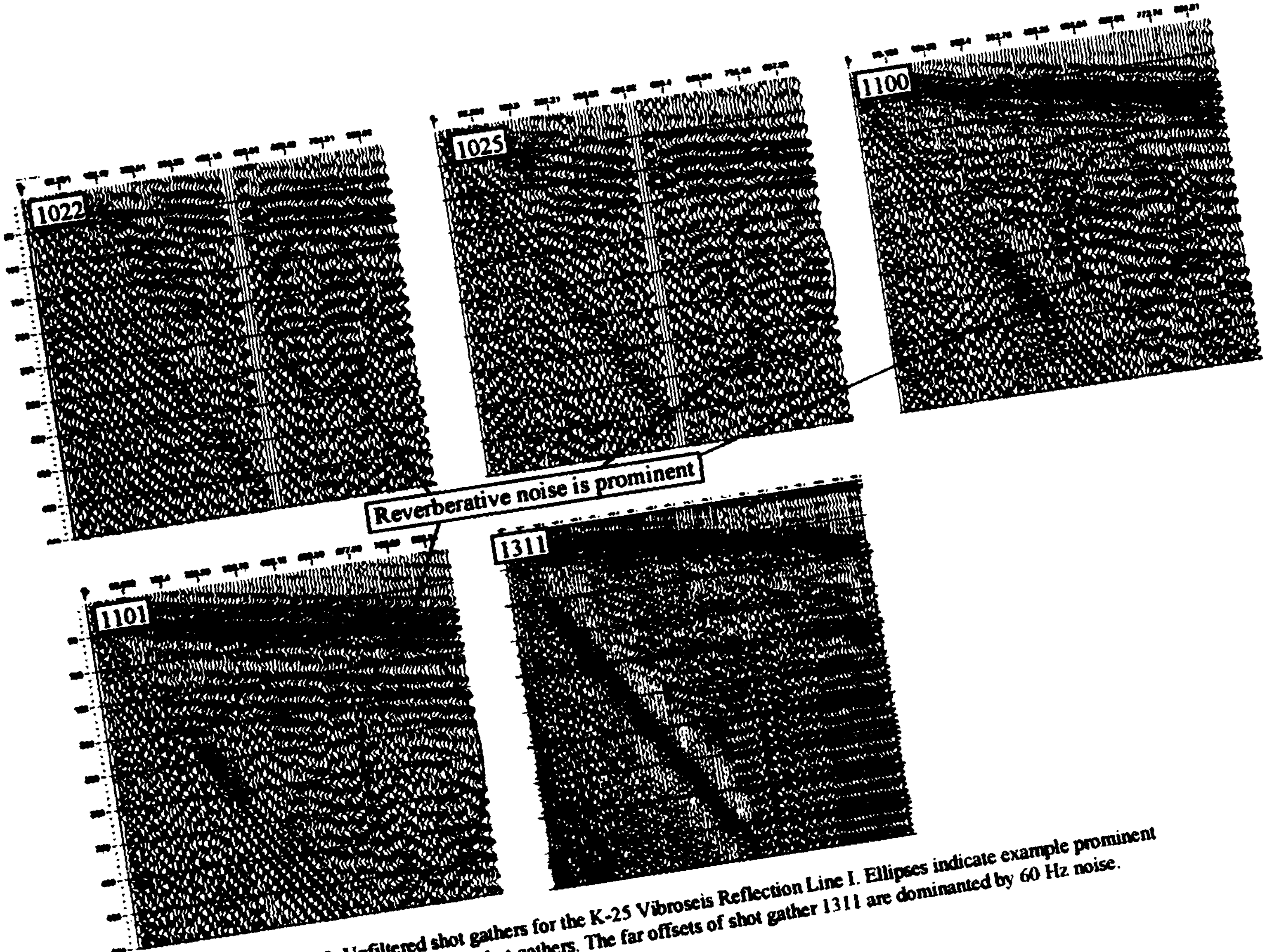

Figure 8 Unfiltered shot gathers for the K-25 Vibroseis Reflection Line I. Ellipses indicate example prominent reverberative noise in the shot gathers. The far offsets of shot gather 1311 are dominanted by 60 Hz noise.

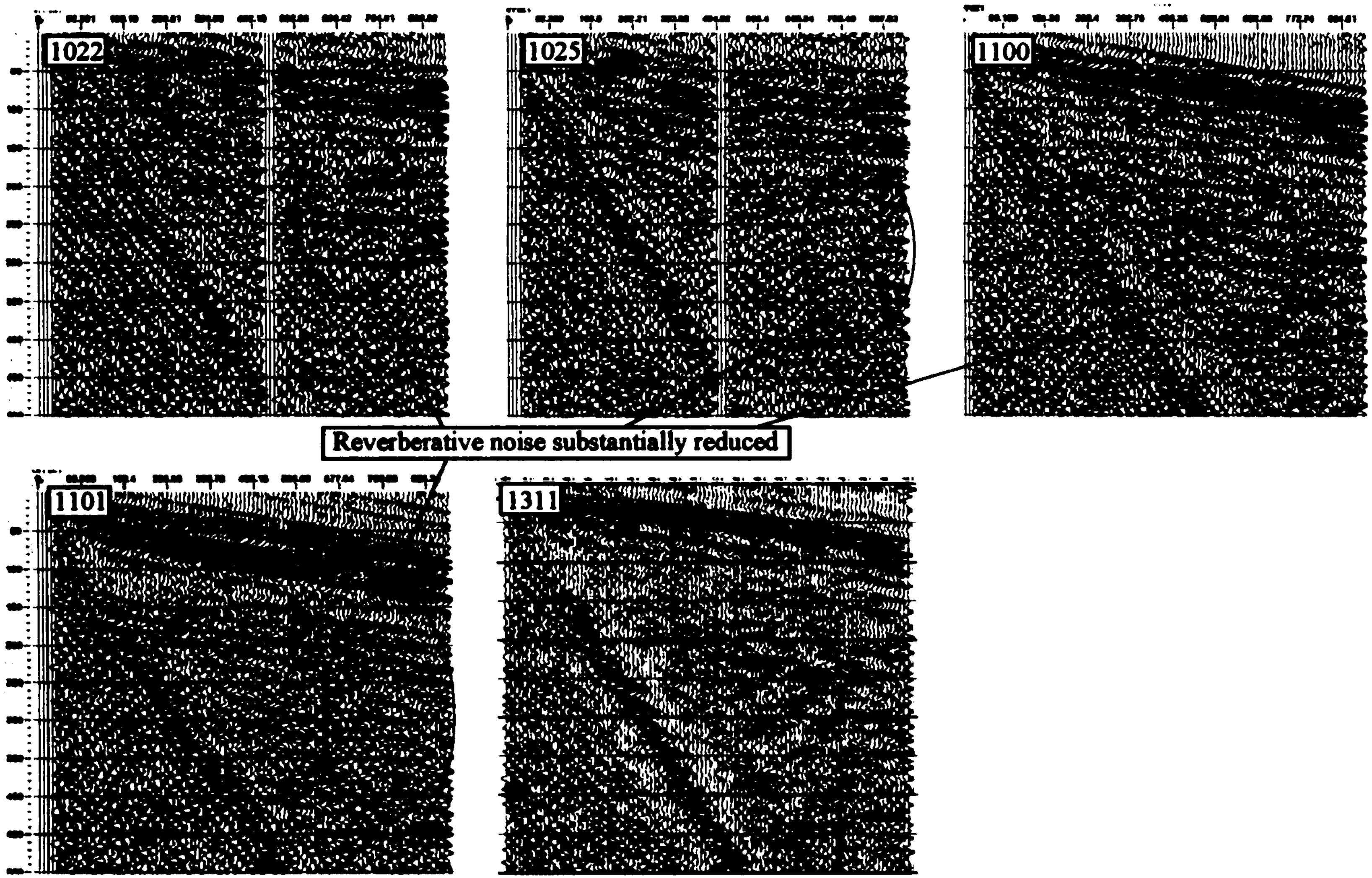

Figure 9 Continuous spectral balancing of shot gathers for the K-25 Vibroseis Reflection Line I. Ellipses show that prominent reverberative noise in the shot gathers corresponding to Figure 8 has been greatly reduced. The 60 Hz noise dominating the far offsets of shot gather 1311 of Figure 8 has been removed.

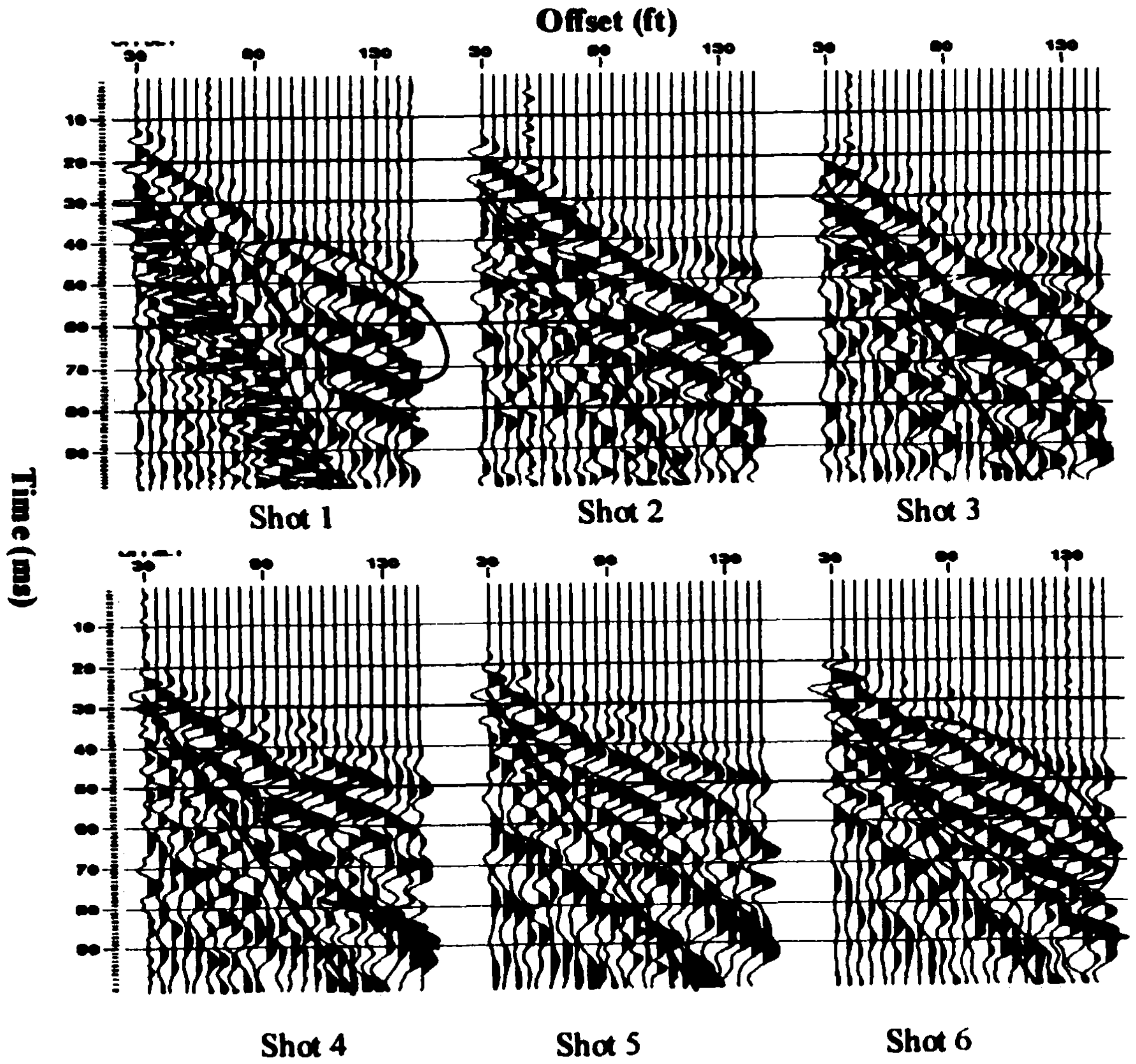

Figure 10 Unfiltered shot gathers for the Gypsy CMP Reflection Line 2628. The possible reflections are marked with red lines. Air-wave is marked with blue lines. Ground-roll is marked with green lines.

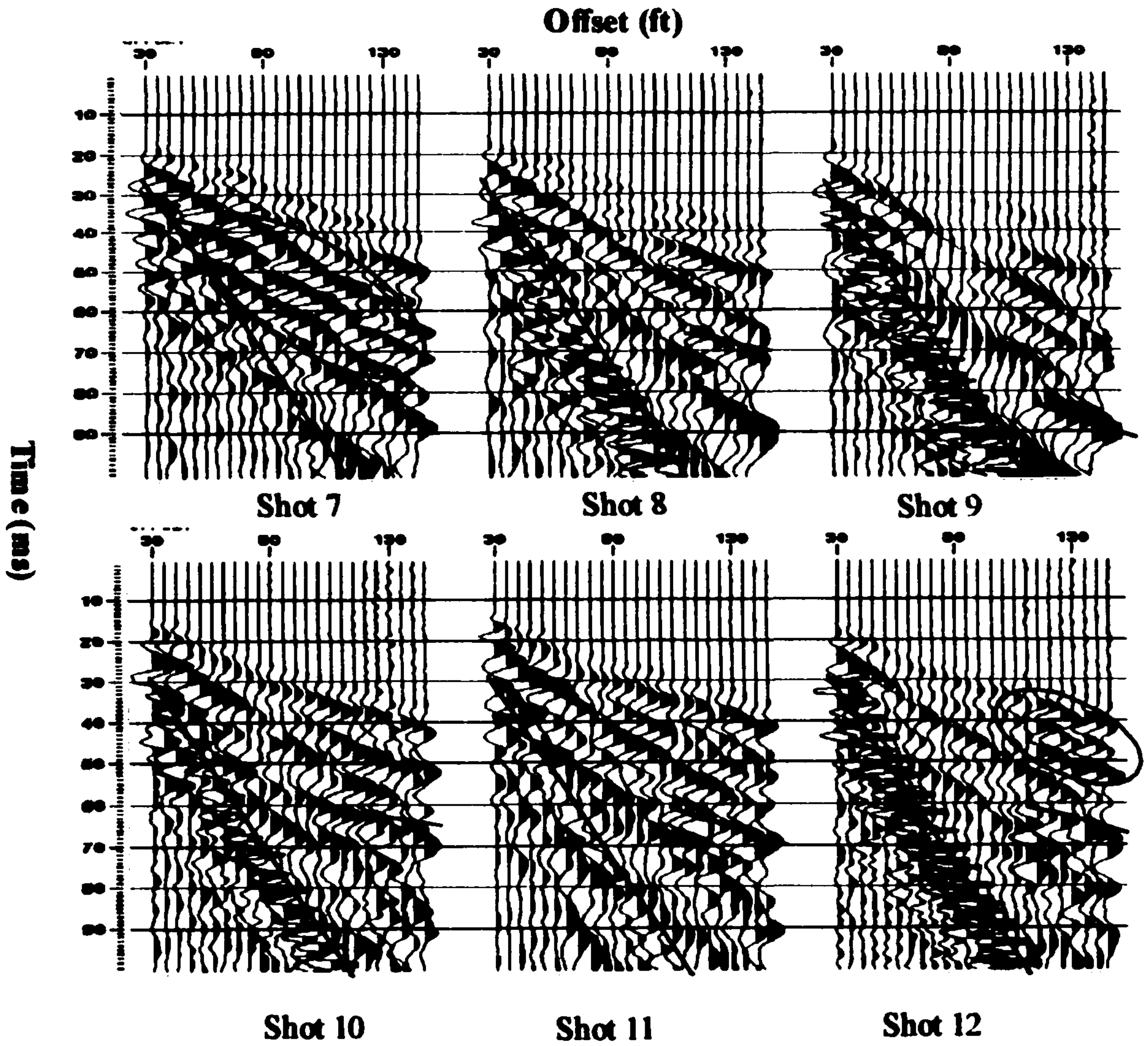

Figure 10 (continued) Unfiltered shot gathers for the Gypsy CMP Reflection Line 2628.

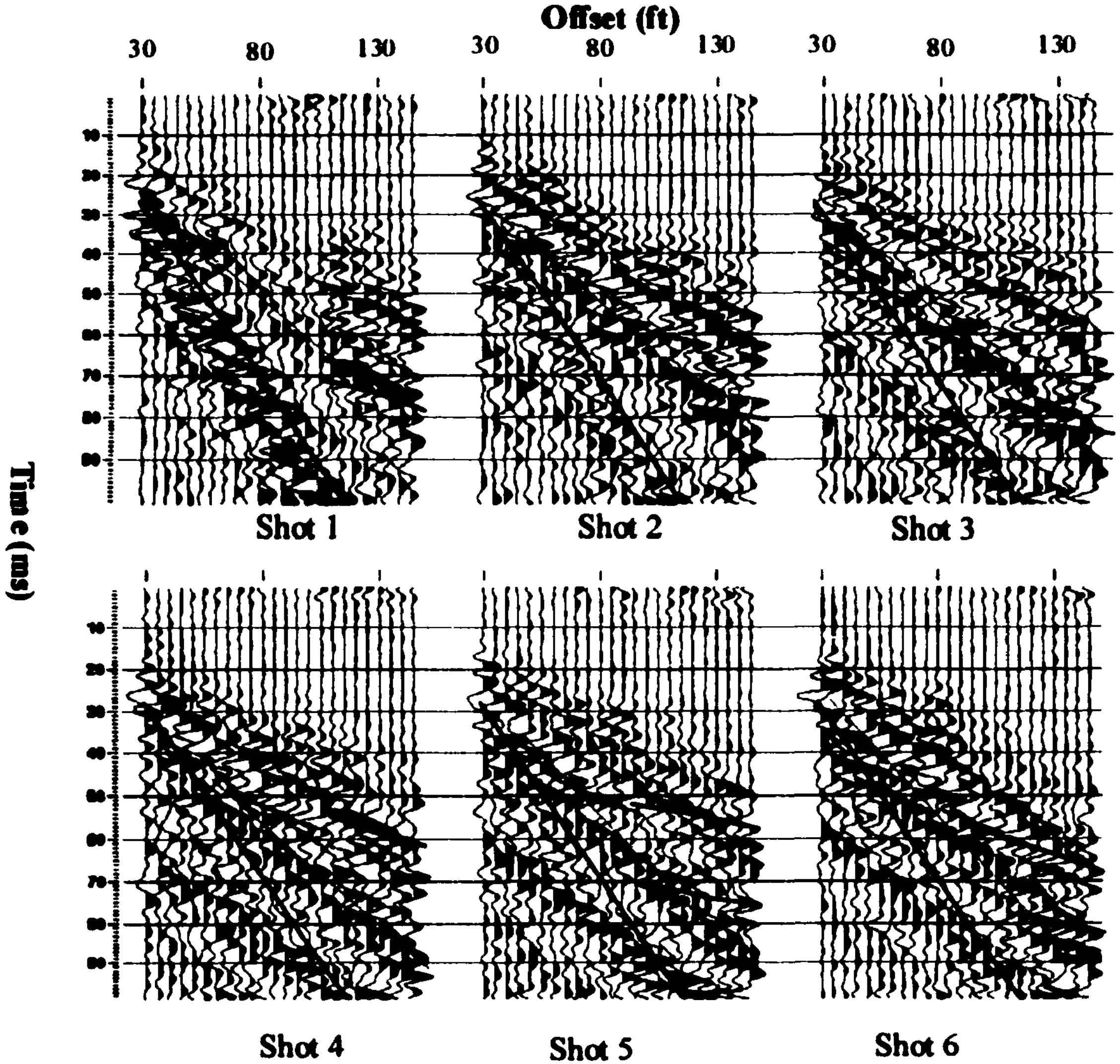

Figure 11 Continuous spectral balancing of shot gathers 1-12 of Gypsy CMP Reflection Line 2628. The possible reflections are marked with red lines. Air-wave is marked with blue lines. Ground-roll is marked with green lines.

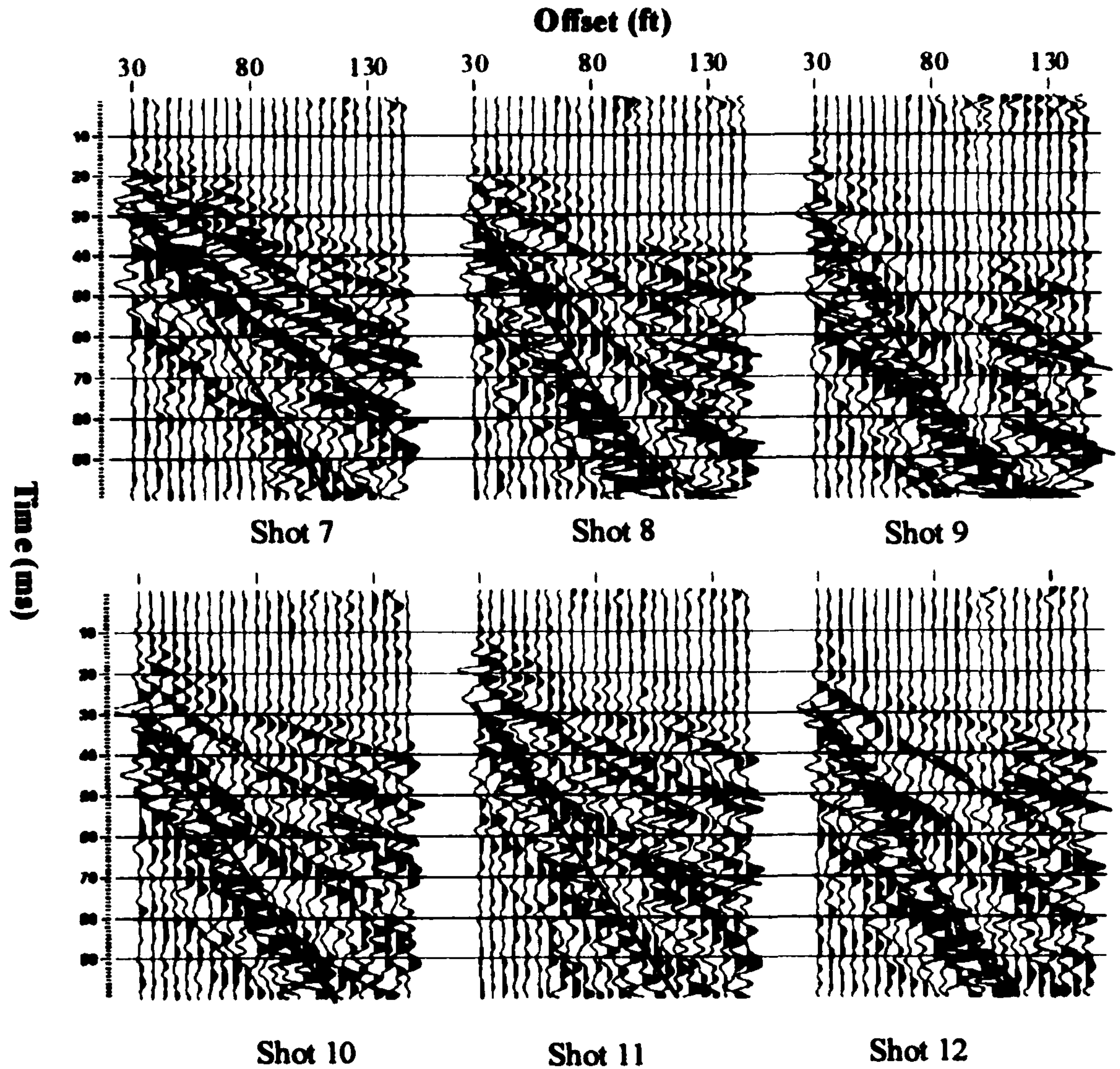

Figure 11 (continued) Continuous spectral balancing of shot gathers 1-12 of Gypsy CMP Reflection Line 2628.

APPENDIX B LOCAL SLANT-SUM ADAPTIVE NOISE REMOVAL

INTRODUCTION

"Local Slant-Sum Adaptive Noise Filtering" (LSSANR) is the name I give to the algorithm I designed and implemented to filter linear coherent noise. This algorithm is written in Visual Basic, with a graphical user interface to enable interactive filtering and graphical display of results. The LSSANR filters noise from signal in the time–space domain, based on the slope differences between noise and signal. Different from frequency filtering, the LSSANR does not require spectral difference between noise and signal. Similar to F-K and τ-p filtering, the LSSANR requires slope and/or apparent velocity differences between noise and signal. Different from F-K and τ-p filtering, the LSSANR does not perform any transformation and it is very localized within time–space windows, hence the LSSANR does not have, or at least has less severe, smearing problems inherent in the F-K and τ-p methods.

EXAMPLES WITH SYNTHETIC SHOT GATHERS

Figure 1 is an example to show the basic concepts of the LSSANR. Figure 1A is a synthetic shot gather consisting of a reflection event (from a dipping layer) and a linear coherent noise event (ground-roll). The term, "Local Slant-Sum" is given as a first qualifier to the algorithm to refer to adding up the seismic traces within local, slant, sliding noise evaluating time windows (e.g., blue box in Figure 1A), so as to evaluate and thereby to remove the noise wavelets from the seismic traces. Figure 1B shows the

LSSANR filtering result with the fixed noise evaluating time window (blue box in Figure 1A). This gives a perfect recovery of the reflection event. However, this requires the assumption of static, unchanging noise wavelet and may not work for field seismic data. Figure 1C shows the LSSANR filtering result with sliding noise evaluating time windows along the traveltimes of the linear coherent noise (red ticks in Figure 1A). This is more practical in case of slowly changing amplitude and phase of the noise wavelets in time and space, even though residual noise exists due to interference within noise wavelet evaluation window. This example shows that the LSSANR has the ability to filter out multiple linear-coherent noise modes.

Figure 2 is an example of the LSSANR with several linear coherent noise modes. In Figure 2A, there is one reflection event from a dipping layer boundary and there are several linear coherent noise modes, some of which even have time gaps (breaks). In such cases, the F-K and τ-P methods (even the local τ-P methods) will have problems at the time gaps. Figure 2B is the LSSANR filtering result of (A) with noise wavelet evaluated from the fixed time window (Blue box in Figure 2A). Perfect recovery of the reflection event is obtained. However, this may be impractical in case of slowly changing amplitude and phase of the noise wavelets. Figure 2C is the filtering result of (A) with noise wavelet evaluated from sliding time windows along each individual linear coherent noise's traveltimes (tick marks in Figure 2A). This is more practical in case of slowly changing amplitude and phase of the noise wavelets in time and space, even though residual noise exists due to interference within the noise wavelet evaluation window.

For fast-changing amplitudes and phases of linear coherent noise modes, such as dispersive ground-roll, it is necessary to make the algorithm adaptive to make amplitude and phase adjustments. Amplitude adaptation of the LSSANR is achieved by obtaining a scale factor, with the sum of the absolute values of the trace within the time window to be filtered as the numerator, and the sum of the absolute values of the noise wavelet as the denominator. This scale factor is used to multiply the noise wavelet to produce the wavelet to be subtracted from the trace.

Phase adaptation requires more explanation. Figure 3 shows synthetic traces with dispersive wavelets, which become longer and lower frequency with the increase in time and offset. In noise estimation time windows, the data traces are linearly interpolated by matching the phases (peaks, troughs, zero-crossings, etc.) to produce a data value for the noise wavelet. The algorithm is programmed to automatically match the phases in the noise estimation time windows and in the subtraction of the noise wavelet from the seismic traces.

Figure 4 is an example with dispersive coherent noise. Figure 4A is the synthetic shot gathers consisted of a reflection event (from a dipping layer boundary) and a dispersive linear coherent noise event. Figure 4B shows the LSSANR filtering result with the fixed time window (blue box in Figure 4A). Because the linear coherent noise in this example is highly dispersive, the fixed time window approach has failed to remove the linear coherent noise at all. By using sliding time windows and phase-matching during noise wavelet evaluation and subtracting, however, the reflection event has been recovered fairly well. Residual noise exists due to the interference from the reflection event during the noise wavelet estimation.

EXAMPLES WITH FIELD SHOT GATHERS

The field shot gather examples use the shot gathers of the Oak Ridge K-25 Line I (Chapter 1) as input. The input shot gathers have been processed using Vibroseis whitening, refraction statics, band-pass filtering and continuous spectral balancing. These are the best processing steps as discussed in Chapter 1. In some of the shot gathers of Line I, there exist a strong linear coherent noise (ground-roll), extending from near offset and small time toward far offset and large time. The linear coherent noise quickly weakens after approximately 100 ms. The LSSANR will be used to remove this particular noise, thereby providing the potential of improving the seismic imaging of the shallow parts of the stacked sections and even the prestack depth migrations.

In the following field data examples, sliding windows, automatic amplitude adaptation, and phase adaptation are included in the noise wavelet evaluation and noise removal process.

Figure 5 is the first example of the LSSANR for field data from Oak Ridge K-25 (Chapter 1). Figure 5A is the input shot gather. Figure 5B is the LSSANR filtering result, showing that the LSSANR filtering has made the possible reflection events (red dots) standout and the strong linear coherent noise is substantially removed.

Figure 6 is yet another example for the field data from the Oak Ridge K-25. In addition to confirming Figure 5 in removing the linear coherent noise (ground-roll), this figure illustrates that the LSSANR can also be used to remove refraction events. Additional LSSANR filtering with shot gathers are shown in Figures 7, 8 and 9. They serve as additional proof that the LSSANR filtering is effective on real data shot gathers.

CONCLUSIONS

Synthetic and field data examples show that the LSSANR is an effective algorithm to remove linear coherent noise. This is a multi-channel, highly interactive and adaptive noise filtering algorithm, making it possible to leave certain parts (such as those with reflections but without noise interference) of the shot gathers untouched. LSSANR can be used to remove any kind of linear coherent noise, provided the time window has been picked by the data processor. Alternatively, LSSANR can be used to remove any part and type of the coherent events, which are considered to be non-reflection events. Improvements of the LSSANR can be made using even more adaptive evaluation of the noise wavelets. These include evaluating of noise wavelets away from the vicinity of the reflection events and using weighting factors.

As a direction for future work, the coding of the LSSANR needs to be improved to be more automatic, less time-picking intensive, and less user-interaction intensive, and thereby be of practical usefulness for filtering large amount of data.

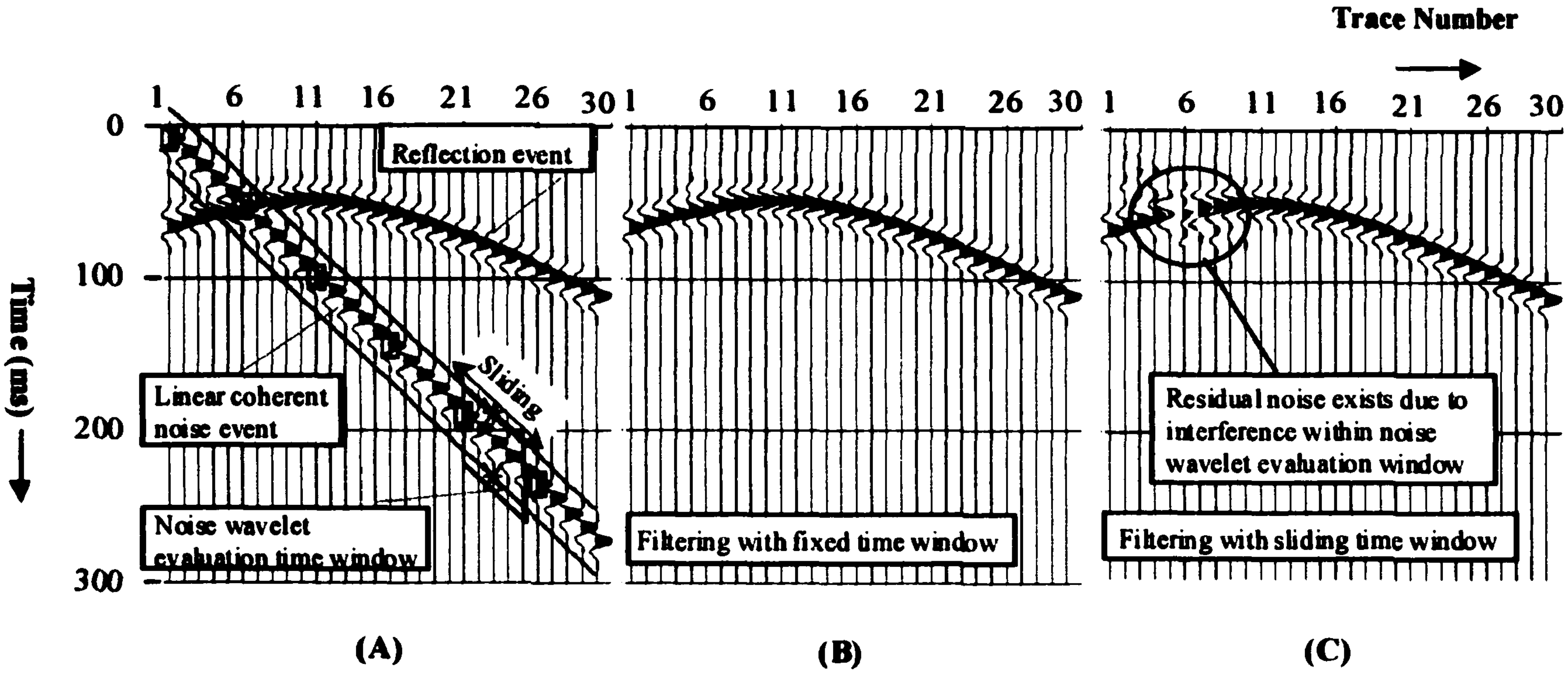

Figure 1 LSSANR filtering of a synthetic shot gather consisted of a reflection event (from a dipping layer) and a linear coherent noise event. (A) Synthetic shot gather. (B) Filtering result of (A) with noise wavelet evaluated from fixed time window (Blue box in (A)). (C) Filtering result of (A) with noise wavelet evaluated from sliding time windows. This is more practical in case of slowly changing amplitude and phase of noise wavelets in time and space, even though residual noise exists due to interference within noise wavelet evaluation window.

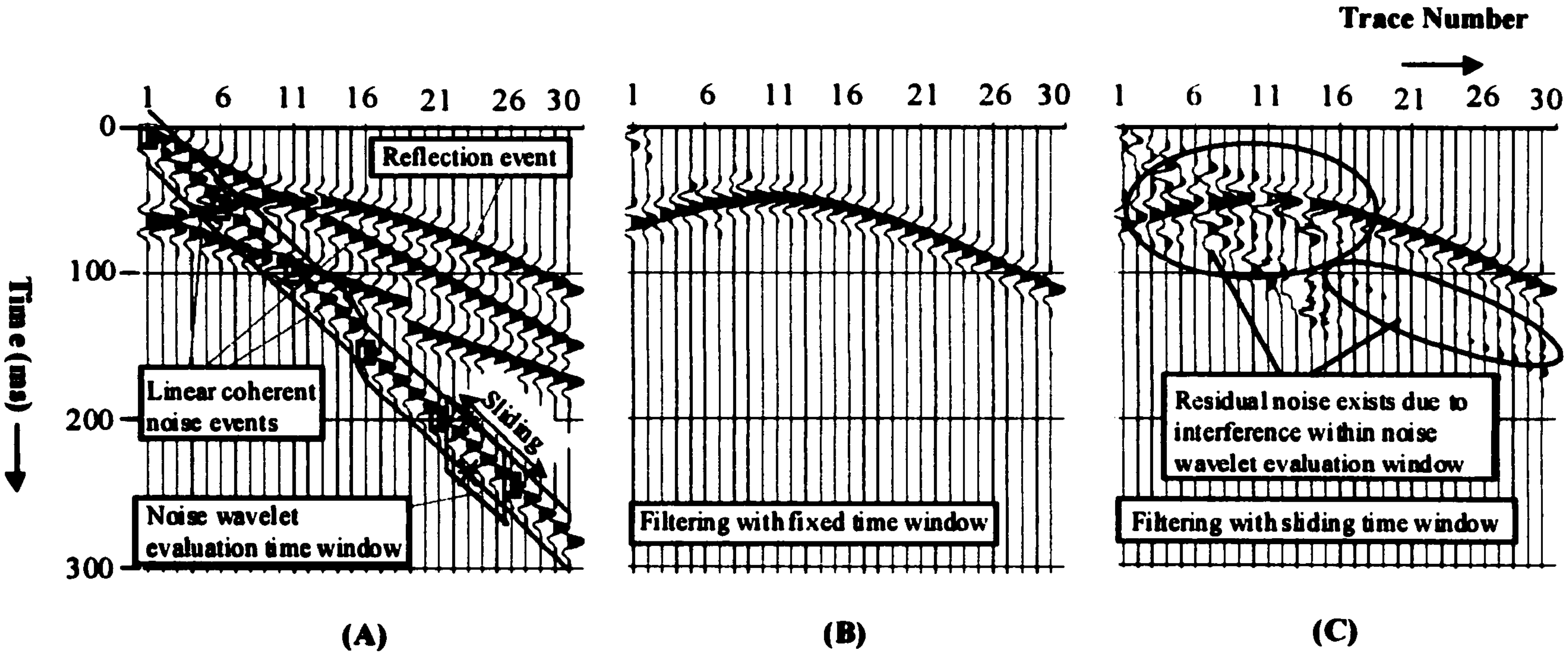

Figure 2 LSSANR filtering of a synthetic shot gather consisted of a reflection event (from a dipping layer) and three linear coherent noise events. (A) Synthetic shot gather. (B) Filtering result of (A) with noise wavelet evaluated from the fixed time window (Blue box in (A)). (C) Filtering result of (A) with noise wavelet evaluated from sliding time windows. This is more practical in case of amplitude and phase changes of wavelet in time and space, even though residual noise exists due to interference within noise wavelet evaluation window.

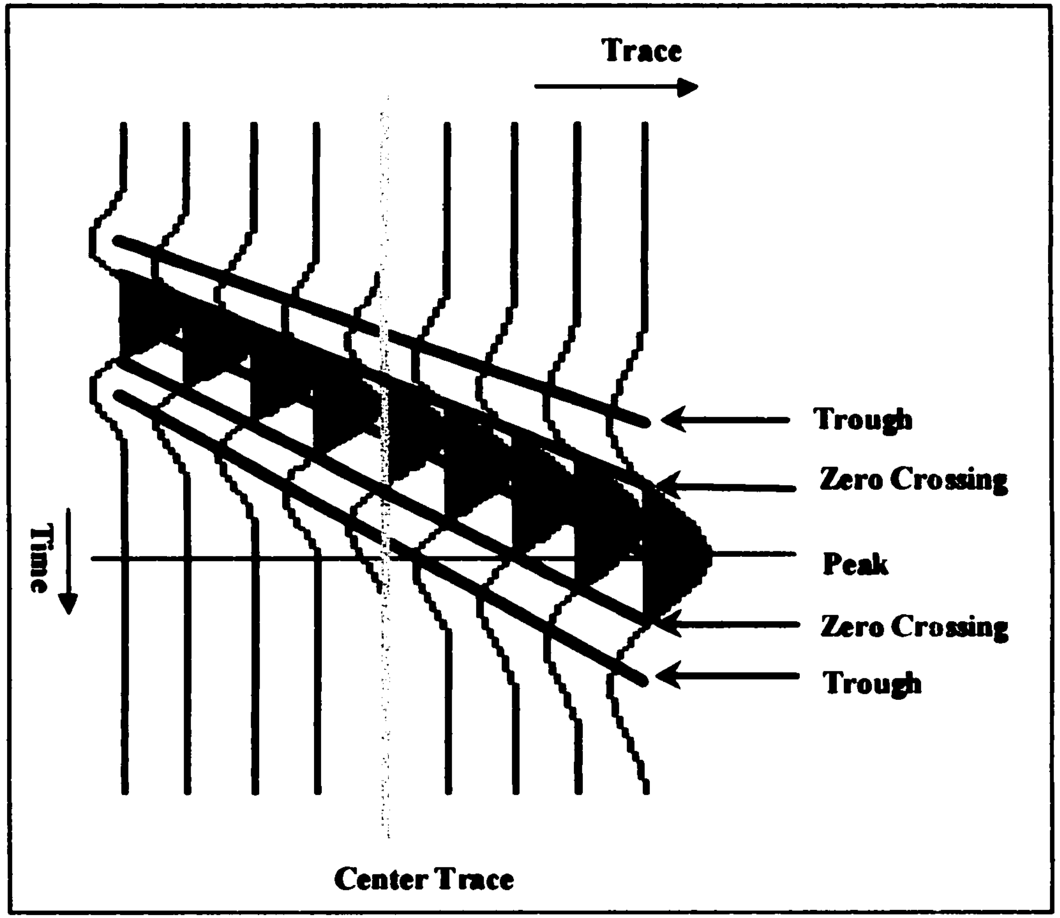

Figure 3 Noise wavelet evaluation by phase matching to account for dispersive ground-roll: Data points with the same phase (such as peaks, troughs, zero crossings, shown with colored lines) are interpolated and averaged to produce a data value of the noise wavelet evaluated for the center trace.

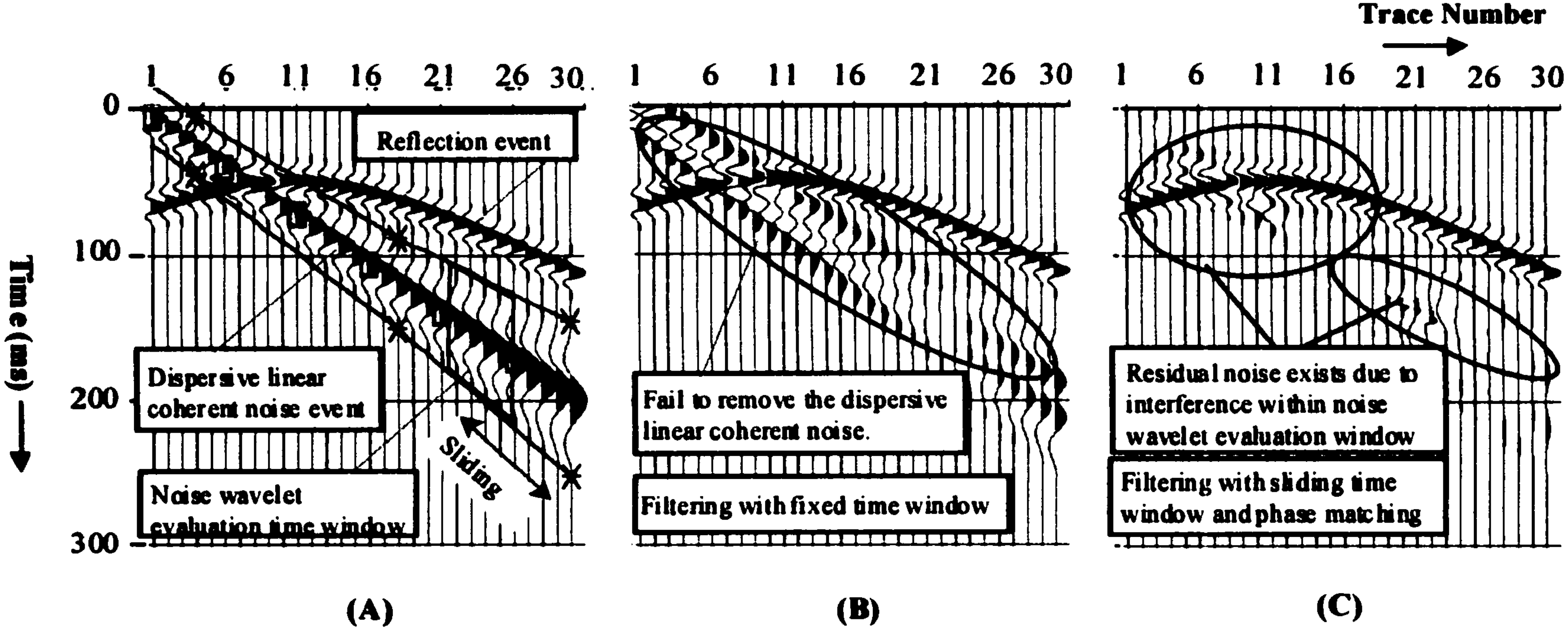

Figure 4 LSSANR filtering of a synthetic shot gather consisted of a reflection event (from a dipping layer) and a dispersive noise event (ground-roll). (A) Synthetic shot gather. (B) Filtering result of (A) with noise wavelet evaluated from the fixed time window (Blue box in (A)). (C) Filtering result of (A) with noise wavelet evaluated from sliding time windows, and phase matching to account for dispersive noise event. This is more practical and necessary in case of dispersive linear coherent noise,even though residual noise exists due to interference within noise wavelet evaluation window.

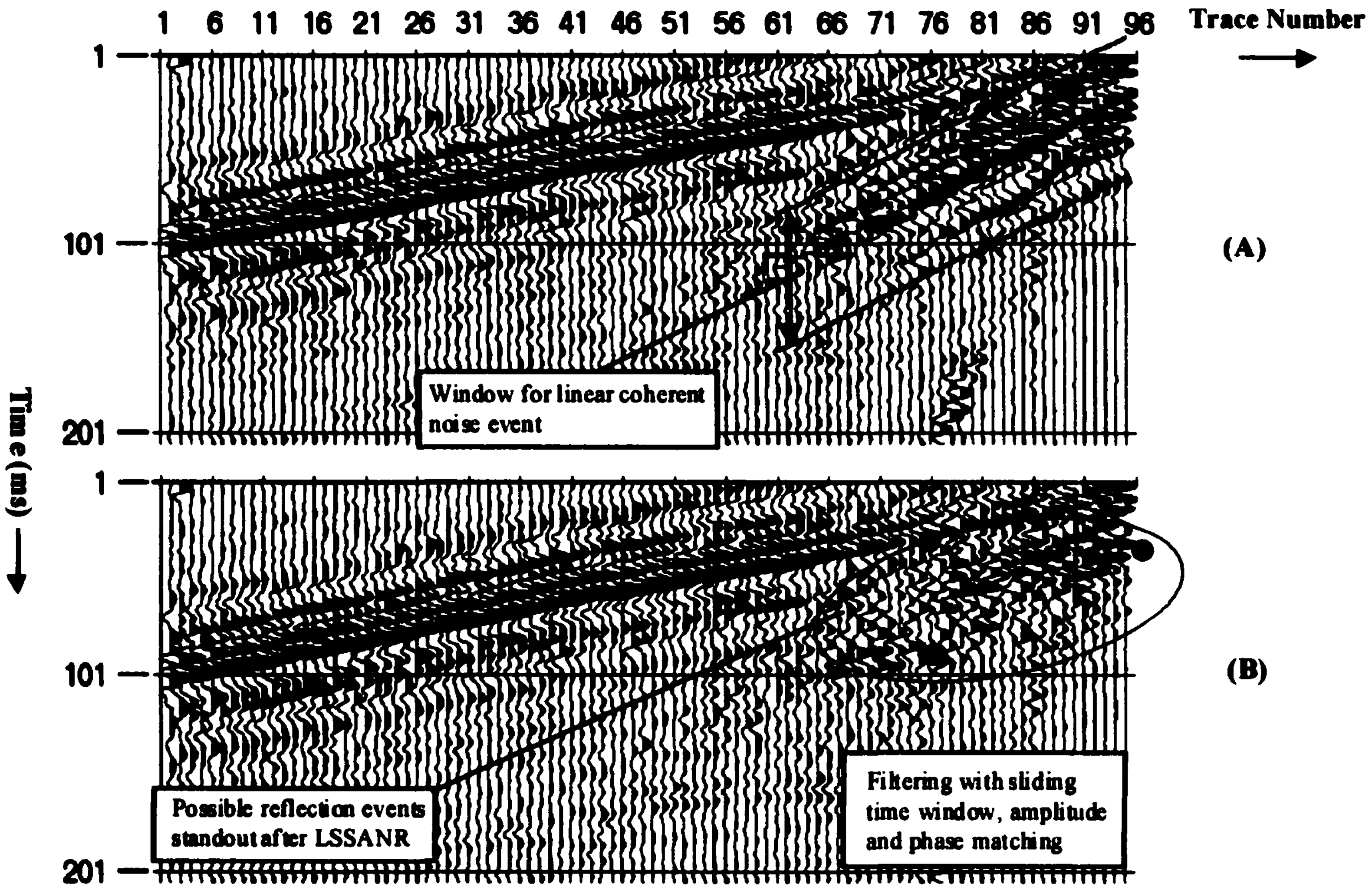

Figure 5 LSSANR filtering of a shot gather from Oak Ridge K-25 Site. (A) Shot gather with Vibroseis hitening, refraction statics, and continuous spectral balancing included. (B) Filtering result of (A) using sliding time windows, phase matching and amplitude matching. Reflection events standout after LSSANR (at red dots).

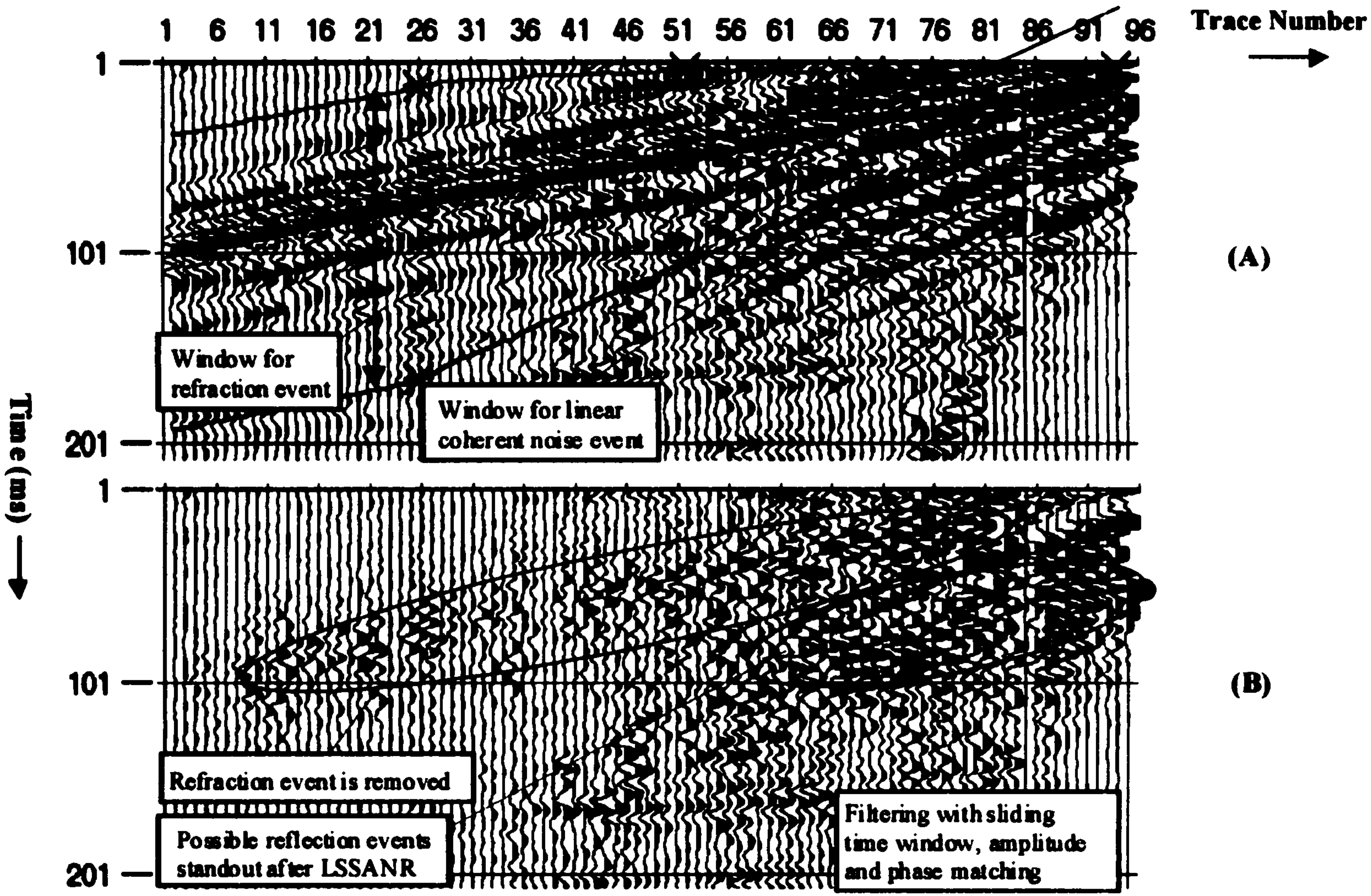

Figure 6 LSSANR filtering of another shot gather from Oak Ridge K-25 Site. (A) Shot gather with Vibroseis whitening, refraction statics, and continuous spectral balancing included. (B) Filtering result of (A) using sliding time windows, phase matching and amplitude matching. Reflection events standout after LSSANR (at red dots). In addition to removing the linear coherent noise (ground-roll), the refraction event is also removed.

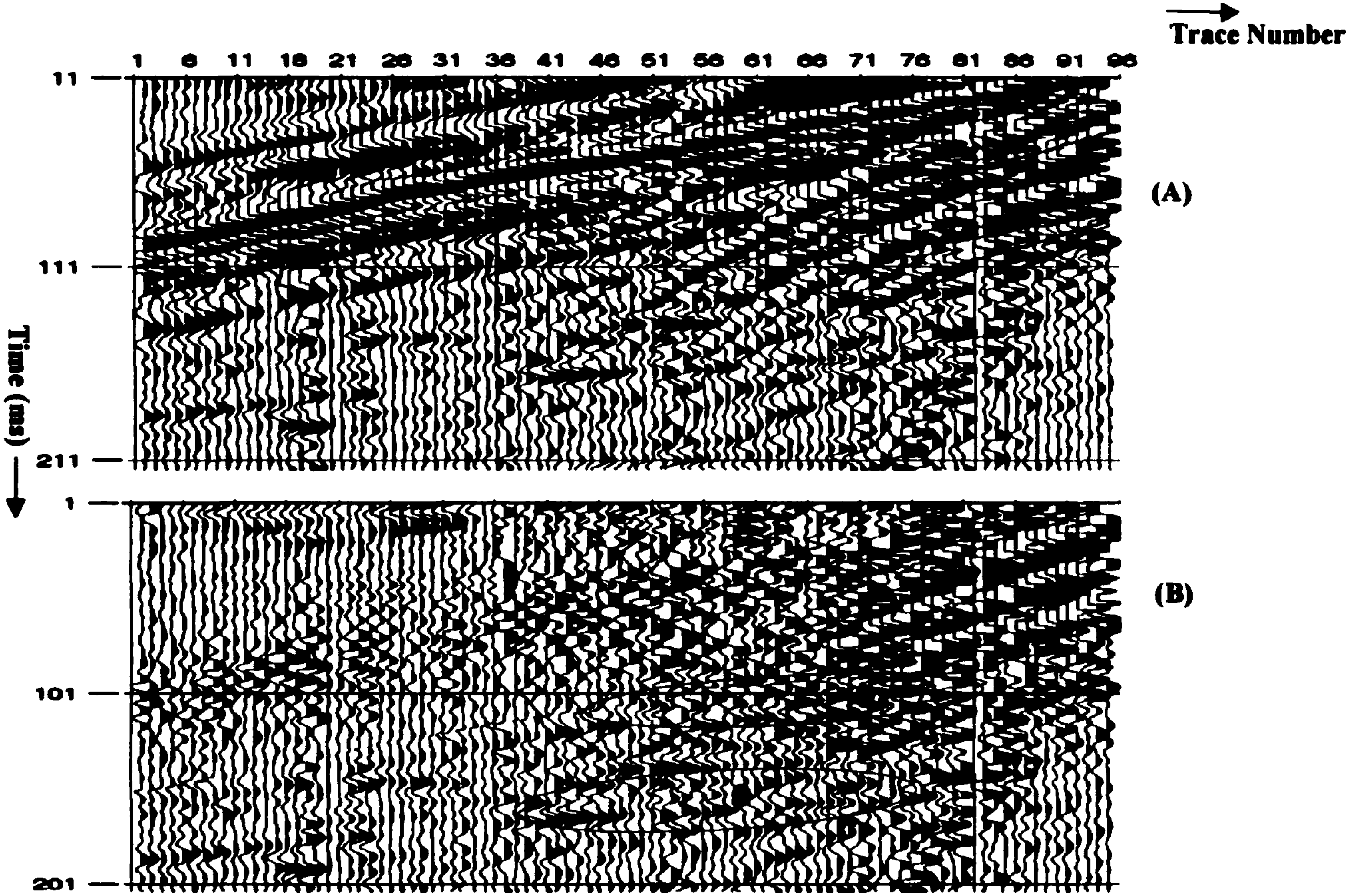

Figure 7 LSSANR filtering of additional shot gather from Oak Ridge K-25 Site. (A) Shot gather with Vibroseis whitening, refraction statics, and continuous spectral balancing included. (B) LSSANR filtering result of (A) using sliding time windows, phase matching and amplitude matching. Reflection events standout after LSSANR (events with gentle slopes at red dots inside the circles).

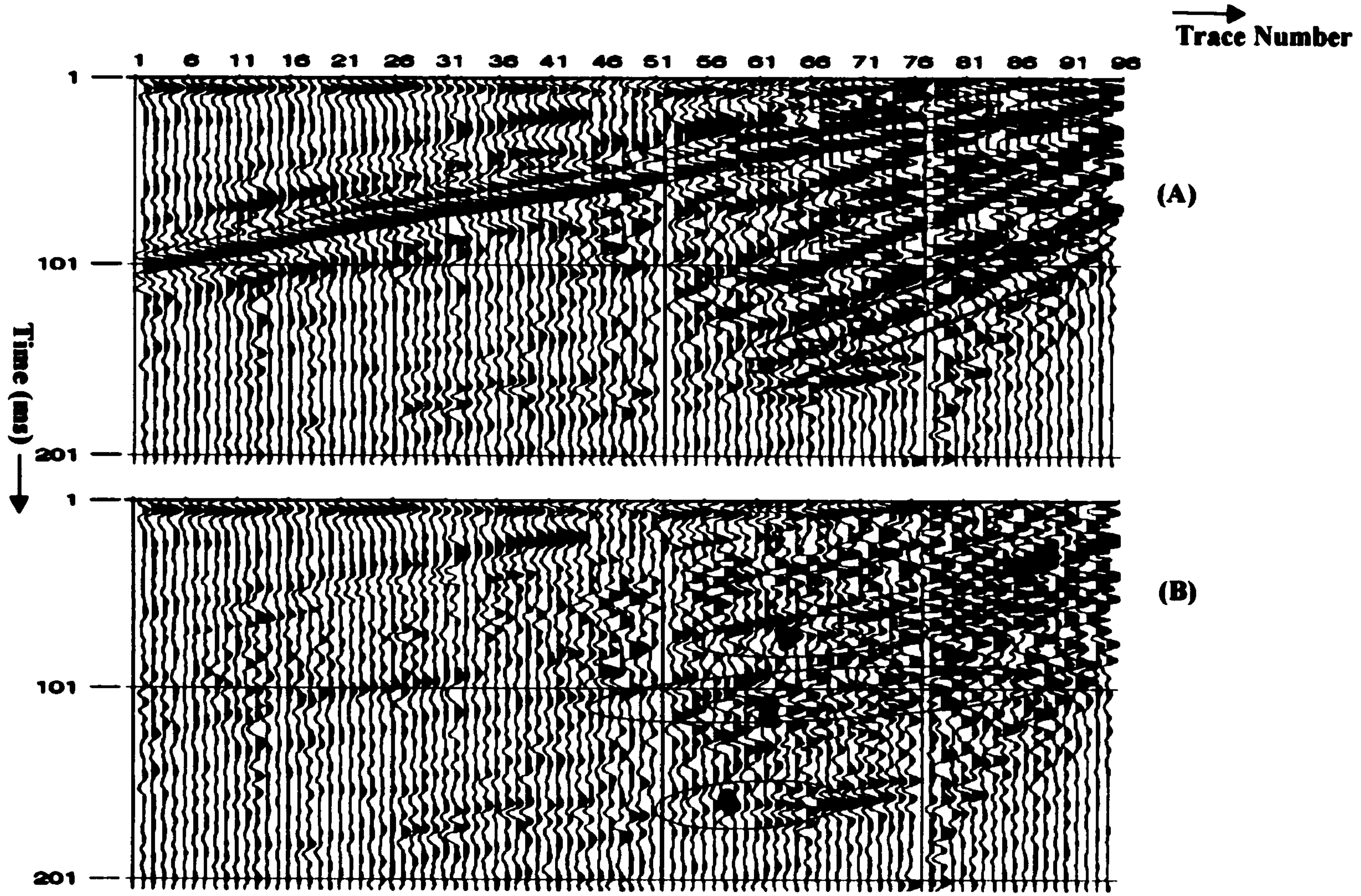

Figure 8 LSSANR filtering of additional shot gather from Oak Ridge K-25 Site. (A) Shot gather with Vibroseis whitening, refraction statics, and continuous spectral balancing included. (B) LSSANR filtering result of (A) using sliding time windows, phase matching and amplitude matching. Reflection events standout after LSSANR (events with gentle slopes at red dots inside the circles).

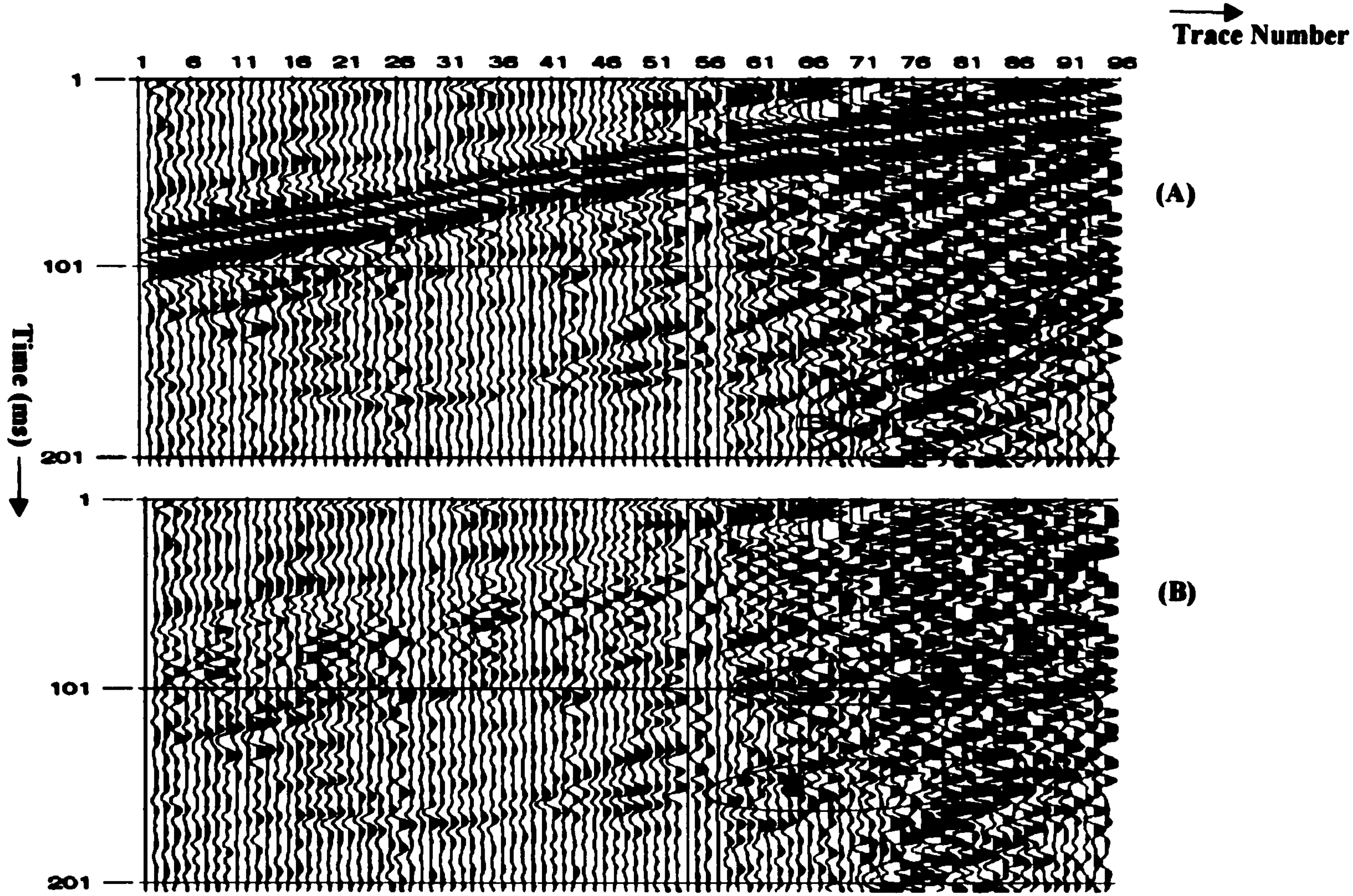

Figure 9 LSSANR filtering of additional shot gather from Oak Ridge K-25 Site. (A) Shot gather with Vibroseis whitening, refraction statics, and continuous spectral balancing included. (B) LSSANR filtering result of (A) using sliding time windows, phase matching and amplitude matching. Reflection events standout after LSSANR (events with gentle slopes at red dots inside the circles).